UNIVERSIDAD COMPLUTENSE DE MADRID
FACULTAD DE CIENCIAS FÍSICAS

TESIS DOCTORAL

The Search for water ice on Comets and Asteroids

La búsqueda de hielo de agua en Cometas y Asteroides

MEMORIA PARA OPTAR AL GRADO DE DOCTOR

PRESENTADA POR

Laurence O'Rourke

DIRECTOR

Michael Küppers

Madrid

UNIVERSIDAD COMPLUTENSE DE MADRID
FACULTAD DE CIENCIAS FÍSICAS

TESIS DOCTORAL

La búsqueda de hielo de agua en Cometas y Asteroides

MEMORIA PARA OPTAR AL GRADO DE DOCTOR

PRESENTADA POR

Laurence O'Rourke

DIRECTOR

Dr. Michael Küppers

The Search for water ice on Comets and Asteroids

La búsqueda de hielo de agua en Cometas y Asteroides

TESIS DOCTORAL

LAURENCE O'ROURKE

Departamento de Física de la Tierra y Astrofísica

Facultad de Ciencias Físicas

Universidad Complutense de Madrid

A thesis submitted for the degree of

Doctor en Astrofisica

September 2020

Director: Dr. Michael Küppers Tutor: Prof. David Montes Gutiérrez

Dedication

I would like to dedicate this thesis to my wife Cristina & our children David and Paulina, and to my parents, Laurence and Rita (neé Curley) O'Rourke, who have both passed away but who would no doubt have been very proud of me for this achievement.

Acknowledgements

This work has been possible thanks to the great support and help provided by my PhD director Michael Küppers and by my UCM tutor, David Montes Gutiérrez.

The published papers presented, provide an excellent overview of the significant collaborations I have had across the planetary science community with nearly 50 different co-authors represented in the papers. Their professionalism, expertise and friendship were vital to ensure that the papers I wrote were at the highest level. I would like to make a special mention for those who I have worked with most closely namely Michael, Dominique, Nicolas, Thomas, Sonia and David.

A work like this, done in parallel to my job at ESA, is only feasible through countless hours (days & nights, weekends and holidays) spent away from the family. To my amazingly patient and lovely wife Cristina, my son David and my daughter Paulina, my thanks and love. They have kept my feet on the ground while my mind was in space.

My sisters (Ita and Anne), brothers (John, Hughie, James, Tony and Tom), and in-laws (Martin, Declan, Assumpta, Loretta, Elaine, Celine and Teresa) in Ireland and the U.S. have been very supportive of me and have provided good advice throughout all my years working and studying and my thanks go to them also.

Abstract

The presence of water is considered one of the key ingredients for the formation of life on Earth. Indeed, current theories as to the origin of the Earth's oceans suggest that the water located there originated from both comets and asteroids, with the exact fractional contribution still under discussion. However, water is not unique to the Earth; it has been found hidden deep inside polar craters on the moon, as well as in its fragment OH form contained in moon regolith. It is believed to make up over two thirds of the mass of the giant icy planets Uranus and Neptune. It is prevalent in the form of ice throughout the outer solar system on the moons of planets, on Kuiper Belt Objects, and on comets. In the case of asteroids, although few detections of surface ice have been made, evidence of hydrated minerals (any mineral containing H_2O or OH) abound.

A search for water ice on the surface and subsurface of comets and asteroids provides not only key information as to its presence and distribution on these primitive bodies, it also contributes to giving a deeper understanding on how the solar system formed, how water was delivered to the Earth by these bodies, and indeed how life emerged as a result.

This thesis has as its main goal to search for the presence of water ice on and just below the surfaces of comets and asteroids, estimating its coverage and where feasible characterising its properties. This goal is broken down into two objectives, whereby we search for and characterise ice found on cometary (1st objective) and asteroid (2nd objective) surfaces and subsurfaces. In this thesis, we present a number of publications aiming to address these objectives.

To address the first objective, we present two papers; one main paper (Nature 2020) and a supporting paper (Astrophysical Journal Letters 2013). In our main paper, we search for water ice inside 2 cometary boulders lying on the surface of comet 67P/Churyumov-Gerasimenko. We apply multiple data analysis techniques to process multi-wavelength observations produced by the Rosetta orbiter merged with in-situ measurements from the Philae lander. The aim is to identify the ice and to characterise its physical properties, in particular its compressive strength and its porosity. In the case of the supporting paper, we searched for cometary activity around a Main-Belt Comet (an asteroid displaying cometary behaviour e.g. coma, tail), estimated its size, and searched for a water exosphere.

To address the second objective, we present three papers; one main paper (Astrophysical Journal Letters 2020) and two supporting papers (Nature 2014 & Astrophysical Journal Letters 2013). These three papers focus on a search for water ice present on the surface/subsurface of asteroids, linked to their relative size. While the main paper studies the case for two of the larger asteroids in the main belt, namely (24) Themis and (65) Cybele, the two supporting papers cover both the largest asteroid – Dwarf planet (1) Ceres – and one of the smallest asteroids (Main-Belt Comet P/2012 T1) which was mentioned above as it supports

also the first objective. In all three papers, we searched for an exosphere of water vapour using the Heterodyne Instrument on the Herschel Space Observatory (HIFI). We support our HIFI results with data from other observatories/instruments (VLT/FORS2, Herschel/SPIRE, Subaru/COMICS), as well as apply different models to aid in the understanding of our results. In the case of both of these supporting papers, we also present in this thesis the scientific progress achieved since we published them.

The results obtained from the papers presented in this thesis are quite unique. The output from our first paper was that we could confirm the presence of primitive (the chemical state of cometary materials as they began to agglomerate/accrete into macroscopic bodies – see Annex F4) ice inside cometary boulders, lying just below their dusty surface. We determined the softness of this primitive ice as well as derived a porosity equivalent to that measured in the comet as a whole. While water ice is generally exposed on the comet through fractures breaking open the dust covered exterior leading to outbursts and jets, in our case the ice was confirmed to be exposed by movements of the Philae lander itself during its bounce across the surface. For our second paper, a non-detection of an exosphere around asteroids (24) Themis and (65) Cybele led to our calculation of highly sensitive upper limits for the water production rate. We estimated that water ice intimately mixed with the asteroids' dark surface material would cover <0.0017% (for Themis) and <0.0033% (for Cybele) of their surfaces, while an areal mixture with very clean ice would cover < 2.2%. Based on this low percentage of surface coverage, we disproved the results of a Nature paper (Campins et al. 2010) which proposed a link between 3.1 μm absorption feature and surface ice on asteroids.

With our first supporting paper, we were the first to confirm the presence of water ice in the asteroid belt when we discovered in 2013 that Dwarf planet (1) Ceres had an exosphere produced from the sublimation of water ice that covered < 10^{-7} of its total surface area. In our second supporting paper, we did not detect an exosphere even though the Main-Belt Comet had a coma at the time of the Herschel observation. Our non-detection allowed us to derive sensitive upper limits on the water production rate as well as estimate a water ice surface coverage of 0.2%.

We close out the thesis by presenting our conclusions and proposing future work in this area. The presence of water ice on comets and on the largest asteroid in the solar system has been confirmed from the studies performed in this thesis. The physical makeup and processes in play to expose this water ice have been discussed in detail. For asteroids of size <300km, the direct confirmation of surface & subsurface water ice remains elusive however. With the launch of JWST (James Webb Space Telescope) as well as the building of bigger and more sensitive Ground based observatories, new techniques are expected to come on line to push the limits in achieving such detections.

Resumen

La presencia de agua se considera uno de los ingredientes clave para la formación de vida en la Tierra. De hecho, las teorías actuales sobre el origen de los océanos de la Tierra sugieren que el agua que se encuentra allí se originó tanto en cometas como en asteroides, con la contribución fraccionaria exacta aún en discusión. Sin embargo, el agua no es exclusiva de la Tierra; se ha encontrado escondido en el interior de los cráteres polares de la luna, así como en su forma de fragmento OH contenido en su regolito. Se cree que constituye más de dos tercios de la masa de los planetas helados gigantes Urano y Neptuno. Prevalece en forma de hielo en todo el sistema solar exterior en las lunas de los planetas, en los objetos del cinturón de Kuiper y en los cometas. En el caso de los asteroides, aunque se han realizado pocas detecciones de hielo en la superficie, abunda la evidencia de minerales hidratados (cualquier mineral que contenga H2O u OH).

La búsqueda de hielo de agua en la superficie y el sub-superficie de cometas y asteroides proporciona no solo información clave sobre su presencia y distribución en estos cuerpos primitivos, sino que también contribuye a brindar una comprensión más profunda de cómo se formó el sistema solar, cómo se entregó el agua a la Tierra por estos cuerpos y, de hecho, cómo surgió la vida como resultado.

Esta tesis tiene como objetivo principal buscar la presencia de hielo de agua sobre y justo debajo de las superficies de cometas y asteroides, estimando su cobertura y, cuando sea posible, caracterizando sus propiedades. Este objetivo principal se divide en dos objetivos específicos, mediante los cuales buscamos y caracterizamos el hielo que se encuentra en los superficies y sub-superficies de cometas (primer objetivo) y asteroides (segundo objetivo). En esta tesis presentamos una serie de publicaciones destinadas a abordar estos objetivos.

Para abordar el primer objetivo, presentamos dos trabajos; un artículo principal (Nature 2020) y un artículo secundario (Astrophysical Journal Letters 2013). En nuestro artículo principal, buscamos hielo de agua dentro de unos cantos rodados cometarios que se encuentra en la superficie del cometa 67P / Churyumov-Gerasimenko. Aplicamos múltiples técnicas de análisis de datos para procesar observaciones de múltiples longitudes de onda producidas por el orbitador Rosetta fusionadas con mediciones in situ del módulo de aterrizaje Philae. El objetivo es identificar el hielo y caracterizar sus propiedades físicas, en particular su resistencia a la compresión y su porosidad. En el caso del articulo secundario, buscamos actividad cometaria alrededor de un Main-Belt Comet (MBC - un asteroide que muestra el comportamiento cometario, por ejemplo, coma, cola), estimamos su tamaño y buscamos una exosfera de agua.

Para abordar el segundo objetivo, presentamos tres artículos; un artículo principal (Astrophysical Journal Letters 2020) y dos artículos secundarios (Nature 2014 y Astrophysical Journal Letters 2013). Estos tres artículos se centran en la búsqueda de hielo de agua presente en la superficie / sub-superficie de los asteroides vinculados a su tamaño relativo. Si bien el artículo principal estudia el caso de dos de los

asteroides más grandes en el cinturón principal, a saber (24) Themis y (65) Cybele, los dos artículos secundarios cubren tanto el asteroide más grande, el planeta enano (1) Ceres, como uno de los asteroides más pequeños, Main-Belt Comet P / 2012 T1, que se mencionó anteriormente ya que también apoya el primer objetivo. En los tres artículos, buscamos una exosfera de vapor de agua utilizando el Instrumento Heterodino en el Observatorio Espacial Herschel (HIFI). Respaldamos nuestros resultados HIFI con datos de otros observatorios / instrumentos (VLT / FORS2, Herschel / SPIRE, Subaru / COMICS), así como también aplicamos diferentes modelos para ayudar en la comprensión de nuestros resultados. En el caso de estos artículos secundarios, también presentamos en esta tesis los avances científicos logrados desde que los publicamos.

Los resultados obtenidos de los trabajos presentados en esta tesis son bastante singulares. El resultado de nuestro primer artículo fue que pudimos confirmar la presencia de hielo primitivo (el estado químico de los materiales cometarios cuando comenzaron a aglomerarse/acumularse en cuerpos macroscópicos - ver Anexo F4) dentro de los cantos rodados cometarios, justo debajo de su superficie polvorienta. Determinamos la suavidad de este hielo primitivo y obtuvimos una porosidad equivalente a la medida en el cometa en su conjunto. Si bien el hielo de agua generalmente está expuesto en el cometa a través de fracturas térmicas que rompen el exterior cubierto de polvo que conduce a explosiones y chorros, en nuestro caso se confirmó que el hielo estaba expuesto por los movimientos del módulo de aterrizaje Philae durante su rebote en la superficie. Para nuestro segundo artículo, la no detección de una exosfera alrededor de los asteroides (24) Themis y (65) Cybele llevó a nuestro cálculo de límites superiores altamente sensibles para la tasa de producción de agua. Estimamos que el hielo de agua íntimamente mezclado con el material de la superficie oscura de los asteroides cubriría <0,0017% (para Themis) y <0,0033% (para Cybele) de sus superficies, mientras que una mezcla “areal” con hielo muy limpio cubriría <2,2%. Basándonos en este bajo porcentaje de cobertura de superficie, refutamos los resultados de un artículo de Nature (Campins et al. 2010) que proponía un vínculo entre la característica de absorción de 3.1 μm y el hielo de la superficie de los asteroides.

Con nuestro primer artículo secundario, fuimos los primeros en confirmar la presencia de hielo de agua en el cinturón de asteroides cuando descubrimos en 2013 que el planeta enano (1) Ceres tenía una exosfera producida a partir de la sublimación de $<1 \times 10^{-7}$ m^2 de agua superficial hielo. En nuestro segundo artículo secundario, no detectamos una exosfera a pesar de que el Main-Belt Comet estaba “activo” en el momento de la observación de Herschel. Nuestra no detección nos permitió derivar límites superiores sensibles en la tasa de producción de agua, así como estimar una cobertura de superficie de hielo de agua del 0.2%.

Cerramos la tesis presentando nuestras conclusiones y proponiendo trabajos futuros en este ámbito. La presencia de hielo de agua en los cometas y en el asteroide más grande del sistema solar ha sido confirmada a partir de los estudios realizados en esta tesis. La composición física y los procesos en juego para exponer este hielo de agua se han discutido en detalle. Sin embargo, para los asteroides de tamaño

<300 km, la confirmación directa del hielo de agua superficial y subterráneo sigue siendo difícil de alcanzar. Con el lanzamiento de JWST (James Webb Space Telescope), así como la construcción de observatorios terrestres más grandes y sensibles, se espera que se pongan en marcha nuevas técnicas para superar los límites para lograr tales detecciones.

TABLE OF CONTENTS

Chapter 1

Introduction

1.1 The current understanding on the presence of water ice on comets and asteroids

1.1.1 The importance of water and its prolificacy in the Solar System

The presence of water is considered one of the key ingredients for the formation of life on the Earth. Indeed, current theories as to the origin of the Earth's ocean define that the water located there originated from comets and asteroids, with the exact fractional contribution still under discussion (Delsemme, 2000; Morbidelli et al. 2000, Meech et al. 2020). On the Earth, water can be found in vapour, liquid and ice forms as well as being bound into minerals.

But water is not unique to the Earth; it has been found on the moon hidden deep inside a polar crater as well as its fragment OH is contained in moon regolith (Sunshine et al. 2009; Pieters et al. 2009; Clark 2009)). Water is prevalent throughout the outer solar system with it making up to 66% of the mass of Uranus and Neptune as well as being present on others in the form of vapour (Larson et al. 1975; Encrenaz et al. 1999). It has also been found on the moons of planets (Clark et al. 1984), on Kuiper Belt Objects (KBOs) (Brown et al. 1997) as well as on comets (Bregman et al. 1988; Brooke et al. 1989) in the form of ice.

Like on Earth, water can be found bound into minerals (as well as at the polar caps) on Mars (Sinton, 1967; Blaney, 1991), Europa (McCord et al. 1999), and on asteroids (Lebofsky, 1978; Feierberg et al. 1981). With asteroids identified as being the parental bodies of meteorites, evidence of early heating sufficient to melt the internal ice and produce varying degrees of aqueous alteration has been found (e.g. DuFresne and Anders, 1962) creating hydrated minerals as a result.

1.1.2 Status of detection of water ice on comets (prior to this thesis)

Comets are generally small in size with irregularly shaped nuclei composed primarily of inorganic, non-metallic, porous and heterogeneous materials such as carbon and silicates, mixed with icy grains. The icy grains can be made up of water, carbon dioxide and other gases with increasing degrees of volatility.

Although known to contain a significant amount of water ice in their interior, only a few published papers recording a direct detection of solid ice features in comets exist. Such detections have been made in the coma (Davies et al. 1997; Kawakita et al. 2004; Yang et al. 2009, 2014) using ground-based observatories.

For in-situ observations made by spacecraft, surface ice detections (Sunshine et al. 2006; A'Hearn et al. 2012; Protopapa et al. 2014; De Sanctis et al. 2015) are worth noting stemming from observations made by Deep Impact and Rosetta for example.

As the Rosetta satellite has been the only mission to orbit a comet and as such has providedspectroscopic data of the ice content of its nucleus, most of the existing knowledge of ices present on comets originates from Ground Based spectroscopic observations of emission lines and bands of the gas coma. More details are provided in section 1.3.

1.1.3 Status of detection of water ice on asteroids (prior to this thesis)

Very few detections of surface ice on asteroids have been made and published, although evidence of hydrated minerals (any mineral containing H_2O or OH) abound (Rivkin et al. 2015).

We begin our review starting with the largest body in the asteroid belt, Dwarf Planet (1) Ceres. Models produced in 1989 (Fanale & Salvail, 1989) pointed to the possibility of polar caps being present on (1) Ceres with evaporated water being replenished from its interior. At the distance of Ceres from the sun (perihelion at 2.55 AU and aphelion at 2.98 AU) water ice sublimation may be significant. The presence of an exosphere around Ceres created by water ice was confirmed in the sub-mm by Küppers & O'Rourke et al. (2014 – see Chapter 4.1 and Annex A). This significant result – the first unambiguous detection of water ice in the asteroid belt – served as an important input to NASA's Dawn mission which arrived to orbit Ceres in 2015. Prettyman et al. (2017) from that mission found that the regolith, at mid-to-high latitudes, contained high concentrations of hydrogen, consistent with broad expanses of water ice. In addition, water ice was detected on its surface (Combe et al. 2016). Chapter 4.1 discusses in more detail the evolution from 2014 to present day of the implications of our finding of water ice on Ceres.

Two asteroids in the ~ 200-300 km diameter range, (24) Themis and (65) Cybele, are important to flag. A rounded 3.1 μm band shape has been found on (24) Themis (Fornasier et al. 1999; Rivkin & Emery, 2010; Campins et al. 2010) and on (65) Cybele (Licandro et al. 2011) as well as on numerous others e.g. (76) Freia (Hargrove et al. 2012) and (361) Bononia (Usui et al. 2019). This 3.1 μm absorption feature was found to correlate well with laboratory experiments suggesting (Rivkin & Emery 2010) that a fine coating of ice on pyroxene grains mixed with amorphous carbon was covering the entire surface of these asteroids. Many members of the Themis family also show evidence for hydration (Florczak et al. 1999; Takir and Emery, 2012), while detections of water (again 3.1 μm feature) and/or hydroxyl on large asteroids have been reported for (175706) 1996 FG3 (Rivkin et al. 2015), (16) Psyche (Takir et al. 2017), and (433) Eros and (1036) Ganymede (Rivkin et al. 2017).

Moving to asteroids in the km to 10s of kms scale, the detection of water ice becomes very difficult to achieve as they are too faint for ground based spectroscopy in the 3 μm region. The discovery of "Main-Belt Comets" (MBCs, Hsieh and Jewitt, 2006) changed this view. These are asteroids that show cometary

activity behaviour linked to sublimation, pointing therefore to water ice being present on/under the surfaces of small objects in the asteroid belt. An MBC is defined in our study as any asteroid located in the near-Earth or main belt asteroidal populations that is observed to lose mass via sublimation processes, normally through the observation of a dust tail or trail, and that is believed to have formed in those orbits rather than originating from one of the cometary reservoirs. In that respect, we do not consider objects in the main asteroid belt where their dust tail/trail has been found to be due to significant impacts e.g. (596) Scheila (Bodewits et al. 2011, Jewitt et al. 2011 and others) and P/2012 F5 (Gibbs) (Stevenson et al. 2012; Moreno et al. 2012).

There have been 14 Main-Belt Comets discovered up to today, with the first 133P/Elst–Pizarro discovered in 1996. P/2016 J1 is particularly interesting as it was observed to split into two pieces (Hui et al. 2017; Moreno et al. 2017), and its initial activity was possibly triggered by a small impact, leading to ice previously buried under the surface starting to sublimate resulting in a spin-up whose torque led to a fragmentation event (Hui et al. 2017). Chapter 4.2 discusses in more detail the evolution from 2013 to present day of the search for Main-Belt Comets taking into account the O'Rourke et al. (2013a) MBC paper.

1.2 How and from where did comets and asteroids obtain their water ice?

1.2.1 The snowline and solar system formation models

The traditional understanding of the structure of our Solar System is that there is an inner region that is home to the terrestrial planets and rocky asteroids, and an outer region consisting of gas and ice giant planets and icy small bodies.

The outer region extends almost one third of the distance to the nearest star as the majority of the icy small bodies (comets) consisting of water ice, carbon dioxide and many super volatiles are located in the Edgeworth-Kuiper belt and in the Oort Cloud. Both of these represent reservoirs feeding the solar system with comets e.g. the Jupiter family comets are comets that have been captured when passing by Jupiter and fly in orbits that travel up to the Jupiter orbit, for example 67P/Churyumov-Gerasimenko.

If we move back closer to the sun, the two quite distinct regions mentioned in the first paragraph are separated by the 'snow line', which represents the distance from the Sun beyond which the ambient temperature allows icy bodies to be created and exist. The location of the snow line varies depending on the model under study. Its location, coinciding with the asteroid belt, is consistent with observations of planetary disks around other stars (Su et al. 2013) where extensive rings of potentially icy planetisimals have been observed, coinciding with the snow line around those stars (approximately between 3 and 3.5AU). Dynamical models suggest however that the location and contents of the asteroid belt of today may be very different to when it actually formed. Indeed these models define a three phased approach to reach its current day structure and location.

The first phase started during the lifetime of the gaseous protoplanetary disk when the giant planets formed. The model describing this phase is known as the "Grand Tack" model (Walsh et al. 2011). It interprets the low-albedo asteroids as originating among the giant planets, with later delivery to their current positions in the main asteroid belt by the migration of both Jupiter and Saturn. With Jupiter initially moving inwards in the solar system, it would have altered the outer asteroid belt (scattering objects behind it) while leaving the inner belt intact. Once Saturn moved into resonance with Jupiter, leading to both starting an outward migratory movement, not only would the previously scattered objects be thrown back once more into the asteroid belt region, but also icy volatile rich objects located closer to 5AU would have accompanied them. This would therefore have led to a rather diverse asteroid belt containing dry objects in the inner part and ice containing objects being present in the outer region. Such movements contribute to explaining how high and low temperature materials are found side by side in the asteroid belt.

The second phase occurs later, after the removal of the gaseous protoplanetary disk (approximately 4 G.y. ago). This phase is described by the "Nice Model" (Gomes et. al. 2005; Morbidelli et al. 2005), which has gained wide acceptance. It predicts a large influx of volatile-rich objects from the outer solar

system to the inner solar system and the insertion of primitive trans-Neptunian objects into the outer asteroid belt (Levison et al. 2009) due to Uranus and Neptune migrating outward. This would explain also the increased impact rate on the Moon determined to have occurred during the Late Heavy Bombardment period.

The third phase which covers the period between the giant planet migrations up to present day is described by Morbidelli et al. (2013). In this phase, it is considered that nearly half the asteroid population was lost via depletion taking place at unstable resonances with the giant and terrestrial planets, mostly during the subsequent 100 m.y. after late planet migration took place.

All these models aid in explaining how the solar system was formed, yet they are still only models driven by the input parameters and assumptions that build them. By providing more solid "measurement based" results, we can aid to fine tune these models. A study of the distribution of icy volatile rich bodies, especially those containing water ice, serves as one way to provide constraints on the models.

The models above discuss how the solar system itself is formed. Other models specifically covering planetesimal formation & growth i.e. how the asteroids & comets were formed from the basic building blocks of dust and gas (Morbidelli et al. 2009, Blum et al. 2017, Davidson et al. 2016), will not be addressed in this specific thesis.

1.2.2 Explaining the presence of water on comets

Comets are believed to have experienced very little alteration since their formation in the coldest regions of the young Solar System, with a number of different formation theories existing. As a result, comets are considered to be best source to study the physical conditions of the outer solar nebula as they contain the original water ice and volatiles present from their formation.

1.2.3 Explaining the presence of water on asteroids

While the presence of water and other volatiles in comets can be linked directly to the solar system formation, the case for its presence (or Hydroxol derivatives) on asteroid surfaces is more difficult to explain. The current hypothesises on this provides three possible reasons:

1. The formation of asteroids in an ice-rich environment, as discussed in the section 1.2.1.
2. Space weathering processes involving the interaction of solar wind protons with regolith resulting in water, OH and the accompanying 3-μm absorption band; such processes have been used to explain the significant OH detection on the moon (Pieters et al. 2009, Sunshine et al. 2009).
3. The delivery of such water via exogenic means i.e. low velocity impacts (or high impact for large asteroids) with carbonaceous or enstatite chondritic material (Reddy et al. 2012, Prettyman et al. 2012, Piani et al. 2020). These findings are in agreement with the weak 3-μm absorption band found in ground-based spectroscopy of Vesta by Hasegawa et al. (2003) and Rivkin et al. (2006).

1.3 A study of techniques used in the search for water ice

1.3.1 Direct versus indirect detection methods

While indirect means exist to search for H_2O on comets e.g. deriving a water production rate (Q) via a log based ratio linking Q_{CN} and Q_{OH} in "typical" comets, or by deriving a value for the dust production rate (Afρ) using visible light observations to estimate the coma brightness of a typical Jupiter Family Comet (O'Rourke et al. 2013b), we focus our attention in this chapter (and in this thesis) on the direct techniques in use.

While the majority of the remote sensing techniques below are focussed primarily on the search for water in a cometary coma e.g. in the search for water vapour from the Philae Touchdown 2 position (O'Rourke et al. 2020a), they have also been applied for studies of exospheres around asteroids (O'Rourke et al. 2020b), around Dwarf planets (Küppers and O'Rourke et al. 2014 – see Annex A) and around Main-Belt comets (O'Rourke et al. 2013a – see Annex B).

1.3.2 Detection techniques of Ultraviolet and Visible emission features

The photo-dissociation of water produces a significant amount of hydrogen in cometary comae, both directly and via a further dissociation of OH, with the Lyman-α transition representing one of the strongest emission features. It has the disadvantage that this detection can primarily only be done from space. While one could argue this is an indirect method as we search for a break-down products of water which could originate from other molecules, the fact that we identify the presence of O and H does provide greater confidence that water is present.

Emission lines from atomic oxygen in the UV, at 1304 and 1356 Å, are also only observable from space. Indeed they were detected by the Rosetta/ALICE instrument when close to comet 67P (Feldman et al. 2015), however the excitation process and the associated production rate, is highly model dependent. The Rosetta/ALICE instrument team performed a similar search in observations taken of the Touchdown 2 location described in O'Rourke et al. (2020a), however no detection was made.

Further to this, in the ultraviolet range the most prominent group of OH lines is in the 3070–3105 Å region (Swings et al. 1941) and it is this emission that is most often used to estimate the water production rate of comets, via spectroscopy or photometry.

At optical wavelengths, it is possible to detect the emission bands of OH, the direct product of water photo-dissociation. While atomic oxygen emissions are detected through three forbidden oxygen lines at 5577.339 Å for the green line and 6300.304 and 6363.776 Å for the red doublet, their detection is challenging and cannot be done for all comets. Observations of (24) Themis produced by McKay et al.

(2017) of these emission lines represented the best upper limits available until those of the O'Rourke et al. (2020b) paper (see Chapter 3) were published.

1.3.3 Detection techniques of Infrared and Sub-mm/radio emission features

There exists a large number of molecular species in the gas comae of comets, including water, that produce emission features in the infrared (Bockelée-Morvan et al. 2004; Cernicharo and Crovisier 2005) and in the sub-millimetre (Biver et al.2007; Bockelée-Morvan 2008). These species are detected by their vibrational and rotational modes. The advantage of observing in this region is that water is directly detected, rather than production rates being derived via daughter species.

For species like CO_2 or the sub-mm lines of water that cannot be observed from earth, observations are best performed using space based telescopes. Indeed some of the most sensitive observations have been made in these wavelengths by the Akari satellite (Ootsubo et al. 2012), by the International Space Observatory (ISO) satellite (Colangeli et al. 1999; Crovisier et al. 1997) and by the Deep Impact spacecraft (Feaga et al. 2014).

Further to this, the most sensitive detection of the rotational lines of water was made by the MIRO instrument (Biver et al. 2015) on the Rosetta spacecraft in its approach to comet 67P. This same instrument was used in support of the O'Rourke et al. (2020a) observations of the Philae Touchdown 2 point (see Chapter 2); although the instrument did detect water vapour above the region flowing an average of 0.39 km/sec away as well as a water column density of $9.4\pm 0.4 \times 10^{13} mol/cm^2$ in the MIRO beam, the results could not be pinpointed to the specific location where Philae touched down.

At sub-mm and radio wavelengths very high resolution spectroscopy is possible, enabling detection of spectrally resolved individual rotational lines which are key to determining the kinematics of gas flows and excitation conditions in the coma.

Using large dishes e.g. 30 m IRAM telescope, or arrays (ALMA), a large number of molecules, hydrocarbons in particular, have been identified and published for comets (Biver et al. 2010). In O'Rourke et al. (2013b), where we used IRAM to search for CO on Comet ISON, we obtained a marginal detection.

The launch of far-infrared (sub-mm) space telescopes, in particular Odin and Herschel, allowed observations of several ortho- and para-water lines (e.g. at 557 & 1113 GHz; de Val-Borro et al. 2010, 2014; Hartogh et al. 2010; Biver et al. 2012). The high-resolution Heterodyne Instrument for the Far Infrared (HIFI; de Graauw et al. 2010) instrument on the Herschel Space Observatory (located at L2) represented the most sensitive instrument (to date) in measuring water. Its importance in measuring the Deuterium/Hydrogen ratio of comet 103P, finding it equivalent to that found in the Earth's oceans, was extraordinary (Hartogh et al. 2011).

This same instrument was used in finding water vapour around (1) Ceres (Küppers and O'Rourke et al. 2014 – see Annex A), for providing upper limits for water vapour on (24) Themis and (65) Cybele (O'Rourke et al. 2020b – Chapter 3 of this thesis) disproving that the 3μm absorption band was due to surface ice on these asteroids, as well as providing a sensitive upper limit for the water ice on the surface of a Main-Belt Comet (O'Rourke et al. 2013a – see Annex B) when that object was confirmed to be still active.

Finally at very long (radio) wavelengths, there is an OH emission at 18 cm with two lines (1.665 and 1.667 GHz) regularly observed in comets, especially using the Nançay array (Crovisier et al. 2013).

1.3.4 Detection techniques of absorption features from hydrated minerals, surface ice and coma ice grains

By observing the absorption features in the reflected solar continuum, it is feasible to detect water ice directly on surfaces of small bodies (comets or asteroids), or in the grains of the cometary comae.

Water ice in general can come in two forms, namely amorphous and crystalline. These forms are linked to the temperature and pressure at the time of their formation (Petrenko and Whitworth 1999), in that if the formation temperatures were < 50 K then the water would have frozen into its amorphous phase but at a warmer temperature of 120 to 180K, the water molecules tend to arrange themselves into a crystalline structure (Mukai 1986).

Amorphous ice is very difficult to observe from remote-sensing observations which is why there have been no detections confirmed. In the case of crystalline ice, there are two key infrared bands in use; one is at 3.1 μm caused by a stretching mode of the water molecule, and the other is a temperature-sensitive absorption band at 1.65 μm – that is specific to crystalline ice (Grundy and Schmitt 1998) although rarely observed.

Most of the direct evidence for the presence of hydrated minerals and surface water ice found on asteroids comes from visible and infrared observations.

The wide range of hydrated minerals found on asteroids aid in understanding which meteoritic groups they belong to. In that respect, because absorption features from hydrated minerals are often the only ones that appear in reflectance spectra of low-albedo asteroids, their presence provides one of the few means of determining asteroidal composition through remote sensing.

Absorption features observed throughout the visible and the near-IR are due to hydrated minerals but their visibility is limited from ground based observatories due to the telluric spectral absorption bands present in the atmosphere. In that respect, space based observatories are needed to circumvent this issue.

Two spectral regions in particular, namely the 3-μm region (2.4–3.6 μm), and the visible region between 0.4–0.9 μm, have been the focus for studies of hydrated minerals on asteroids.

Takir & Emery 2012 examined the distribution and abundance of hydrated minerals on 28 outer main belt asteroids and proposed four 3 μm spectral groups based on the absorption shapes observed: Ceres-like, Europa-like, rounded and sharp. Of the four absorption shapes, only the rounded 3μm band shape has been linked to the presence of water ice on the surface. We have found however in O'Rourke et al. (2020b) that the absorption feature located at the 3.1 μm band cannot be due to surface ice and we speculate that it could in fact be due to ammonium salts (see Chapter 3).

Indeed the 3-μm region is known to host other volatile species that do show similar absorption curves. The ammonium (NH^{4+}) ion has a band centre near 3.1 μm and was interpreted to be present in the (1) Ceres spectrum (King et al. 1992). Poch et al. (2020) have recently compared the 3.2 μm spectra of ammonium salts found on comet 67P (Altwegg et al. 2020) with the 3.1 μm feature on Themis and Cybele finding a distinct correlation between the two. Similar features have been observed on the Jupiter Trojan asteroids and the small moon Himalia matching with ammoniated minerals on their surface (Poch et al. 2020; Brown 2016) at this wavelength. Further to the above, minerals such as Brucite (Beck et al. 2011), magnetite (Yang & Jewitt, 2010) and adsorbed water molecules in lunar regolith (Clark 2009) all represent other possible alternative explanations to the presence of surface water ice.

1.3.5 In-situ detection techniques of water ice

The final set of techniques to detect water are those from in-situ measurements generated from instruments on board a spacecraft orbiting or performing a flyby of an asteroid or comet.

Of the significant list of spacecraft that have performed this feat, one stands above the rest when it comes to the in-situ search and detection of water from a cometary surface and that is the Rosetta spacecraft (Glassmeier et al. 2007). Launched in 2004, it took 10 years to travel to and rendezvous with comet 67P/Churyumov-Gerasimenko. Rosetta was very much a flying laboratory designed and constructed to study a comet using its suite of 17 in-situ and remote sensing instruments. In addition to Rosetta's instruments, the Philae lander itself had another 10.

In O'Rourke et al. (2020a) – see Chapter 2 of this thesis - numerous instruments from the Rosetta spacecraft and the Philae Lander were combined to produce a definitive detection of water ice on the surface of the comet. The OSIRIS and VIRTIS instruments proved essential in confirming that the ice visible on the surface (exposed by Philae) was water ice. Combining this knowledge with magnetometer instruments on both Rosetta (RPC-MAG) and the lander (ROMAP) allowed a measurement to be made of the compressive strength of that ice and indeed aided in deriving the porosity.

Besides the instruments which can search for surface ice or outgassing water, there are others that can search for evidence of buried ice. For the Rosetta mission, there was one which did just that i.e. CONSERT Radar. It was located on both of the spacecraft and the Philae Lander. The depth at which radar can detect echoes from a subsurface interface is affected by the properties of the material between the surface and the interface. The CONSERT measurements (Kofman et al. 2015) gave direct information about the permittivity of the comet nucleus and its spatial structure. The permittivity is a function of several properties of the nucleus: porosity, composition of the material, temperature, internal structure, and/or scale of potential heterogeneities. From the propagation time and form of the signals, the upper part of the "head" of 67P was found to be fairly homogeneous on a spatial scale of tens of meters. A porosity of the internal structure was determined to be between 65% and 85%, (Herique et al. 2019). This can be compared to the porosity derived by O'Rourke et al. (2020a) which provides a more precise value between 68% and 82%. In addition, the high ice-to-dust ratio found by CONSERT was found also in the crevice in O'Rourke et al. (2020a).

1.4 Main Objectives and Description of this work

This thesis has as its main goal to search for the presence of ice (primarily water ice) on and just below the surfaces of both comets and asteroid, estimate its coverage and where feasible characterise its properties focussing on subsurface dynamics, sublimation limits, and cleanliness of the ice. This goal can be broken down into two main objectives:

- The first objective focusses on the search for and characterisation of surface/subsurface ice on comets.
- The second objective focusses on the search for and characterisation of surface/subsurface ice on asteroids.

In Chapter 1, we have presented the current state of investigations performed to find water ice on comets and asteroids. We introduced the techniques used to find surface/subsurface ice and flag how these techniques have been used in the published works presented in this thesis.

In Chapter 2 (O'Rourke et al., 2020a), we present the Nature publication "The Philae lander reveals low strength primitive ice inside cometary boulders". This chapter is linked to the first of the two objectives of the thesis: The search for and characterisation of surface/subsurface ice on comets. The paper presents in-situ measurements taken on the surface of comet 67P/Churyumov-Gerasimenko by the Philae Lander, of ice contained in two cometary boulders. These measurements derive never before obtained in-situ compressive strength measurements of the primitive (the chemical state of cometary materials as they began to agglomerate/accrete into macroscopic bodies – see Annex F4) ice contained in their interior as well as deriving its porosity. In this paper, we used multi-wavelength observations merged with in-situ measurements to identify water ice, its location/visibility when compared with other ice patches found on the comet, determine its dust-to-ice ratio, and characterise the physical properties of the original primitive ice including compressive strength and porosity.

In Chapter 3 (O'Rourke et al., 2020b), we present the Astrophysics Journal Letters publication "Low Water outgassing from (24) Themis and (65) Cybele – 3.1 μm NIR spectra implications". This chapter is linked to the second of the objectives of the thesis: The search for and characterisation of surface/subsurface ice on asteroids. In this paper we investigated two of the larger asteroids in the main asteroid belt with sizes between 200 and 300 km. We use the HIFI instrument on the Herschel Space Observatory to search for an exosphere allowing us to confirm (or otherwise) the presence of surface/subsurface water ice. Further to this we investigate with this result whether the 3.1 μm Near Infrared absorption feature considered synonymous with the presence of water ice is actually due to water ice.

In Chapter 4, we introduce two previously published supporting papers (attached in the Annex section of the thesis) that very much relate to the two objectives above whereby they contribute important results related to the search for and characterisation of surface/subsurface ice on the largest asteroid (950 km) and

one of the smallest (<2.6 km). The smaller size complements nicely with the sizes found for comets. In addition, the fact that this small asteroid showed cometary activity makes it relevant to the first objective also. The first supporting paper (Küppers, M., O'Rourke L., et al., 2014) was published in 2014 in Nature and titled "Localized sources of water vapour on the dwarf planet (1) Ceres". This paper presents the search for water vapour on the largest asteroid in the asteroid belt. At the time of this Nature paper's release, there had been no water ice discovered in the asteroid belt thus it had a significant impact in the area of planetary science. The second supporting paper (O'Rourke et al., 2013), was published in 2013 in Astrophysics Journal Letters and titled "Determination of an upper limit for the water outgassing rate of Main-Belt Comet P/2012 T1 (PANSTARRS)". This paper presents observations performed on Main-Belt Comet (MBC) P/2012 T1 that was an asteroid in the main belt that showed cometary activity. It was discovered in October 2012. Our aim was to determine if the activity was indeed cometary in nature by searching for water vapour in the coma surrounding the MBC.

In Chapter 5, I draw my conclusions and discuss about future work and perspectives.

Finally, in the Annexes, I provide a copy of the two previously published papers, a brief overview of the observatories/instruments used in my work, the bibliography for this thesis, and also further supplementary methods and figures related to the Nature paper presented in Chapter 2.

Chapter 2

The Philae Lander reveals low strength primitive ice inside cometary boulders

This chapter is linked to the first of the objectives of the thesis whereby we search for and characterise ice found on the surface and subsurface of comets. The article covered in this chapter "The Philae lander reveals low strength primitive ice inside cometary boulders", was published in Nature on October 28th 2020. In the bibliography, it is referenced as O'Rourke et al. 2020a.

Prior to the publication of this paper, surface ice detections (Sunshine et al. 2006; A'Hearn et al. 2012; Protopapa et al. 2014; De Sanctis et al. 2015) had been made on comets based on observations made by Deep Impact and Rosetta for example. Indeed Rosetta observed multiple outbursts across the comet linked to newly exposed ice reacting with the sun resulting in a plume of gas and dust being released "violently" from the surface of the comet. Up to the release of this new paper, no direct inspection of the interior of a cometary boulder nor indeed an in-situ measurement of the strength of primitive cometary ice had ever been made. An unambiguous link between the porosity of ice inside cometary boulders with that arising from the interior of the comet was also never shown.

The paper presents in-situ measurements taken by the Philae Lander on the surface of comet 67P/Churyumov-Gerasimenko which identifies primitive ice contained within two cometary boulders. These measurements are used to determine the in-situ compressive strength measurements of the ice contained in their interior. Further to this, using two instruments from the Rosetta orbiter, we have been able to determine that the ice remaining 19 months after exposure by Philae is water ice with a very low local dust-to-ice mass ratio of $2.3^{+0.2}_{-0.16}$: 1, equivalent to levels observed in newly exposed water ice during outbursts. Finally we derived a porosity for this ice (75±7%) equivalent to that found for the ice in the interior of the comet by other instruments from Philae (Consert Radar) and Rosetta (RSI).

This paper shows the unique benefits of merging science and engineering techniques with multi-wavelength observations from multiple instruments.

NOTE: The supplementary figures 1 to 8 referred to in the following pages are provided in Annex F of this Thesis. Similarly, certain supplementary methods have also been provided.

Article

The Philae lander reveals low-strength primitive ice inside cometary boulders

https://doi.org/10.1038/s41586-020-2834-3

Received: 7 April 2020

Accepted: 28 August 2020

Published online: 28 October 2020

Check for updates

Laurence O'Rourke[1]✉, Philip Heinisch[2], Jürgen Blum[2], Sonia Fornasier[3,4], Gianrico Filacchione[5], Hong Van Hoang[3,6], Mauro Ciarniello[5], Andrea Raponi[5], Bastian Gundlach[2], Rafael Andrés Blasco[7], Björn Grieger[8], Karl-Heinz Glassmeier[2], Michael Küppers[1], Alessandra Rotundi[5,9], Olivier Groussin[10], Dominique Bockelée-Morvan[3], Hans-Ulrich Auster[2], Nilda Oklay[11], Gerhard Paar[12], Maria del Pilar Caballo Perucha[12], Gabor Kovacs[13], Laurent Jorda[10], Jean-Baptiste Vincent[14], Fabrizio Capaccioni[5], Nicolas Biver[3], Joel Wm. Parker[15], Cecilia Tubiana[5,16] & Holger Sierks[16]

On 12 November 2014, the Philae lander descended towards comet 67P/Churyumov–Gerasimenko, bounced twice off the surface, then arrived under an overhanging cliff in the Abydos region. The landing process provided insights into the properties of a cometary nucleus[1–3]. Here we report an investigation of the previously undiscovered site of the second touchdown, where Philae spent almost two minutes of its cross-comet journey, producing four distinct surface contacts on two adjoining cometary boulders. It exposed primitive water ice—that is, water ice from the time of the comet's formation 4.5 billion years ago—in their interiors while travelling through a crevice between the boulders. Our multi-instrument observations made 19 months later found that this water ice, mixed with ubiquitous dark organic-rich material, has a local dust/ice mass ratio of $2.3^{+0.2}_{-0.16}$: 1, matching values previously observed in freshly exposed water ice from outbursts[4] and water ice in shadow[5,6]. At the end of the crevice, Philae made a 0.25-metre-deep impression in the boulder ice, providing in situ measurements confirming that primitive ice has a very low compressive strength (less than 12 pascals, softer than freshly fallen light snow) and allowing a key estimation to be made of the porosity (75 ± 7 per cent) of the boulders' icy interiors. Our results provide constraints for cometary landers seeking access to a volatile-rich ice sample.

Fly-bys and rendezvous missions have been central to the provision of close-up images of cometary surface structures, delivering important insights into the chemical and physical processes that have defined them[7]. The presence of boulders on their surfaces with sizes ranging from the metre scale up to tens of metres—often in locations not matching where they were initially exposed—certainly points to the dynamic nature of their creation[8,9]. A determination of mechanical strength properties derived from in situ measurements carried out on the primitive ice located in the interior of a cometary boulder allows unique comparisons to be made with the cometary body internal structure. Furthermore, these properties provide information about the comet's dynamical history and deliver important constraints for the design of cometary landers and cryogenic sample return missions.

The European Space Agency's Rosetta mission[10] was launched in 2004 and began orbiting comet 67P/Churyumov–Gerasimenko in August 2014. On 12 November 2014, the Philae lander was released with a faulty harpoon system, touching down on the surface on two occasions while also experiencing a glancing collision against the Hatmehit depression edge. After touchdown 2 (TD2), it proceeded to its final position at touchdown 3 (TD3), located under an overhang in the Abydos region of the comet[1] (see Fig. 1a–d). Although scientific analysis of data[1,2,11] from Philae's first and third touchdown points have provided important insights into the properties of a cometary nucleus, the location and scientific implications stemming from the second touchdown point were unknown up to now. Its importance was noted[12], however, as Philae was found to have changed both velocity and rotation rate at this location, as well as having penetrated the surface with the Rosetta Lander Magnetometer and Plasma Monitor[13] (ROMAP) sensor, possibly exposing ice at the same time.

The production of a new Philae landing trajectory (Supplementary Methods, Supplementary Fig. 1) served to start the search for TD2, with a ridge region identified as being a likely candidate for its

[1]European Space Agency (ESA), European Space Astronomy Centre (ESAC), Madrid, Spain. [2]Institut für Geophysik und extraterrestrische Physik, Technische Universität Braunschweig, Braunschweig, Germany. [3]LESIA, Observatoire de Paris, Université PSL, CNRS, Université de Paris, Sorbonne Université, Meudon, France. [4]Institut Universitaire de France (IUF), Paris, France. [5]Istituto Nazionale di Astrofisica, Istituto di Astrofisica e Planetologia Spaziali, Rome, Italy. [6]Université Grenoble Alpes, CNRS, Institut de Planétologie et Astrophysique de Grenoble (IPAG), UMR, Grenoble, France. [7]Telespazio Vega UK Ltd for the European Space Agency (ESA), European Space Astronomy Centre (ESAC), Madrid, Spain. [8]Aurora Technology BV for the European Space Agency (ESA), European Space Astronomy Centre (ESAC), Madrid, Spain. [9]Dipartimento di Scienze e Tecnologie, Universitá degli Studi di Napoli Parthenope, Naples, Italy. [10]Aix Marseille Université, CNRS, CNES, LAM, Marseille, France. [11]Independent researcher, Berlin, Germany. [12]Joanneum Research Forschungsgesellschaft, Graz, Austria. [13]Department of Mechatronics, Optics and Engineering Informatics, Budapest University of Technology and Economics, Budapest, Hungary. [14]DLR Institute of Planetary Research, Berlin, Germany. [15]Planetary Science Directorate, Southwest Research Institute (SwRI), Boulder, CO, USA. [16]Max-Planck-Institut für Sonnensystemforschung, Göttingen, Germany. ✉e-mail: lorourke@esa.int

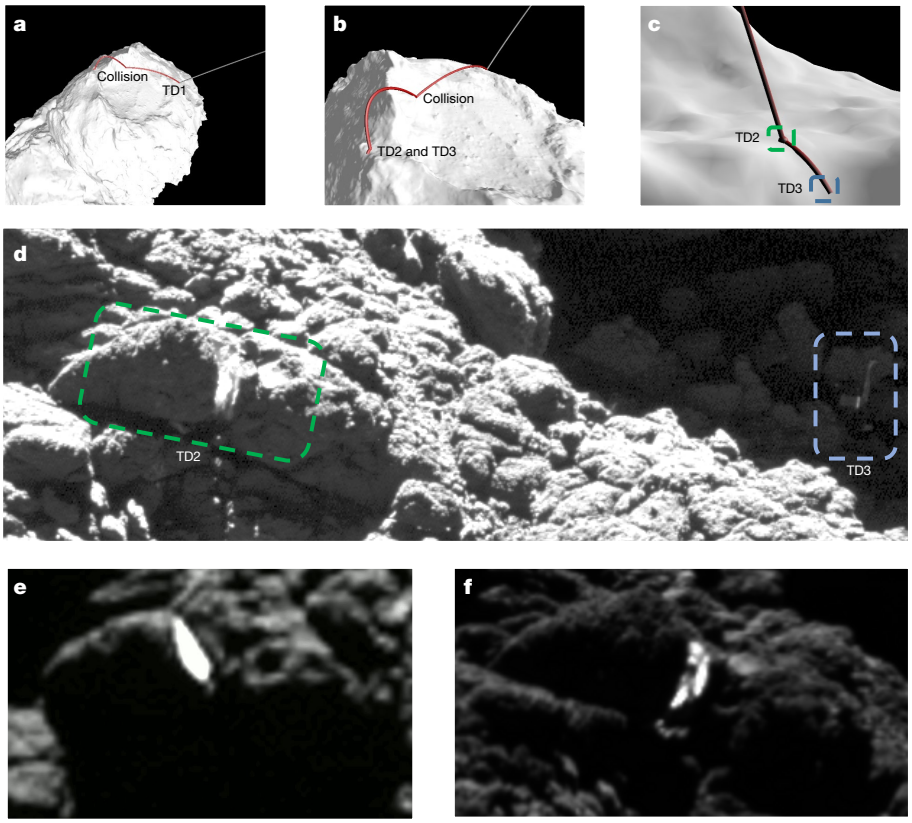

Fig. 1 | Philae landing trajectory, TD2 and TD3, Philae and visible ice. **a**–**c**, Three views showing the Philae landing trajectory as it crosses the surface of the comet (represented by a shape model) highlighting the locations of touchdown 1 (TD1), collision, touchdown 2 (TD2) and touchdown 3 (TD3). **d**, OSIRIS image (2 September 2016, 19:59 UT; 0.049 m per pixel), showing locations of TD2 and TD3 as boxed in **c**. This image is enhanced in order to show the skull-top crevice (inside the green dashed box marked TD2) and the Philae lander hidden in the distant shadows (inside the blue dashed box marked TD3). **e**, **f**, Views of the ice in the crevice (6 August 2016 and 24 August 2016, respectively).

location[11]. A comparative analysis was performed of this area using pre- and post-landing imagery (Supplementary Figs. 2, 4) from the Rosetta Optical, Spectroscopic, and Infrared Remote Imaging System (OSIRIS)[14], combined with high-resolution digital terrain models of the ridge (for example, Supplementary Figs. 9–11) and of the Abydos region as a whole. While notable changes in boulder positions were observed in the Abydos valley (Supplementary Fig. 4e, f), the geomorphological structures along the length of the ridge showed no differences with regards to position or orientation. Changes were found however in the pre- and post-landing surface morphology of two adjoining boulders located on the ridge (Extended Data Fig. 1, Supplementary Video 1, Supplementary Figs. 5, 6). These changes included the identification of an unusual ice feature located in the boundary between the boulders (Fig. 1e, f, Supplementary Video 2). Our analysis of these changes found that only Philae's presence could explain their existence (Supplementary Methods). As the topological structures of these two boulders, viewed from above, give the impression of a skull face as shown in Supplementary Fig. 3, we chose to name the location 'skull-top ridge' and the boundary between the two boulders as 'skull-top crevice'. We highlight in Methods that the boulders themselves represent assemblages of dust/ice aggregates.

The timing involved in this chain of events (Extended Data Table 2, Supplementary Video 3) was derived from magnetometer data produced by the ROMAP sensor and checked against thermal and power information from Philae's subsystems. The ROMAP instrument provided attitude information (combined with the Rosetta Plasma Consortium Fluxgate Magnetometer, RPC-MAG[15]), as well as unique accelerometer measurements based on sensor boom movement (see Methods). Combined with our image analysis, a reassessment of the ROMAP science data (see Methods and Supplementary Methods) determined that the initial contact took place at 17:23:48 ± 10 s UT, approximately 1.5 min before the previously published contact time[16]. Indeed Philae spent nearly two full minutes at TD2, making four surface contacts in its trip across it (see Supplementary Fig. 6). Of the four, the third (TD2c) of these contacts (Fig. 2) is the most notable due to the 0.25-m-deep depression visible in an ice-like feature on the side of the crevice. We found a perfect correlation between the presence of that depression and ROMAP boom movements (Fig. 2a) that shows the expected deviations matching the stamping movement required for its creation. The compression lasted 3 s (Fig. 2b, c) before Philae proceeded to rise out of the crevice to then make its final TD2 contact with the surface (TD2d), creating the 'eye' of the 'skull' in the process.

Data from the OSIRIS and VIRTIS (Visible, InfraRed and Thermal Imaging Spectrometer) instruments on the Rosetta orbiter were used to determine whether the high-albedo ice-like features observed in the skull-top crevice were water ice. For the OSIRIS instrument, we focused on multi-filter images generated during the timeframe of 12 to 14 June 2016 (Fig. 3a, Extended Data Fig. 2). A spectrophotometric analysis of the data sets from this period (see Methods) provided spatially resolved data that confirmed the presence of water ice in the crevice, matching a visible area of approximately 3.5 m^2, with a brightness 6 times greater than that of the dust-covered terrain. The water-ice abundance was derived from the observed reflectance, after corrections were made for the illumination conditions and phase function based on geographical mixtures of the comet's dark terrain and water ice (grain size of 30–100 μm) applied to the bright material's absolute reflectance[17]. A water-ice abundance value of 46.4% ± 2.0% was measured during the 14 June 2016 observations at 10:30:32 UT (Fig. 3c, d, Extended Data

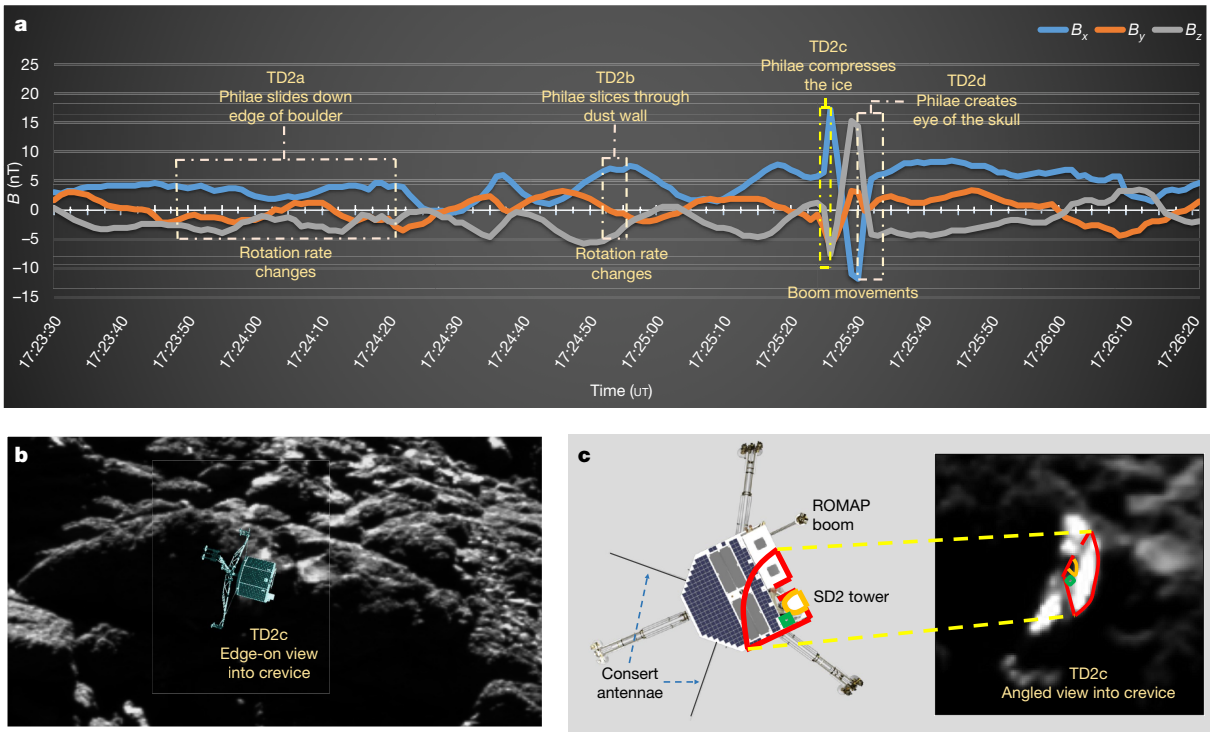

Fig. 2 | ROMAP guide and Philae impact TD2c. a, ROMAP magnetometer rotation and boom measurements matching Philae touchdown events (TD2a–d) are plotted as magnetic field values versus time (see Methods and Supplementary Methods) whereby B_x, B_y and B_z represent the three magnetic field components. **b**, OSIRIS image focussing on TD2c, where the lander (1 m width in the image) compressed the ice in the crevice (2 September 2016). **c**, Left, overhead view of the Philae lander highlighting its instruments. The red, orange and green markings map to the impression in the ice (right; OSIRIS image from 24 August 2016). See Supplementary Video 2 showing a fly-over of the crevice and Supplementary Video 3 for an animation of this figure.

Table 1), resulting in an approximate local dust/ice volume ratio of $1.15^{+0.1}_{-0.08}$: 1. Assuming a dust/ice bulk density ratio of two[18], and a similar porosity for dust and ice material, the local dust/ice mass ratio is approximately $2.3^{+0.2}_{-0.16}$: 1. This value is below the average dust/ice mass ratio for the nucleus, which is >3 for most estimates derived from measured data[19].

Lower spatial resolution data from the VIRTIS Instrument on 14 June 2016 confirmed this detection of water ice. Figure 3b shows the resulting hyperspectral image of the Abydos region with the skull-face crevice identified at the edge of the field of view. A signal from the ice located in the crevice was found in the tail of the optical point spread function (see Methods). An estimation by VIRTIS of the water-ice abundance in the location concurred with that of the OSIRIS measurement whereby the water-ice-rich spot was determined to have an approximate area of 1.27 ± 0.5 m^2 (matching the upper bound of 48% of 3.5 m^2), calculated from the inferred abundances (0.5% over an area of 253 m^2).

The general longevity of ice on the comet's surface is dependent on local surface topography[6,17,20,21], with most ice features disappearing quite quickly owing to limited surface shading from the Sun within days to weeks of discovery. Local dust/ice ratios of <3:1, equivalent to that in the skull-top crevice, have been found at other locations across the comet (as well as on other comets[7,22])—in particular, in newly exposed water ice observed on cliffs and scarps linked in some cases to outbursts as well as in clustered bright spots in both hemispheres[4,6,17]. As dust/ice ratios have been found to increase over time due to solar illumination exposure, the facts that our measurement of high water-ice abundance was made 19 months post-landing, and that the ice in the crevice was observed 22 months post-landing without notable measurable changes, both point to the ice in the crevice receiving very low solar illumination due to shadowing.

We confirmed this using a horizon mask (Extended Data Fig. 3), determining that the ice on the left-hand side of the crevice was illuminated <0.55% of the time during the perihelion passage while the ice on the right-hand side of the crevice, where the compression took place, received <0.21% of direct sunlight during the same period. Using as input the corresponding energy flux, we found our sublimation modelling over-estimated by an order of magnitude the amount of ice that sublimed (compared to that visible in the imagery), pointing to even greater morphological shadowing than our horizon mask could derive (Supplementary Methods). This very low illumination is supported by our direct measurements of the crevice dimensions; the width of the TD2c location matches the width of the Philae lander, thus pointing to very little sublimation or erosion having taken place (see e1 in Fig. 3e). For these reasons, we conclude that while the super-volatiles may have sublimed over time, the water ice itself at TD2c did not sublime and remained in a highly unprocessed state.

The depth of the impression made by Philae in this icy surface, combined with a detailed correlation of the ROMAP boom measurements, contribute to direct in situ measurements allowing an estimate to be made of the compressive strength of this dust/ice feature. The depth of the impression in the ice is 0.246±0.049 m (e2 in Fig. 3e) and its area is ≥0.2208 m^2 (see Methods). A detailed analysis was performed (Methods), and found the compressive strength of the ice to be <12 Pa. It is important to note that this very low compressive strength is of 'primitive' ice (see Supplementary Methods for explanation) buried and hidden from view until it was exposed and compressed at the time of the Philae landing itself.

Whereas compressive strengths[1,2] of 1 kPa and 2 MPa were measured at TD1 and TD3 respectively (although deployment uncertainties do affect the reliability of the MUPUS—Multi Purpose Sensors for Surface and Subsurface Science—penetrator result), a number of other publications find much lower values. Model-dependent analyses of the collapse of cliff overhangs observed from orbit[23], as well as those derived from the scratches Philae made at the final landing location[11], calculated

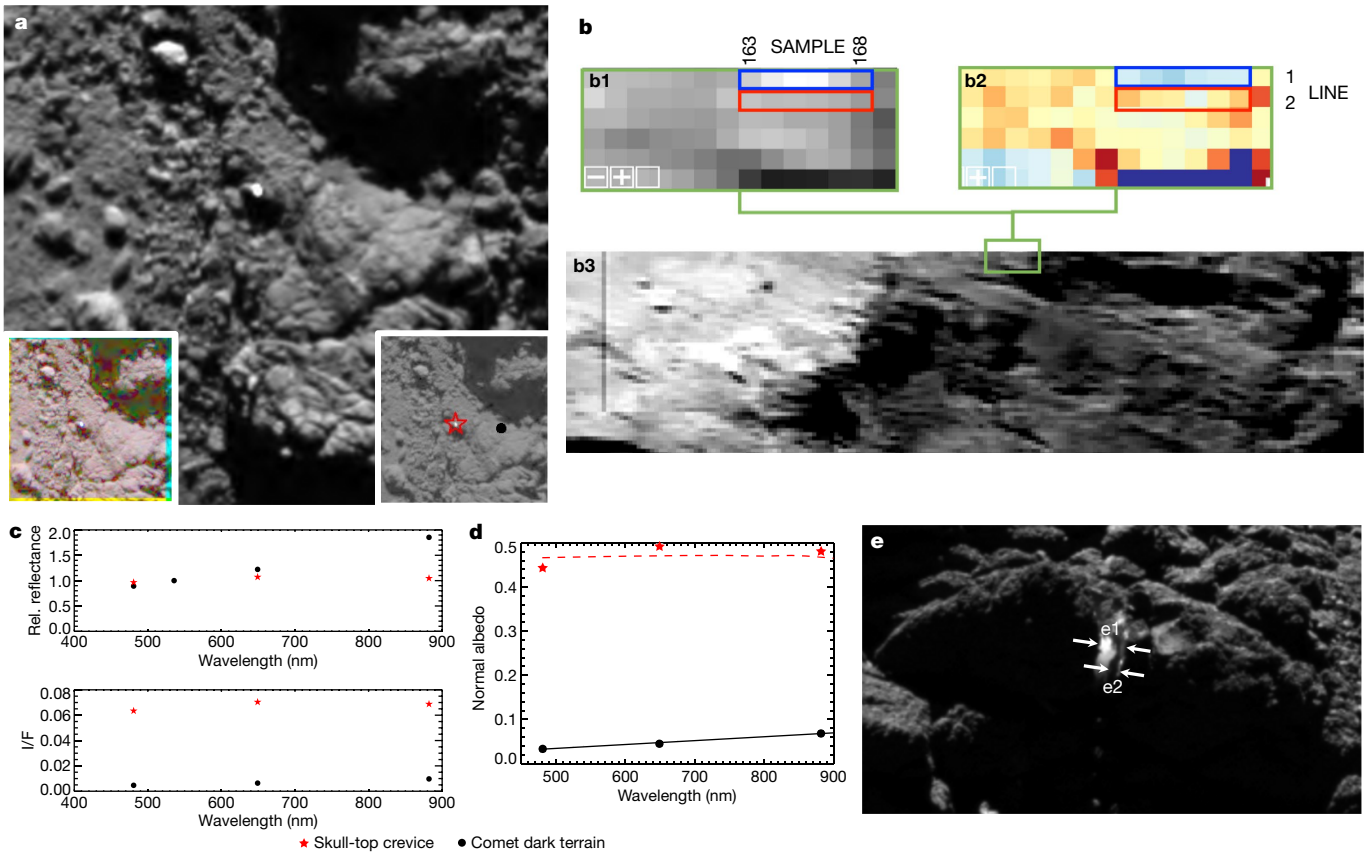

Fig. 3 | Multi-instrument view of the water ice. a, Main panel, NAC image (taken on 14 June 2014 at 10:29 UT); insets, OSIRIS images (left, multi-filter view; right, star and black dot show positions for plots **c**, **d**). **b**, The 0.55 µm VIRTIS-M hyperspectral cube (V1_00424522185.QUB) of the Abydos region (14 June 2016, 10:51–11:35 UT) with skull-top ridge located in the green box of the lower panel, b3. The upper panels b1 and b2 zoom-in on spectral slope (left) and the radiance factor (I/F) image (right), respectively. 'Sample' identifies the relevant pixel numbers in each 'Line' (row) of the cube. **c**, Plot of reflectance and I/F versus wavelength, and **d**, the measured albedo as a function of wavelength. **e**, OSIRIS image (2 September 2016) shows the crevice edge-on with e1 (crevice width) 1.03 ± 0.07 m and e2 (compression width) 0.246 ± 0.049 m.

compressive strength values ranging between 30 Pa and 150 Pa for the former and from 10 Pa to 100 Pa for the latter. Such model-based low compressive strength derivations show consistency with our in situ findings.

Three independent porosity estimations have been made for this comet, with values ranging from 65%–85% (Philae Consert radar[3,24]) to 70%–75% (Rosetta Radio Science Instrument)[25], and a modelled third estimate[26] of 63%–79%. These same numbers equate to volume filling factors of 0.15–0.35, 0.25–0.3 and 0.21–0.37, respectively.

We modelled the compression Philae made in the cometary boulder material, with the aim of determining how much the volume-filling factor of the material is altered. The model we use[27] assumes that the material making up the cometary interior is made up of a hierarchical arrangement of building blocks (see Supplementary Methods). According to this model, applied here to the interior of a cometary boulder, the submicrometre-sized solid grains[28,29] are contained in larger units ('pebbles'), which themselves are clustered together to make up the boulder.

We find that such an arrangement of hierarchical building blocks, which previously has demonstrated excellent correlation with the Philae Consert radar results[24], also provides the conditions needed to achieve the low compressive strength (<12 Pa) of the material of the boulder into which Philae stamped (see Methods). We further note that although the local dust/ice ratio we measured ($2.3^{+0.2}_{-0.16}$) is lower than the model-based average[30] estimate of the nucleus (between 3 and 9), we can resolve this inconsistency. A study of results from gas activity models[31,32] (based also on our hierarchical pebble model) explains our finding in that dust/ice ratios of 5 and lower can be found to be present locally for up to 5% of the volume of the nucleus[29]. As a result and on the basis of the consistencies found using our model, we derive a volume filling factor for the boulder material of 0.25 ± 0.07 (a porosity range of 68%–82%), equivalent to previously published values for the overall nucleus of comet 67P.

Our results provide important constraints for future cometary lander missions, as the knowledge of cometary boulder interiors is not only vital for impact analysis but also provides insights into the mechanical processes needed to retrieve a volatile-rich cryogenic sample for in situ analysis—or indeed for delivery back to the Earth[33,34]. The operational dangers of landing in a cometary boulder field would however need careful study and preparation.

Online content

Any methods, additional references, Nature Research reporting summaries, source data, extended data, supplementary information, acknowledgements, peer review information; details of author contributions and competing interests; and statements of data and code availability are available at https://doi.org/10.1038/s41586-020-2834-3.

1. Biele, J. et al. The landing(s) of Philae and inferences about comet surface mechanical properties. *Science* **349**, aaa9816 (2015).
2. Spohn, T. et al. Thermal and mechanical properties of the near-surface layers of comet 67P/Churyumov-Gerasimenko. *Science* **349**, aab0464 (2015).
3. Kofman, W. et al. Properties of the 67P/Churyumov-Gerasimenko interior revealed by CONSERT radar. *Science* **349**, aab0639 (2015).

4. Pajola, M. *et al*. The pristine interior of comet 67P revealed by the combined Aswan outburst and cliff collapse. *Nat. Astron*. **1**, 0092 (2017).
5. Fornasier, S. et al. Surface evolution of the Anhur region on comet 67P/Churyumov-Gerasimenko from high-resolution OSIRIS images. *Astron. Astrophys*. **630**, A13 (2019).
6. Oklay, N. et al. Long-term survival of surface water ice on comet 67P. *Mon. Not. R. Astron. Soc*. **469**, S582–S597 (2017).
7. Oklay, N. et al. Comparative study of water ice exposures on cometary nuclei using multispectral imaging data. *Mon. Not. R. Astron. Soc*. **462**, S394–S414 (2016).
8. Luccheti, A. et al. Characterization of the Abydos region through OSIRIS high-resolution images in support of CIVA measurements. *Astron. Astrophys*. **585**, L1 (2016).
9. Keller, H. U. et al. Seasonal mass transfer on the nucleus of comet 67P/Churyumov-Gerasimenko. *Mon. Not. R. Astron. Soc*. **469** (Issue Suppl. 2), S357–S371 (2017).
10. Glassmeier, K. et al. The Rosetta mission: flying towards the origin of the Solar System. *Space Sci. Rev*. **128**, 1–21 (2007).
11. Heinisch, P. et al. Compressive strength of comet 67P/Churyumov–Gerasimenko derived from Philae surface contacts. *Astron. Astrophys*. **630**, A2 (2019).
12. Heinisch, P. et al. Reconstruction of the flight and attitude of Rosetta's lander Philae. *Acta Astronaut*. **140**, 509–516 (2017).
13. Auster, H. U. et al. ROMAP: Rosetta magnetometer and plasma monitor. *Space Sci. Rev*. **128**, 221–240 (2007).
14. Keller, H. U. et al. OSIRIS — the scientific camera system onboard Rosetta. *Space Sci. Rev*. **128**, 433–506 (2007).
15. Glassmeier, K. et al. RPC-MAG, the fluxgate magnetometer in the ROSETTA plasma consortium. *Space Sci. Rev*. **128**, 649–670 (2007).
16. Auster, H. U. et al. The non-magnetic nucleus of comet 67P/Churyumov–Gerasimenko. *Science* **349**, aaa5102 (2015).
17. Fornasier, S. et al. Rosetta's comet 67P/Churyumov-Gerasimenko sheds its dusty mantle to reveal its icy nature. *Science* **354**, 1566–1570 (2016).
18. Fulle, M. et al. The dust-to-ices ratio in comets and Kuiper belt objects. *Mon. Not. R. Astron. Soc*. **469**, S45–S49 (2017).
19. Choukroun, M. et al. Dust-to-gas and refractory-to-ice mass ratios of comet 67P/Churyumov-Gerasimenko from Rosetta observations. *Space Sci. Rev*. **216**, 44 (2020).
20. Deshapriya, J. D. P. Exposed bright features on the comet 67P/Churyumov–Gerasimenko: distribution and evolution. *Astron. Astrophys*. **613**, A36 (2018).
21. Filacchione, G. et al. Exposed water ice on the nucleus of comet 67P/Churyumov-Gerasimenko. *Nature* **529**, 368–372 (2016).
22. Sunshine, J. M. et al. Exposed water ice deposits on the surface of comet 9P/Tempel 1. *Science* **311**, 1453–1455 (2006).
23. Groussin, O. et al. Gravitational slopes, geomorphology, and material strengths of the nucleus of comet 67P/Churyumov-Gerasimenko from OSIRIS observations. *Astron. Astrophys*. **583**, A32 (2015).
24. Herique, A. et al. Homogeneity of 67P/Churyumov-Gerasimenko as seen by CONSERT: implication on composition and formation. *Astron. Astrophys*. **630**, A6 (2019).
25. Pätzold, M. et al. A homogeneous nucleus for comet 67P/Churyumov–Gerasimenko from its gravity field. *Nature* **530**, 63–65 (2016).
26. Fulle, M. et al. Comet 67P/Churyumov–Gerasimenko preserved the pebbles that formed planetesimals. *Mon. Not. R. Astron. Soc*. **462**, S132–S137 (2016).
27. Blum, J. et al. The physics of protoplanetesimal dust agglomerates. I. Mechanical properties and relations to primitive bodies in the Solar System. *Astrophys. J*. **652**, 1768–1781 (2006).
28. Mannel, T. et al. Dust of comet 67P/Churyumov-Gerasimenko collected by Rosetta/MIDAS: classification and extension to the nanometre scale. *Astron. Astrophys*. **630**, A26 (2019).
29. Güttler, C. et al. Synthesis of the morphological description of cometary dust at comet 67P/Churyumov-Gerasimenko. *Astron. Astrophys*. **630**, A24 (2019).
30. Lorek, S., Gundlach, B., Lacerda, P. & Blum, J. Comet formation in collapsing pebble clouds — what cometary bulk density implies for the cloud mass and dust-to-ice ratio. *Astron. Astrophys*. **587**, A128 (2016).
31. Fulle, M. et al. How comets work: nucleus erosion versus dehydration. *Mon. Not. R. Astron. Soc*. **493**, 4039–4044 (2020).
32. Gundlach, B., Fulle, M. & Blum, J. On the activity of comets: understanding the gas and dust emission from comet 67P/Churyumov-Gerasimenko's south-pole region during perihelion. *Mon. Not. R. Astron. Soc*. **493**, 3690–3715 (2020).
33. Bockelée-Morvan, D. et al. *AMBITION–Comet Nucleus Cryogenic Sample Return*. https://www.cosmos.esa.int/web/voyage-2050/white-papers (ESA, 2019).
34. Veverka, J. *Cryogenic Comet Nucleus Sample Return (CNSR) Mission Technology Study*. Report SDO-12367 https://solarsystem.nasa.gov/studies/228/cryogenic-comet-nucleus-sample-return-cnsr-mission-technology-study (NASA, 2017).

Methods

OSIRIS data analysis

The normal albedo presented here has been evaluated from photometrically corrected images using the shape 7S model with 12 million facets[35] and the Hapke model[36] parameters (table 4 of ref. [37]) from resolved photometry in the orange filter centred at 649 nm.

We assume that the phase function at 649 nm also applies at the other wavelengths[17]. The flux of a region of interest (ROI) in each of the 3 filters has been integrated over 3-pixel-wide, square boxes. We attempt to reproduce the spectral behaviour and the normal albedo of the ice-rich patches by obtaining synthetic spectra of areal mixtures (spatially segregated) of the comet's dark terrain (DT), derived from areas near the boulder with water ice:

$$R = \rho R_{\mathrm{ice}} + (1-\rho)R_{\mathrm{DT}} \quad (1)$$

where R is the reflectance of the bright patches, R_{ice} and R_{DT} are the reflectance of the water ice and of the comet's dark terrain, respectively, and ρ is the relative surface fraction of water ice or frost.

We use areal mixture models due to the absence of reliable and relevant optical constants for the dark material needed to run more complex scattering models, and the absence of clear absorption features in the wavelength range covered by the OSIRIS observations. The water-ice spectrum was derived from Hapke modelling of optical constants[38] using grain sizes of 30 μm and 100 μm. In fact, the typical size of ice grains on cometary nuclei was found to be a few tens of micrometres[22,39,40].

We also attempt to use models with larger water-ice grains (up to 1,000 μm and 2,000 μm), but these models gave a worse spectral match and a lower χ^2 fit. The models that best fit the maximum absolute reflectance observed on the bright patch on the skull boulder are areal mixtures of the average cometary dark terrain (DT) enriched with 46.4%–47.4% of water ice (Fig. 3d, Extended Data Table 1) with grain sizes of 30–100 μm. A further analysis is provided in Supplementary Methods.

VIRTIS data analysis

The best viewing opportunity for VIRTIS-M[41] of the Philae touchdown 2 (TD2) site occurred on 14 June 2016 between 10:51:12 and 11:35:31 UTC when the Rosetta spacecraft was at a distance of 27.3 km from 67P and the solar phase angle was 57°.

During this period of time, the VIRTIS-M instrument acquired a visible hyperspectral cube (acquisition V1_00424522185.QUB) by collecting 133 consecutive slit images of the surface with a spatial resolution of about 6.5 × 10 m (along slit × scan). Each slit image was acquired with an integration time of 16 s and a repetition step time of 20 s while the Rosetta spacecraft was maintaining nadir pointing. At each step the internal scan mirror is rotated by an angle of 250 μrad (corresponding to one Instantaneous Field-Of-View—IFOV) to achieve an angular scan of about 1.9° in 133 steps. Consecutive slits are not completely connected among them, being separated by about 13 m.

The resulting hyperspectral image of the Abydos region shown in Fig. 3b has a scale of 1.66 km (slit width) by 0.86 km (scan length). The position of the cracked boulder on the TD2 site has been identified close to pixels at line = 1, samples = 163–168 and appears located at the edge of the FOV (see Fig. 3b, panel b2, blue box). According to reconstructed geometries computed on the SHAP7 digital model and including the current best estimate of the errors, the centres of these pixels are offset by a minimum of 25 m to a maximum of 58 m with respect to the reference position of TD2. The identification of the TD2 location on the VIRTIS image is therefore not fully certain owing to the limited spatial resolution and position of the pixels on the edge of the VIRTIS image.

Owing to the coarse spatial resolution, VIRTIS-M is not able to resolve the cracked boulder whose exposed bright area is about 0.5 m^2 while the pixel area is 65 m^2. Moreover, owing to the instrumental point spread function[42,43] FWHM (<500 μrad) and to the uncertainty on the position of the TD2 site, we are averaging the signal of the candidate TD2 area taken on 6 contiguous pixels where higher reflectance and blueing is observed.

The average reflectance spectrum of the TD2 pixels is shown in Extended Data Fig. 4a and compared with an average collected on nearby pixels (line = 2, samples = 163–168) as a reference for an adjacent non-icy terrain (Extended Data Fig. 4b). The analysis of the spectral slope measured on the two ROI gives a value of 2.39 μm^{-1} and 2.59 μm^{-1} for the cracked boulder pixels (blue curve) and nearby dark terrain (red curve), respectively. These values correspond to a spectral slope difference of $\Delta = 0.20\ \mu m^{-1}$. This difference is equivalent[44] to a water-ice abundance of 0.1% in areal mixing (Extended Data Fig. 4c).

The size of the bright area on TD2 has been constrained to about 3.5 m^2 on OSIRIS high-resolution images, of which about 1 m^2 is made of exposed water ice in an areal mixture (where water ice and dust do not thermally interact leading to less energy being available for sublimation). Our analysis shows that VIRTIS is missing the TD2 location by about one line and that the signal is harvesting the tail of the optical point spread function. As a consequence of this, we are collecting about 20% of the photons coming from the water-ice patch on the TD2 site. This means that the water-ice abundance of 0.1% ± 0.04% previously estimated is likely to be five times larger, leading to 0.5% ± 0.2%. Scaling this value for the total area of 253 m^2 on 6 pixels, the water-ice-rich spot corresponds to an area of about 1.27 ± 0.5 m^2, in agreement with OSIRIS findings.

ROMAP and RPC-MAG data analysis

The tri-axial lander magnetometer ROMAP and orbiter magnetometer RPC-MAG were operating during the descent, landing and rebound phase with a sampling rate of 1 Hz. Extended Data Fig. 5 shows the measurements of both instruments for the interval around TD2. In order to use magnetic field measurements for flight dynamics reconstructions, reference measurements are necessary to separate external events in the background magnetic field (for example, magnetic wave activity as seen in the RPC-MAG observations in Extended Data Fig. 5) from changes caused by the spacecraft dynamics or operation (for example, rotation change or boom movements). In this case, the RPC-MAG orbiter instrument was used as background field reference to be able to reconstruct the Philae dynamics.

A rotation of the lander along an arbitrary axis relative to the background magnetic field causes an apparent rotation of the magnetic field vector observed by the lander relative to the orbiter reference. This causes the three-dimensional (3D) quasi-sinusoidal modulation of the ROMAP measurements relative to the RPC-MAG measurements visible in Extended Data Fig. 5. A time-dependent rotation matrix between these two 3D observations can therefore be calculated to describe the attitude of the lander relative to the orbiter. This information can then in theory be used to derive a set of time-dependent quaternions giving the absolute attitude of the lander.

A statistical analysis has to be used to accurately determine the absolute attitude to account for small deviations between the orbiter and lander measurements caused by noise and plasma phenomena (for a detailed description, see ref. [12]). In this case only a minimal number of data points is available due to the low 1 Hz sampling rate and relatively fast changes in lander dynamics. Hence, a simplified analysis for the reconstruction of the rotation rate during descent was used[12] to estimate the average lander rotation rate between the individual surface contacts (see Extended Data Table 2). Instead of determining the total absolute lander orientation, this method is based on determining only the orientation of the lander rotation axis, which allows the lander magnetic field observations to be transformed into a temporary coordinate system in which one magnetic axis remains stable (that is, the field along the rotation axis) and only the two remaining axes show a

modulation. This modulation relative to the orbiter reference measurements can easily be determined, and results directly in the lander rotation frequency[12].

A rotation of the magnetometer boom relative to the lander creates a characteristic signature (as can be seen around 17:25:30 UT in Fig. 2a and Extended Data Fig. 5) in the magnetic field caused by the displacement of the ROMAP sensor relative to the static lander bias field[13]. The shape and duration of this signature allows us to constrain the acceleration acting on the lander perpendicular to the boom rotation axis, that is, along the lander z axis. The other touchdowns[1,11] were used as references to determine the direction and timing, and gain a qualitative insight into the magnitude (see Supplementary Information for more details)

Philae lander dynamics at the TD2c point

This section covers only the dynamics at the TD2c point, where the ice was compressed by the Philae balcony and SD2 tower. The full dynamics that took place through all four TD2 points (TD2a–d) are described in the Supplementary Methods and summarized in Extended Data Table 2.

The TD2c contact duration is linked to the ROMAP boom, which showed an upwards movement at 17:25:24 ± 1 s continuing until approximately 17:25:27 ± 1 s (Fig. 2a, Extended Data Fig. 5). At 17:25:27 ± 1 s, the boom started to move downwards away from the lid, meaning that the acceleration of the lander had stopped or reversed. The change at 17:25:27 ± 1 s is considered the end position of the stamping in TD2c, because the geometry from the deceleration of Philae during stamping causes an upward deflection of the boom, which is what was observed. This resulted in a duration of 3 ± 1 s for the stamping/compression of the ice (see Fig. 2a–c and the animation in Supplementary Video 3). The energy loss at TD2c caused by the stamping is estimated to be 0.671 ± 0.297 J.

Estimating TD2c surface area and depth

The images used in the data analysis are obtained from numerous epochs and distances from the comet. The pixel resolution linked to distance ranged from 0.16 m per pixel in May 2016 when the spacecraft was 8.5 km from the crevice, to 0.13 m per pixel at a distance of 7 km in June 2016, to 0.049 m per pixel at the closest distance reached on 2 September 2016 (2.63 km). The pixel size in Extended Data Fig. 1 for both pre- and post-landing images was 0.15 m per pixel, as the images were taken at an equivalent distance (8 km) to the crevice.

Image analysis relied primarily on cross-correlating multiple images to determine accurate estimates of heights and width of different boulder features. The lower the resolution the greater the error bar, as it became difficult to determine where the edge of a feature actually started or ended owing to the greater coverage of the pixel. The error bar is therefore linked to the pixel resolution achievable in the image analysis.

A lower limit of 0.2208 m^2 has been estimated for the area of ice compressed by Philae in the TD2c position. Only two OSIRIS images (21 August 19:19 UT, 24 August 2016 19:39 UT; Figs. 1f, 2c) provide a clear, albeit angled, view of the ice in the compression. The full width of the ice impression could therefore not be estimated due to lack of direct visibility. It was feasible however to use both these images as well as another from 2 September 2016 19:59 in Fig. 3e (which provides an edge-on-view of the ice impression) to obtain a lower-limit measurement of the length of the sides of the Philae balcony that made the impression. The estimate is a combination therefore of the actual area of the Philae balcony matching these lengths plus the area of an arc matching the remainder of the angled visible ice.

Figures 1d, 2b and 3e (same images) were taken on 2 September 2016 at the closest distance (2.63 km) to the nucleus surface achieved by Rosetta during the mission, and provide therefore the highest resolution. This image, which was the famous Philae discovery image, provides a clear high-resolution view of the edge of the compressed ice region in TD2c. The solar illumination in this image is equivalent to the illumination observed on 6 August 05:52 UT, and allows to conclude that while the sunlight was gradually moving down the crevice, it had not yet arrived at the compressed region. As a result, the stamped edge lies in shadow, with the exposed ice further back in the crevice creating a back-light effect. This edge-on view allows an accurate measurement of 0.246 ± 0.049 m to be taken of the depth of the compressed region. In that respect, the one image showing Philae resting on the surface of the comet (Fig. 1d) also provides the key input measurement for this paper. Further dimension-related images are provided (Supplementary Figs. 7, 8).

Compressive strength and porosity analysis

The model that we use. To derive material properties for the cometary boulder from our findings, we consider a hierarchical setup of the interior structure of the boulder assuming the dust and ice grains are concentrated in larger units ('pebbles'), which themselves are clustered together to make up the boulder[45]. Thus, the boulder itself is a kind of 'rubble pile' and possesses pore space on two length scales, the microscopic and the pebble-sized. Comparisons between our model and others addressing the basic building blocks of the internal material of the comet can be found elsewhere[24,32,46,47] and are not dealt with further in this paper.

Compressive strength estimates. As the incoming trajectory of Philae at TD2c with respect to the surface normal shows, Philae lost a total kinetic energy of $\Delta E = 0.671 \pm 0.297$ J owing to compression ('stamping') of the surface material of comet 67P. The vertical component of the incoming motion of Philae resulted in the compaction of the porous cometary matter. The characteristic stress required for stamping is determined by the compressive strength P_C of the material. With the depth and minimum area of the stamping impression Philae made estimated (see main text) to be $h = 0.246 \pm 0.049$ m and $A_{Min} = 0.2208$ m^2, respectively, a minimum volume of $V_{Min} = A_{Min}h = 0.054$ m^3 was displaced during stamping.

We can make a first, crude, estimate of the compressive strength by assuming that the compressed volume is at least V_{Min} and that the compressive strength is a constant material value, that is, is independent of the compressional state of the matter. In reality, a much larger volume than V_{Min} is affected by the impact of Philae and P_C is a strong function of the porosity (see below). However, we can state that $P_C < \frac{\Delta E}{V_{Min}} = 12$ Pa is required to account for the observed material compression and energy loss of Philae. It should be noted that this upper limit for the compressive strength of 67P's surface material is model independent and based on firm measurements (this paper).

Compressive strength link to volume filling factor. The compressive strength is not a constant material value, but rather depends on the volume filling factor (fraction of total volume filled by material), Φ, in a characteristic way[27,48,49]

$$P_C(\Phi) = p_m \left(\frac{\Phi - \Phi_1}{\Phi_2 - \Phi} \right)^{\Delta'} \quad (2)$$

with Φ_1 and Φ_2 being the formal lower and upper limits of the volume filling factor for which $P_C(\Phi_1) = 0$ and $P_C(\Phi_2) \to \infty$, respectively (see below for p_m and Δ').

Experiments and numerical simulations showed[27,48–50] that Φ_2 is in the range 0.1–0.9, depending on the particle properties, such as grain size, grain-size distribution, grain shape, and the mode of deposition or compression. The value of Φ_1, which has no physical meaning and is merely a fitting parameter, ranges[45] between 0.05 and 0.35. The factor p_m is the characteristic compressive strength and Δ' describes the logarithmic range of stresses in which compression takes place: that is, most compression happens in the interval $(10^{-\Delta'} p_m, 10^{+\Delta'} p_m)$.

Schräpler et al.[49] showed that this relation holds for a wide range of particle sizes, from loose granular ensembles of dust aggregates (the 'pebbles' in our notation) to others of a more homogeneous

assemblage. They also showed that $\Delta' = 1.3$ is an appropriate value for all kinds of grain and pebble sizes. Pebble assemblages possess characteristic compressive strengths of $p_m \approx 6.1 \times 10^{-2}$ Pa for pebbles with 1 mm radius and $p_m \approx 4.7 \times 10^{-3}$ Pa for pebbles with 1 cm radius (for the heterogeneous case—as is our model), whereas submicrometre-sized particles in a more homogenous structure are compressed with $p_m \approx 10^4$ Pa. The schematic functional dependence of the volume filling factor on compression for our model is shown in Extended Data Fig. 6c.

Volume filling factor applied to the cometary boulder interior (TD2c). To estimate the volume filling factor, and therefore the porosity, we need to take into account the manner in which the pebble assemblage compacts when the boulder interior is formed. The different ways in which this can happen can vary, as touched on briefly in the Supplementary Information, whether it occurs at initial cometary formation or long afterwards as the result of cometary dynamical events. The resulting packing fraction of the pebble assemblage can be defined in these scenarios by random loose packing (RLP), which means[51] $\Phi_{RLP} \approx 0.55$, if inter-pebble friction is strong[52] (a criterion satisfied for dust/ice aggregates) and if the size–frequency distribution of the pebbles is narrow (see Supplementary Methods).

The maximum random packing density is random close packing (RCP), or[51,52] $\Phi_{RCP} \approx 0.64$ for narrow size distributions. Thus, Philae's energy was dissipated by the compaction from RLP towards RCP (see Extended Data Fig. 6c). The total compressed volume must be larger than the displaced volume, V_{Min}, to make room for the displaced material (Extended Data Fig. 6a, b). Assuming that the overall compressed volume is $V_{Eff} = \eta V_{Min}$ and that the increase in volume filling factor from initially $\Phi_{Min} = \Phi_{RLP}$ to Φ_{Max} is identical everywhere inside this volume, the volume scaling factor can be derived as $\eta = \frac{\Phi_{Min}}{\delta\Phi}$, with $\delta\Phi = \Phi_{Max} - \Phi_{Min}$. We can calculate the energy dissipated by Philae's stamping motion (in the z direction), $\Delta E = 0.671$ J to be:

$$\begin{aligned}\Delta E &= \int_{V_{Eff}+V_{Min}}^{V_{Eff}} P_C \mathrm{d}V \\ &= A\int_0^h P_C \mathrm{d}z \\ &= Ap_m\int_0^h \left(\frac{\Phi(z)-\Phi_1}{\Phi_{RCP}-\Phi(z)}\right)^{\Delta'} \mathrm{d}z \\ &= Ap_m\int_{\Phi_{Min}}^{\Phi_{Max}} \left(\frac{\Phi-\Phi_1}{\Phi_{RCP}-\Phi}\right)^{\Delta'} \frac{\mathrm{d}z}{\mathrm{d}\Phi}\mathrm{d}\Phi \\ &= \frac{V_{Min}p_m}{\delta\Phi}\int_{\Phi_{Min}}^{\Phi_{Max}} \left(\frac{\Phi-\Phi_1}{\Phi_{RCP}-\Phi}\right)^{\Delta'} \mathrm{d}\Phi,\end{aligned} \quad (3)$$

in which we use equation (2) with $\Phi_2 = \Phi_{RCP}$ and the approximation $\Phi(z) = \Phi_{Min} + \frac{z}{h}\delta\Phi$ and $\frac{\mathrm{d}z}{\mathrm{d}\Phi} = \frac{h}{\delta\Phi}$, with $h = 0.246$ m and $A = 0.2208$ m^2 being Philae's intrusion and stamping cross-section.

Applying equation (3) (see Supplementary Table 1) with the nominal values $p_m \approx 10^{-2}$ Pa, $\Phi_{Min} = \Phi_{RLP} = 0.55$, $\Delta' = 1.3$ and $\Phi_1 = 0.05$ shows that $\Phi_{Max} \approx \Phi_{RCP}$ and, thus, $\eta = 6.1$ and $V_{Eff} = 0.33$ m^3.

It should be noted that the volume filling factor assumed in the above calculation, $\Phi = \Phi_{RLP} \approx 0.55$, is that of the pebble assemblage. The pebbles themselves consist of submicrometre-sized dust/ice particles so that they possess internal porosity, which can be expressed by their inner volume filling factor $\Phi_{pebble} \approx 0.33$–$0.58$, depending on the type of compression experienced by the pebbles, as shown in laboratory experiments[48].

Taking the average of this range in volume filling factor of the pebbles, $\Phi_{pebble} = 0.455 \pm 0.125$, we get an overall volume filling factor of the boulder of $\Phi_{boulder} = \Phi_{RLP}\Phi_{pebble} = 0.25 \pm 0.07$, comparable with the values determined by Rosetta[24–26]. It should be noted that our two-step hierarchical model for the inner constitution of the boulder is plausible, but by no means the only feasible solution (see Supplementary Methods for more details).

Data availability

All OSIRIS, VIRTIS, RPC-MAG and ROMAP calibrated data are publicly available through the European Space Agency's Planetary Science Archive website (https://archives.esac.esa.int/psa/). The Supplementary Information contains additional supporting images, data and explanatory text with the aim of allowing readers to understand what we have done and how we have done it.

35. Jorda, L. et al. The global shape, density and rotation of 67P/Churyumov-Gerasimenko from pre-perihelion Rosetta/OSIRIS observations. *Icarus* **277**, 257–278 (2016).
36. Hapke, B. et al. Bidirectional reflectance spectroscopy. 5. The coherent backscatter opposition effect and anisotropic scattering. *Icarus* **157**, 523–534 (2002).
37. Fornasier, S. et al. Spectrophotometric properties of the nucleus of comet 67P/Churyumov-Gerasimenko from the OSIRIS instrument onboard the ROSETTA spacecraft. *Astron. Astrophys.* **583**, A30 (2015).
38. Warren, S. G. & Brandt, R. E. Optical constants of ice from the ultraviolet to the microwave: a revised compilation. *J. Geophys. Res.* **113**, D14220 (2008).
39. Capaccioni, F. et al. The organic-rich surface of comet 67P/Churyumov-Gerasimenko as seen by VIRTIS/Rosetta. *Science* **347**, aaa0628 (2015).
40. Filacchione, G. et al. The global surface composition of 67P/CG nucleus by Rosetta/VIRTIS. (1) Prelanding mission phase. *Icarus* **274**, 334–349 (2016).
41. Coradini, A. et al. VIRTIS: an imaging spectrometer for the Rosetta mission. *Space Sci. Rev.* **128**, 529–559 (2007).
42. Filacchione, G. On-ground characterization of Rosetta/VIRTIS-M. II. Spatial and radiometric calibrations. *Rev. Sci. Instrum.* **77**, 103106 (2006).
43. Ammannito, E. et al. On-ground characterization of Rosetta/VIRTIS-M. I. Spectral and geometrical calibrations. *Rev. Sci. Instrum.* **77**, 093109 (2006).
44. Raponi, A. et al. The temporal evolution of exposed water ice-rich areas on the surface of 67P/Churyumov-Gerasimenko: spectral analysis. *Mon. Not. R. Astron. Soc.* **462** (Issue Suppl. 1), S476–S490 (2016).
45. Blum, J. et al. Evidence for the formation of comet 67P/Churyumov-Gerasimenko through gravitational collapse of a bound clump of pebbles. *Mon. Not. R. Astron. Soc.* **469**, S755–S773 (2017).
46. Skorov, Y. V. & Blum, J. Dust release and tensile strength of the non-volatile layer of cometary nuclei. *Icarus* **221**, 1–11 (2012).
47. Davidsson, B. J. R. et al. The primordial nucleus of comet 67P/Churyumov-Gerasimenko. *Astron. Astrophys.* **592**, A63 (2016).
48. Güttler, C. et al. The physics of protoplanetesimal dust agglomerates. IV. Toward a dynamical collision model. *Astrophys. J.* **701**, 130–141 (2009).
49. Schräpler, R. et al. The stratification of regolith on celestial objects. *Icarus* **257**, 33–46 (2015).
50. Oquendo-Patiño, W. F. & Estrada-Mejia, N. Optimal packing of poly-disperse spheres in 3D: effect of the grain size span and shape. In *Proc. VI International Conference on Particle-based Methods—Fundamentals and Applications* (eds Oñate, E. et al.) 313–319 (CIMNE, 2019).
51. Onoda, G. Y. & Liniger, E. G. Random loose packings of uniform spheres and the dilatancy onset. *Phys. Rev. Lett.* **64**, 2727–2730 (1990).
52. Luding, S. Granular matter: so much for the jamming point. *Nat. Phys.* **12**, 531–532 (2016).

Acknowledgements B.G. and J.B. thank Deutsches Zentrum für Luft- und Raumfahrt (DLR) for continuous support and Deutsche Forschungsgemeinschaft for their support under grant Bl 298/24-2 in the framework of the Research Unit FOR 2285 'Debris disks in planetary systems'. OSIRIS was built by a consortium led by Max-Planck-Institut für Sonnensystemforschung, Göttingen, Germany, in collaboration with CISAS, University of Padova, Italy, Laboratoire d'Astrophysique de Marseille, France, Instituto de Astrofisica de Andalucia, CSIC, Granada, Spain, the Scientific Support Office of the European Space Agency, Noordwijk, The Netherlands, Instituto Nacional de Tecnica Aeroespacial, Madrid, Spain, Universidad Politechnica de Madrid, Spain, the Department of Physics and Astronomy of Uppsala University, Sweden, and Institut für Datentechnik und Kommunikationsnetze der Technischen Universität Braunschweig, Germany. The support of the national funding agencies of Germany (DLR), France (CNES), Italy (ASI), Spain (MEC), Sweden (SNSB), and the ESA Technical Directorate is gratefully acknowledged. Those authors who are part of the VIRTIS and GIADA teams wish to thank the Italian Space Agency (ASI, Italy; contract number I/024/12/2) and Centre National d'Études Spatiales (CNES, France) for supporting their contribution. The contribution of the ROMAP and RPC-MAG teams was financially supported by the German Ministerium für Wirtschaft und Energie and the Deutsches Zentrum für Luft- und Raumfahrt under contract 50QP1401. This research has made use of the scientific software shapeViewer (www.comet-toolbox.com). Video rendering was powered by PRo3D, a viewer for the exploration and analysis of planetary and smaller body surface reconstructions. It was developed by VRVis Zentrum für Virtual Reality und Visualisierung Forschungs-GmbH in close collaboration with Joanneum Research and Imperial College London; see http://pro3d.space for more details. Trajectory and instrumental information relevant to the observations performed on Rosetta was based on the use of SPICE kernels. We acknowledge the important role played by the Rosetta Science Ground Segment, the Rosetta Mission Operations Team and the Philae Lander team(s) in the running of the Rosetta mission and Philae Lander Operations.

Author contributions Identification of the skull-top crevice ice and other touchdown points was made by L.O'R. The lead writer of the paper is L.O'R. Contributions to Methods and sections of Supplementary Information were made by L.O'R., P.H., S.F.,

H.V.H., G.F., A.R., M.C., J.B., B. Gundlach, A.R., M.d.P.C.P. and G.P. The ROMAP and RPC-MAG data analysis was performed by P.H., K.-H.G. and H.-U.A. in close collaboration with L.O'R. The compressive strength and porosity analysis was performed by J.B. and B.G. The OSIRIS image analysis was performed by L.O'R., S.F. and H.V.H. The VIRTIS data analysis was carried out by G.F., A.R., M.C. and F.C. The skull-top crevice ice and dust analysis was carried out by A.R., D.B.-M., M.K., O.G. and N.O. The OSIRIS image processing was performed by S.F., H.V.H., G.K., C.T. and H.S. Trajectory data analysis was performed by B. Grieger, L.O'R., R.A.B., P.H., J.-B.V., C.T. and H.S. Shape model support and analysis were provided by L.J., J.-B.V., R.A.B., M.d.P.C.P. and G.P. Figures (in support of analysis) were generated by L.O'R., P.H., R.A.B., J.B., B. Gundlach, S.F., H.V.H., G.F., A.R. and M.C. All authors have participated in the review of the paper and its contents.

Competing interests The authors declare no competing financial interests. One of the authors, N.O., is currently an editor at *Nature Communications*, but was not in any way involved in the journal review process.

Additional information

Supplementary information is available for this paper at https://doi.org/10.1038/s41586-020-2834-3.

Correspondence and requests for materials should be addressed to L.O.

Peer review information *Nature* thanks Erik Asphaug, Dennis Bodewits, Mathieu Choukroun and the other, anonymous, reviewer(s) for their contribution to the peer review of this work. Peer reviewer reports are available.

Reprints and permissions information is available at http://www.nature.com/reprints.

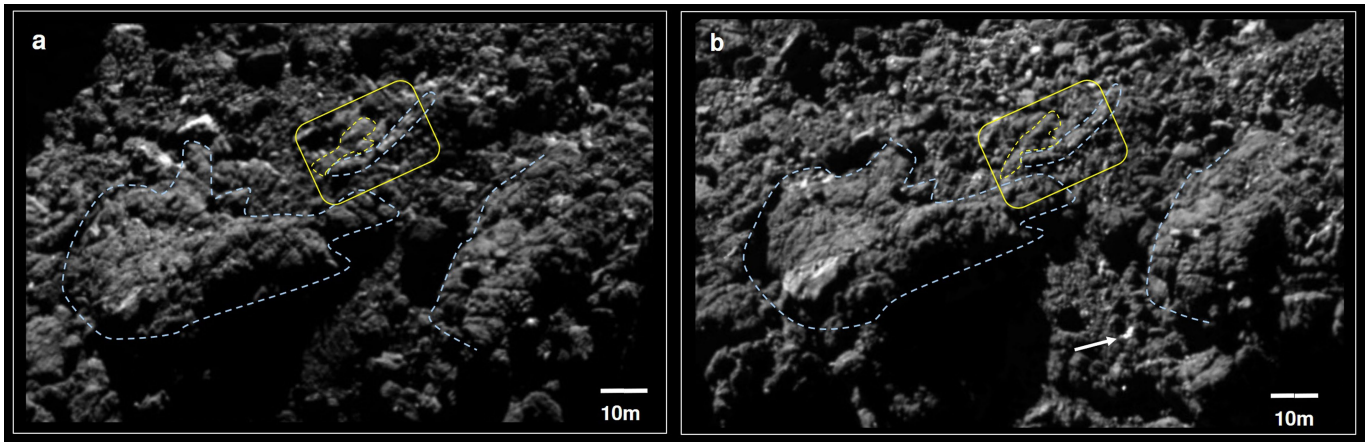

Extended Data Fig. 1 | Comparison of pre-landing and post-landing images. **a**, **b**, Comparison of the location of the skull-top ridge (yellow rectangle) as it looked in a pre-landing OSIRIS image (**a**; 22 October 2014) and in a post-landing image (**b**; 14 May 2016). The yellow dashed lines outline the skull-top boulders (see Supplementary Video 1 for a detailed comparison), while context terrain similarities between images are shown in blue dashed lines. Although the spacecraft distance is the same (about 8 km), the solar illumination and the Rosetta viewing geometry differ between the images. An arrow points at the Philae lander location in **b**.

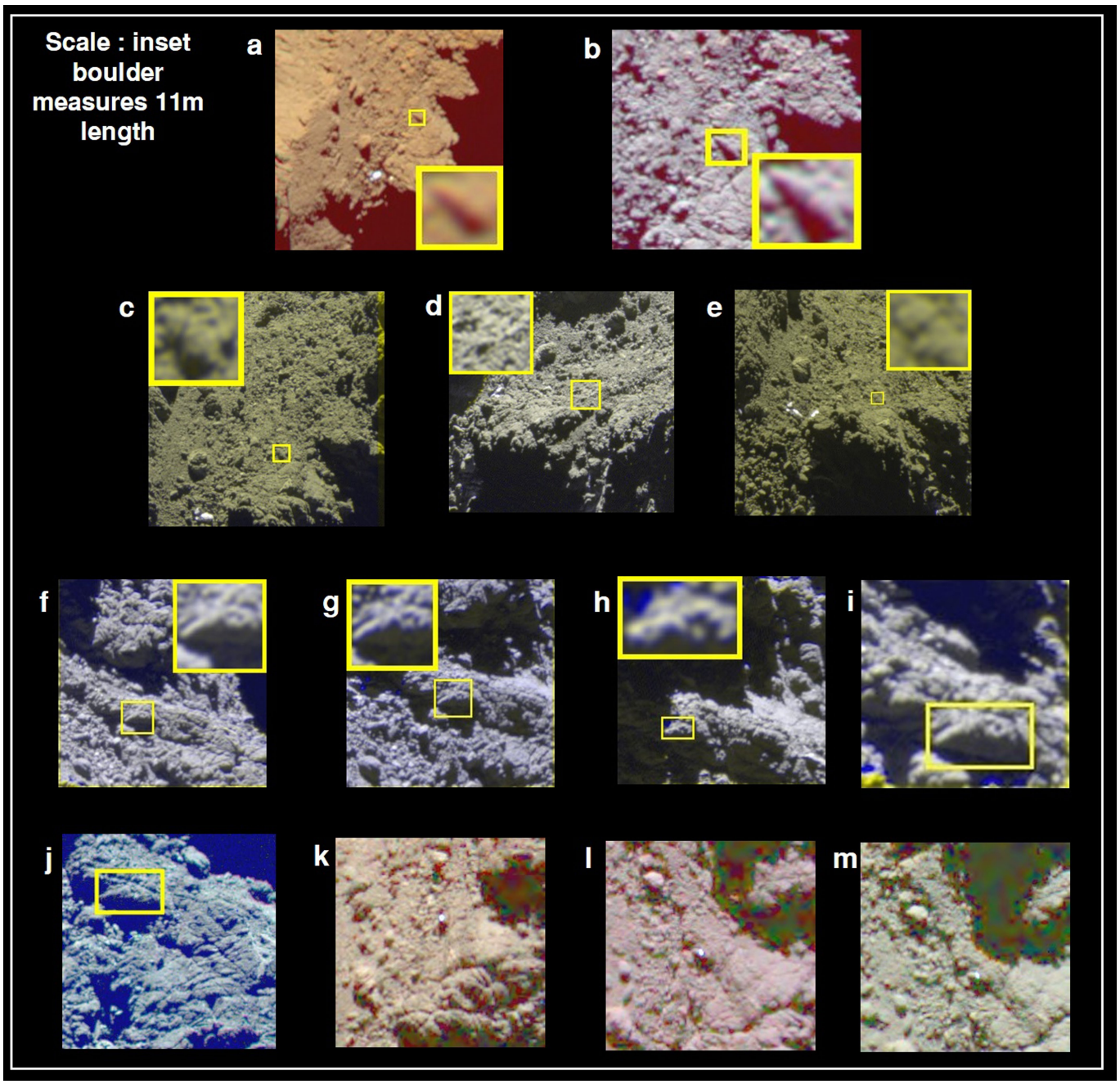

Extended Data Fig. 2 | OSIRIS colour composites of skull-top boulders. (In **a**–**h**, the boxed feature in the main image is shown magnified in the inset. In **i**, **j**, no magnification is required.) **a**, **b**, Pre-landing images of skull-top boulders. RGB setting; 'green' = F24 (480.7 nm), 'red' = F22 (649.2 nm), 'blue' = F16 (360.0 nm). **c**–**e**, Skull-top boulders observed in December 2014. RGB setting; 'green' = 'red' = F22 (649.2 nm), 'blue' = F24 (480.7 nm). **f**–**i**, The skull-top boulders observed in March 2016. RGB setting; 'green' = 'red' = F22 (649.2 nm), 'blue' = F24 (480.7 nm). **j**–**m**, Colour composite of the skull-top boulders in early and mid-June 2016 with the brightly lit ice feature visible in **k**–**m** specifically. RGB setting; 'green' = F24 (480.7 nm), 'red' = F22 (649.2 nm), 'blue' = F16 (360.0 nm).

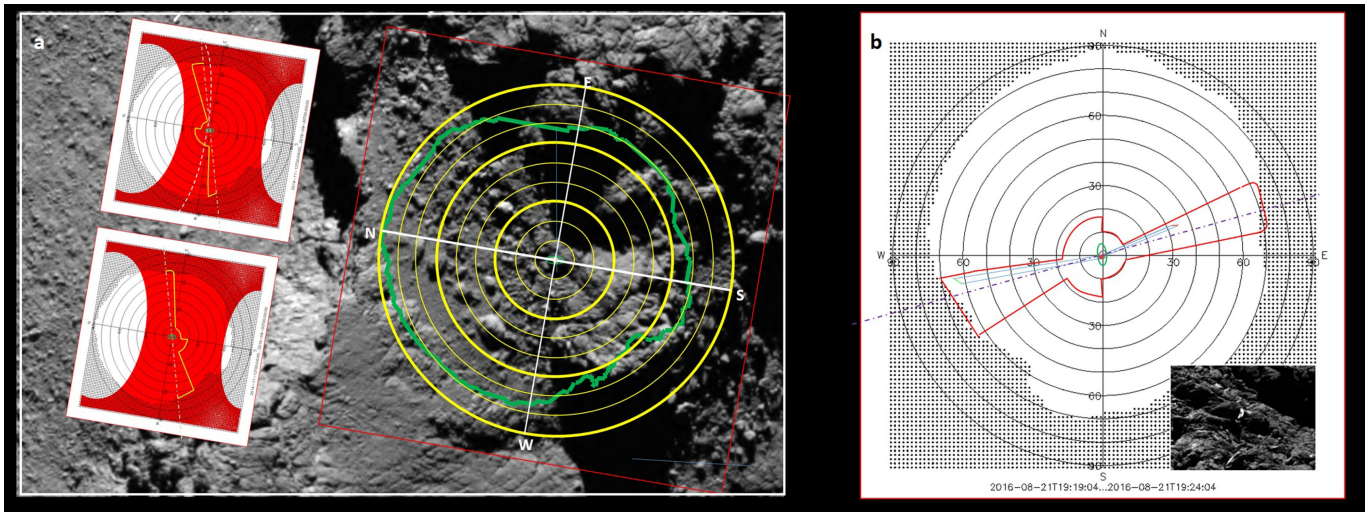

Extended Data Fig. 3 | Illumination geometry of the skull-top crevice. **a**, OSIRIS NAC image of the Abydos region on 12 June 2016 with three overlaid azimuth plots. The central point of each plot is positioned on the skull-top crevice. The two skull-top boulders are outlined by the green ellipse and the crevice by a tiny purple ellipse inside it. At this central point the viewer is at a 90° angle, that is, an overhead view; each concentric circle represents a decrease in viewing angle of 10°. The large red box encloses an azimuth plot overlaid on the image and the green line shows the horizon. The red area in the two left-hand azimuth plots shows the track of the Sun over this region during the full period of the Philae landing and to the end of the Rosetta mission, while the yellow line overlay is the crevice's own horizon mask (created as explained in **b**). **b**, Example azimuth plot for 21 August 19:19–19:24 UT with Rosetta's position and the Sun's position at this time marked by the very short green and red lines. These short lines are then connected by long blue lines to the central crevice. This gives the line of sight for the OSIRIS camera and for solar illumination of the crevice during this period. We then look at the OSIRIS image (inset) to see if the crevice is illuminated. We find that it is, which is why it lies inside the red-lined horizon mask. The dot-dashed line passes right through the crevice, meaning that the right of that line is the right side of the crevice and the left, the left side.

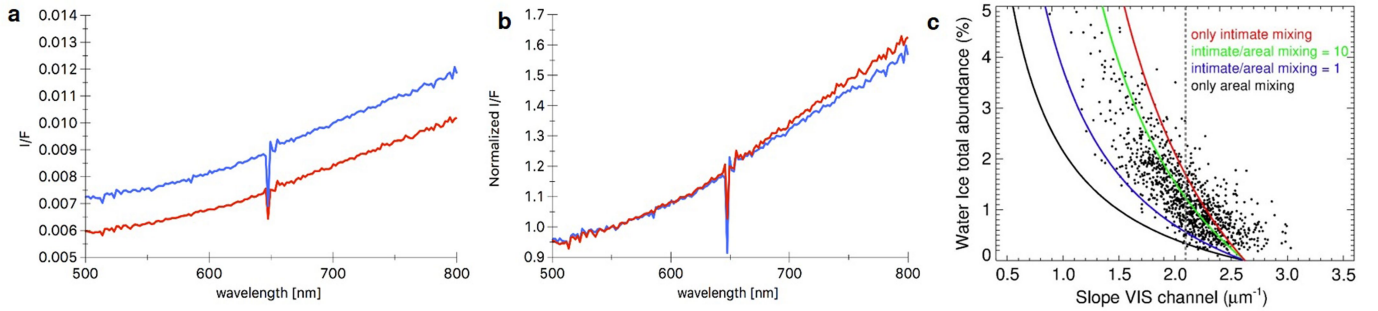

Extended Data Fig. 4 | VIRTIS water-ice analysis plots. a, **b**, Average radiance factor of the skull-top boulder location (blue curve) and of the nearby dark terrain (red curve) before (**a**) and after (**b**) normalization at 550 nm. **c**, Theoretical abundance of water ice as a function of the spectral slope in the visible (VIS) spectral channel[44]. Black dots and dashed lines indicate a water-ice-rich region observed by VIRTIS to calibrate the theoretical curves. The black line represents a solely areal mixing case and the red line a solely intimate mixing case. The blue and green lines represent a merge of both, with different mixing ratios of 1 and 10, respectively. The *x*-axis values correspond to slope values scaled to the dark terrain unit viewing conditions (Fig. 3b, panel b1, red box) for observation V1_00424522185.QUB.

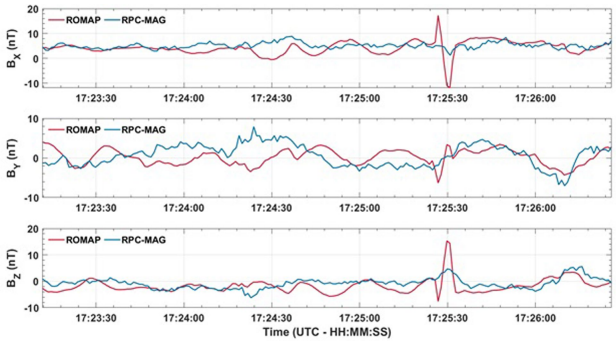

Extended Data Fig. 5 | Combined ROMAP and RPC-MAG magnetic-field and boom measurements. The three components of the magnetic field observations (B_x, B_y, B_z, respectively top, middle and bottom) are shown starting before TD2 at 17:23:00 UTC and ending shortly after the boom movement was detected. This figure also shows the concurrent orbiter RPC-MAG observations as a reference. See Methods and Supplementary Methods section 7 for a detailed description.

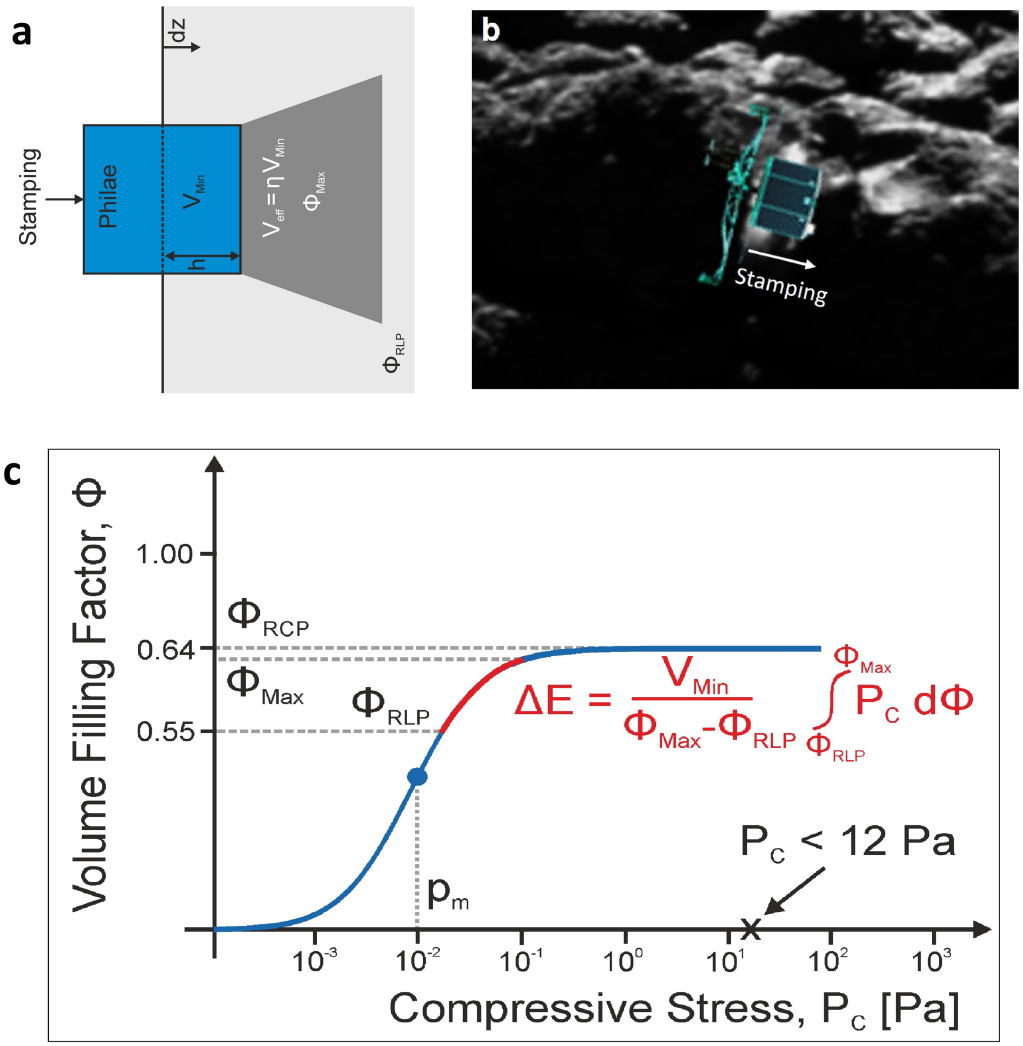

Extended Data Fig. 6 | Philae interaction geometry and boulder volume-filling factor. a, Interaction geometry of Philae with the ice/dust at the moment of deepest penetration in TD2c. **b**, Philae superimposed on an OSIRIS image (2 September 2016), showing an interaction geometry equivalent to that in **a**. **c**, Compressive stress curves for a boulder consisting of pebbles. Note that the volume-filling factor Φ denotes packing of porous pebbles only; these are then further packed to make up the whole boulder. See Methods for a detailed explanation of this panel.

Extended Data Table 1 | Estimation of TD2c water-ice content

Acquisition time	Δ (km)	α (°)	Area (m^2)	ρ (30 μm)	ρ (100 μm)
2016-06-12T22:29:58	27.5	81.4	3.7	$28.8^{+5.8}_{-5.3}$%	$30.3^{+6.1}_{-5.5}$%
2016-06-14T10:30:32	26.7	54.0	3.5	46.4%	47.4%
2016-06-14T22:23:41	26.3	48.6	2.5	40.7%	43.0%

This table shows the estimation of the water-ice content of the bright spot observed at the crevice of the skull boulder from three separate observations by the OSIRIS instrument in mid-June 2016. Columns (left to right) show acquisition time of data; Δ, the distance between the spacecraft and the comet surface; α, the phase angle; Area, the estimated area of the bright spot; and ρ, the water-ice fraction at both 30 μm and 100 μm. The 14 June 2016 10:30:32 image provides the highest value, as the illumination into the crevice and the viewing conditions were both the best at that time.

Extended Data Table 2 | Philae lander dynamics for TD2a–d

	TD2a (Initial Contact)	TD2b (Dust wall)	TD2c (Stamping)	TD2d (Dust compression)
Start Time (UT)	17:23:48±10s	17:24:53±1s	17:25:24 ±1s	17:25:30±1s
End Time (UT)	17:24:22±1s		17:25:27±1s	17:25:33±1s
Contact Time t (s)	30±10	2±1	3±1	2±1
Incoming Kinetic Energy (J)	2.97±0.15	1.845±0.18	1.028±0.197	0.357±0.1
Outgoing Kinetic Energy (J)	1.974±0.18	1.028±0.197	0.357±0.1	0.10±0.02
Energy Loss (J)	1.342±0.33	0.817±0.377	0.671±0.297	0.257±0.12
Incoming Rotation Rate (mHz)	42.0±1.0	64.0±1.0	28±1.0	33±1.0
Outgoing Rotation Rate (mHz)	64.0±1.0	28±1.0	33±5.0	2±0.5
Incoming Vertical Velocity (m/s)	≈ −0.194	-0.034±0.008	-0.017±0.006	≈ 0
Incoming Horizontal Velocity (m/s)	≈ 0.098	0.109±0.011	0.125±0.013	≈ 0
Outgoing Vertical Velocity (m/s)	-0.034±0.008	-0.017±0.006	>+0.073 (after stamping)	≈ + 0.007
Outgoing Horizontal Velocity (m/s)	0.109±0.011	0.125±0.013	≈ 0	≈ 0.090

Shown is a summary of the underlying values and results for TD2, including timing, as described in Methods (section 'Philae lander dynamics at the TD2c point') and Supplementary Methods (section 'ROMAP/RPC-MAG detailed analysis describing Philae's flight through TD2'). Supplementary Video 4 provides an animation showing the dust wall referred to in the table.

Chapter 3

Low water outgassing from (24) Themis and (65) Cybele: 3.1μm Near-IR Spectral Implications

This chapter is linked to the second of the objectives of the thesis whereby we search for and characterise ice found on the surface and subsurface of asteroids. The article covered in this chapter "Low Water outgassing from (24) Themis and (65) Cybele – 3.1 μm NIR spectra implications", was published in Astrophysics Journal Letters on August 1st 2020. In the bibliography, it is referenced as O'Rourke et al., 2020b.

In 2010 two Nature papers were published (Campins et al. 2010, Rivkin & Emery, 2010) presenting a Near Infrared Absorption feature at 3.1 μm observed on asteroid (24) Themis interpreted as a coating of water ice on its surface producing that feature. In 2011, the same absorption feature was observed on (65) Cybele (Licandro et al. 2011) and since then multiple asteroids have presented the same feature. In all cases, because of the water ice link, these asteroids have been assumed to all have water ice on their surfaces. This paper disproves the hypothesis that this absorption feature is due to water ice on the surface of these asteroids.

We searched for water vapour using the Herschel Space Observatory HIFI instrument in the atmospheres of asteroids (24) Themis and (65) Cybele and did not make a detection. We did however generate sensitive upper limits which were, for the case of (24) Themis, 1 order of magnitude and for (65) Cybele two orders of magnitude better than all other previously published results. We applied our results to three different models (Thermophysical model, water production rate model, ice surface coverage model) with the aim of deriving upper limits for the water ice coverage on these asteroids. In our analysis we investigated the manner in which the water ice and the surface regolith had been mixed and touch upon two different mixing strategies (intimate mixing and areal mixing). We estimated that water ice intimately mixed with the asteroids' dark surface material would cover < 0.0017% for Themis and < 0.0033% for Cybele of their surfaces, while an areal mixture with very clean ice (bond albedo 0.8 for Themis and 0.7 for Cybele) would cover < 2.2% of the surface for Themis and < 1.5% for Cybele.

We find that the upper limit for surface ice present on these asteroids is not sufficient to produce the observed 3.1 μm absorption feature and as a result we conclude that this absorption feature cannot be due to water ice.

The Astrophysical Journal Letters, 898:L45 (8pp), 2020 August 1 https://doi.org/10.3847/2041-8213/aba62b

Low Water Outgassing from (24) Themis and (65) Cybele: 3.1 μm Near-IR Spectral Implications

L. O'Rourke[1], T. G. Müller[2], N. Biver[3], D. Bockelée-Morvan[3], S. Hasegawa[4], I. Valtchanov[5], M. Küppers[1], S. Fornasier[3,6], H. Campins[7], H. Fujiwara[8], D. Teyssier[5], and T. Lim[5]

[1] European Space Astronomy Centre, European Space Agency, Urbanización Villafranca del Castillo, Villanueva de la Cañada, E-28692 Madrid, Spain
lorourke@esa.int
[2] Max-Planck-Institut für extraterrestrische Physik, Giessenbachstrasse 1, D-85748 Garching, Germany
[3] LESIA, Observatoire de Paris, Université PSL, CNRS, Université de Paris, Sorbonne Université, 5 place Jules Janssen, F-92195 Meudon, France
[4] Institute of Space and Astronautical Science, Japan Aerospace Exploration Agency, 3-1-1 Yoshinodai, Chuo-ku, Sagamihara, Kanagawa 252-5210, Japan
[5] Telespazio Vega UK Ltd. for ESA/ESAC, Urbanización Villafranca del Castillo, Villanueva de la Cañada, E-28692, Madrid, Spain
[6] Institut Universitaire de France (IUF), 1 rue Descartes, F-75231 Paris Cedex 05, France
[7] University of Central Florida, P.O. Box 162385, Orlando, FL 32816-2385, USA
[8] Subaru Telescope, National Astronomical Observatory of Japan, 650 North A'ohoku Place, Hilo, HI 96720, USA
Received 2020 May 31; revised 2020 July 10; accepted 2020 July 13; published 2020 July 31

Abstract

Asteroids (24) Themis and (65) Cybele have an absorption feature at 3.1 μm reported to be directly linked to surface water ice. We searched for water vapor escaping from these asteroids with the Herschel Space Observatory Heterodyne Instrument for the Far Infrared. While no H_2O line emission was detected, we obtain sensitive 3σ water production rate upper limits of $Q(H_2O) < 4.1 \times 10^{26}$ molecules s^{-1} for Themis and $Q(H_2O) < 7.6 \times 10^{26}$ molecules s^{-1} for Cybele. Using a thermophysical model, we merge data from the Subaru/Cooled Mid-Infrared Camera and Spectrometer and the Herschel/Spectral and Photometric Imaging Receiver with the contents of a multi-observatory database to derive new radiometric properties for these two asteroids. For Themis, we find a thermal inertia $\Gamma = 20^{+25}_{-10}$ J m^{-2} s$^{-1/2}$ K^{-1}, a diameter 192^{+10}_{-7} km, and a geometric V-band albedo $p_V = 0.07 \pm 0.01$. For Cybele, we obtain a thermal inertia $\Gamma = 25^{+28}_{-19}$ J m^{-2} s$^{-1/2}$ K^{-1}, a diameter 282 ± 9 km, and an albedo $p_V = 0.042 \pm 0.005$. Using all inputs, we estimate that water ice intimately mixed with the asteroids' dark surface material would cover <0.0017% (for Themis) and <0.0033% (for Cybele) of their surfaces, while an areal mixture with very clean ice (Bond albedo 0.8 for Themis and 0.7 for Cybele) would cover <2.2% (for Themis) and <1.5% (for Cybele) of their surfaces. While surface (and subsurface) water ice may exist in small localized amounts on both asteroids, it is not the reason for the observed 3.1 μm absorption feature.

Unified Astronomy Thesaurus concepts: Asteroids (72); Main belt asteroids (2036); Main-belt comets (2131); Comets (280); Small solar system bodies (1469); Astronomy data modeling (1859)

1. Introduction

Observational and theoretical data suggest that solar system objects located in the main asteroid belt hold more water ice than originally thought. Indeed, the detection of water vapor on (1) Ceres (Küppers et al. 2014; Combe et al. 2016), asteroids that present cometary behavior (active asteroids; Hsieh & Jewitt 2006), and 3.1 μm absorption features in asteroid reflectance spectra (Campins et al. 2010; Licandro et al. 2011) have reinforced this line of thinking. Hydrated minerals (any mineral containing H_2O or OH) and water ice are known to have strong spectral absorptions in the ~2.5–3.5 μm wavelength range (Rivkin et al. 2002). Features at 0.7 and 2.7 μm are attributed to the presence of hydrated minerals and those at ~3.05 μm to water ice.

Takir & Emery (2012) examined the distribution and abundance of hydrated minerals on 28 outer main-belt asteroids and proposed four 3 μm spectral groups based on the absorption shapes observed: Ceres-like, Europa-like, rounded, and sharp. Of the four absorption shapes, only the rounded 3 μm band shape has been linked to the presence of water ice on the surface. Besides being observed on both Themis (Fornasier et al. 1999; Campins et al. 2010; Rivkin & Emery 2010) and 65 Cybele (Licandro et al. 2011), it has been found on numerous other asteroids, e.g., (76) Freia (Hargrove et al. 2012) and (361) Bononia (Usui et al. 2019), correlating well with laboratory experiments suggesting (Rivkin & Emery 2010) that a fine coating of ice on pyroxene grains mixed with amorphous carbon was covering the entire surface of these asteroids.

Asteroid (24) Themis is the parent body of the Themis family of asteroids located at the edge of the main belt and consisting of about 5000 members (Nesvorny 2012), mostly belonging to primordial C and B type (Fornasier et al. 2016a). In addition, to the 3.1 μm feature, the asteroid also has an absorption feature at approximately 2.76 μm associated with hydrated minerals (Usui et al. 2019), with no feature at 0.7 μm. Asteroid (65) Cybele, a P-type asteroid, is the most prominent member of a primitive outer-edge main-belt asteroid population known as the Cybele asteroids. Although it has the 3.1 μm feature, the asteroid has no hydrated features at 0.7 or 2.76 μm (Usui et al. 2019).

Besides the search for hydration in asteroids with spectral features from hydroxyl-bearing minerals (Takir & Emery 2012; Usui et al. 2019) or oxidized iron in phyllosilicates (Fornasier et al. 2014), the detection of gaseous water vapor or its disassociation products provides a more direct way to identify the presence of water. Up to now, water vapor has not been detected on Themis or Cybele, although upper limits have been derived for each.

Optical spectra of the two asteroids were obtained (Jewitt & Guilbert-Lepoutre 2012) from the Keck I 10 m telescope to

Table 1
Observations and Observing Conditions for the Previously Unpublished Measurements Used in This Paper

Target	Observatory and Instrument	ObsID	Date/Time (UT)	rh (au)	Δ (au)	α (deg)
Themis	Herschel HIFI (556.936 GHz)	1342262585	2013 Jan 30 17:30:38	2.92	2.37	18.1
	Subaru COMICS (*N*-band 8.8 μm)	n/a	2003 Jun 20 06:46:30	2.87	2.64	20.7
	Subaru COMICS (*N*-band 11.7 μm)	n/a	2003 Jun 20 06:43:30	2.87	2.64	20.7
Cybele	Herschel HIFI (556.936 GHz)	134225765	2012 Dec 21 16:53:19	3.52	3.11	15.5
	Herschel SPIRE (large map; 250/350/500 μm)	134187509	2009 Dec 1 13:14:28	3.45	3.27	16.6
		134187511	2009 Dec 1 13:44:47	3.45	3.27	16.6
	Herschel SPIRE (small map; 250/350/500 μm)	134228344	2011 Sep 8 16:48:43	3.80	4.09	14.1
		134230779	2011 Oct 10 22:51:21	3.79	3.61	15.2
		134244177	2012 Apr 12 19:47:23	3.72	3.86	15.1
		134244840	2012 Apr 22 18:30:51	3.72	3.99	14.4
		134254082	2012 Oct 28 19:50:08	3.57	3.93	14.2
		134255059	2012 Nov 15 00:37:22	3.56	3.68	15.6
		134257368	2012 Dec 17 23:39:25	3.53	3.16	15.7

Note. Columns: target (the two asteroids), observatory and instruments used, ObsID (observation ID reference number), date and time in UT, rh (heliocentric distance), Δ (Earth to asteroid distance), α (phase angle).

search for outgassed CN, a photodissociation product of HCN. An average CN/H_2O ratio of 0.3% was applied (as done for comets) to these asteroids, and upper limits for the water production rate of $Q(H_2O) < 1.3 \times 10^{28}$ molecules s^{-1} for Themis and $Q(H_2O) < 1.2 \times 10^{28}$ molecules s^{-1} were derived. A global coverage of water ice was discarded by the authors with these upper limits constraining the ice coverage on the Earth-facing asteroids' surface to be less than 10% based upon the presence of "relatively clean" (unmixed) ice with a Bond albedo >0.3.

Radio and UV observational searches for OH emission around Themis were performed (Lovell et al. 2010) using the National Radio Astronomy Observatory 100 m Green Bank Telescope and the Lowell Observatory 1.1 m Hall Telescope. A 3σ upper limit for $Q(H_2O)$ of 1×10^{28} molecules s^{-1} was obtained.

A more recent study (Mckay et al. 2017) presented the result of a nondetection following a search for gaseous H_2O at optical wavelengths using the forbidden oxygen line at 6300.3 Å, in line with similar observations performed on comets (McKay et al. 2014, 2015). While no detection was made, an upper limit of $Q(H_2O) < 4.5 \times 10^{27}$ molecules s^{-1} was provided for Themis, and conclusions equivalent to Jewitt & Guilbert-Lepoutre (2012) were reached regarding the localized nature and purity of the ice needed to match the upper limit obtained.

The Heterodyne Instrument for the Far Infrared (HIFI; de Graauw et al. 2010) on board the ESA Herschel Space Observatory (Pilbratt et al. 2010) has proven to be the most sensitive instrument ever built for directly observing water vapor on comets (Bockelée-Morvan et al. 2010), as well as in the asteroid belt. Indeed, it was through use of HIFI that H_2O gas was successfully detected around (1) Ceres (Küppers et al. 2014).

In Section 2 the observations of Cybele and Themis obtained by HIFI, as well as those from the Subaru/Cooled Mid-Infrared Camera and Spectrometer (COMIC) and Herschel/Spectral and Photometric Imaging Receiver (SPIRE) instruments, are presented, and the data are analyzed. In Section 3 we present new radiometric properties derived from our thermophysical model (TPM). In Section 4 we feed in our radiometric properties to derive upper limits for the water production rate of both asteroids. In Section 5, we calculate the fraction of ice coverage required to achieve this upper limit, discuss our results, and present our conclusions.

2. Observations and Data Analysis

2.1. Herschel HIFI Observations

Themis was observed with HIFI on Herschel on 2012 January 30 (see Table 1). The asteroid was traveling inbound (2.92 au) and close to perihelion (2.75 au) when the observation was carried out. Cybele was observed with HIFI on 2012 December 21 (see Table 1) when the asteroid was 3.52 au from the Sun and inbound, having already passed aphelion (3.8 au). It is important to highlight that with the low escape velocity from these asteroids, any escaping water vapor would have been visible to Herschel independent of its source location, as the footprint of the telescope was much larger than the asteroids themselves.

The line emission from the fundamental ortho-H_2O 1_{10}–1_{01} line at 556.936 GHz was searched for in the lower sideband of the HIFI band 1b mixer. The observations were performed in the frequency-switching observing mode using both the wide-band spectrometer (WBS) and the high-resolution spectrometer (HRS). The spectral resolution of the WBS is 1 MHz (0.54 km s^{-1} at the frequency of the observed line), while the HRS was used in its high-resolution mode with a resolution of 120 kHz (0.065 km s^{-1}). Initial processing of the HIFI data set was carried out using the standard HIFI processing pipeline of the Herschel Interactive Processing Environment v15.0.1 (HIPE; Ott 2010), followed by processing with the GILDAS CLASS software.

In CLASS, vertical and horizontal polarizations were folded and averaged. The frequency-switching observing mode introduces quite a strong baseline ripple, which was removed through a polynomial baseline correction performed on the final spectra. The averaged and baseline-corrected HRS spectra of the two asteroids are shown in Figures 1(a) and (b). The pointing offset of both the vertical and the horizontal polarization spectra is 3.″5 in band 1b with respect to the target position. The half-power beam width is 38.″1 at 557 GHz. The main beam brightness temperature scale was computed using a forward efficiency of 0.96 and a beam

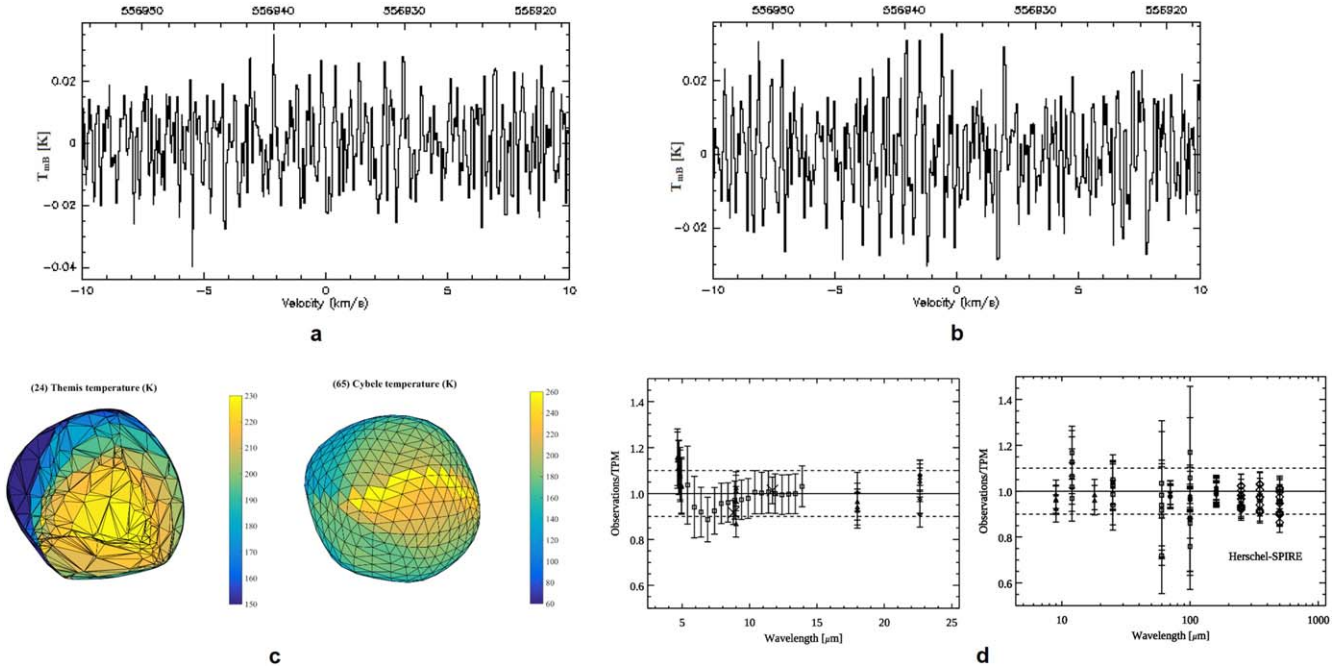

Figure 1. Averaged HIFI spectra and thermophysical modeling output. Shown are the HRS-averaged spectra for (a) asteroid Themis and (b) asteroid Cybele with TPM outputs (c) for Themis (left) and Cybele (right). These outputs represent the Herschel view with orientation "ecliptic sky" at the specific HIFI observing start epochs. The plots in panel (d) show the observations divided by the TPM predictions using the best solution described in the text as a function of wavelength for Themis (left) and Cybele (right). For Themis, the data shown are the good photometric data points coming from Spitzer-IRS (squares), Subaru (crosses), Akari below 5 and above 18 μm (triangles), and WISE-W4 at 22 μm (diamonds). For Cybele, the data are IRAS (squares); AKARI (triangles); ISOCAM (crosses); and PACS, SPIRE, and Spitzer-IRS (diamonds), with identification linked to wavelength.

Table 2
Output Results Following Processing of the Data in Table 1

Target	Herschel/HIFI		Subaru/COMICS			Herschel/SPIRE					
	Line Area 1σ mK km s^{-1} (HRS)	Line Area 1σ mK km s^{-1} (WBS)	Airmass	Flux (Jy)	Err. (Jy)	PSW Flux (Jy)	PSW Err. (Jy)	PMW Flux (Jy)	PMW Err.(Jy)	PLW Flux (Jy)	PLW Err. (Jy)
Themis	2.98	2.82	1.27	3.81	0.22			n/a			
			1.26	11.50	0.66						
Cybele	2.96	2.68		n/a		1.680	0.092	0.896	0.049	0.450	0.025
						1.181	0.065	0.630	0.035	0.307	0.017
						0.993	0.055	0.528	0.029	0.260	0.015
						0.857	0.047	0.459	0.025	0.229	0.013
						0.937	0.052	0.493	0.027	0.246	0.014
						1.040	0.057	0.546	0.030	0.271	0.015
						0.795	0.044	0.411	0.023	0.201	0.012
						1.673	0.092	0.883	0.049	0.431	0.024
						1.669	0.092	0.874	0.048	0.431	0.024

Note. Columns: target (the two asteroids), Herschel/HIFI (the calculated line areas for the HRS and WBS spectra for both asteroids), Subaru/COMICS instrument (the airmass, flux, and error obtained for Themis), Herschel/SPIRE instrument (the fluxes and errors derived from the SPIRE 250/350/500 μm observations of Cybele).

efficiency of 0.62. The output line area rms values are provided in Table 2.

Although the H_2O line is not detected in the resultant spectra for either of the two asteroids, sensitive upper limits could be derived. Table 2 provides a summary of the $1\sigma \int TmBdv$ line area upper limits calculated for both asteroids. The 1σ upper limits were computed on a $[-1, 1\ \mathrm{km\ s^{-1}}]$ window. The mean of the HRS- and WBS-derived values has been used to derive the 3σ upper limits of 8.7 mK km s^{-1} $\int TmBdv$ for Themis and 8.5 mK km s^{-1} $\int TmBdv$ for Cybele.

2.2. Observations Used for the Radiometric Analysis

2.2.1. Database of Existing Observations

For the radiometric analysis of these two asteroids, we used a wide range of thermal IR and submillimeter/millimeter measurements. Contrary to Cybele, Themis has not been well observed at thermal IR wavelengths. Besides using a Spitzer-IRS spectrum (Landsman et al. 2016), our study was limited to AKARI and Wide-field Infrared Survey Explorer (WISE) measurements. We used two different AKARI data sets. The

first was taken from the SBNAF public database[9] (Szakáts et al. 2020) and originated from the IRC instrument using the MIR-S (5.8–14.1 μm) and MIR-L (12.4–26.6 μm) cameras. For the second, produced by the IRC-NIR camera, we used the spectral data in the range 4.5–5.0 μm only (Usui et al. 2019), where the fluxes are pure thermal emission. We note that in the case of the WISE data, the W3 data (11.10 μm) were strongly saturated and the saturation-corrected fluxes were problematic, while the W4 (22.64 μm) data were only partly saturated and the saturation-corrected fluxes were of good quality. We added to these observational data sets the Subaru/COMICS data set as presented in Section 2.2.2.

In the case of Cybele, there exists a significant set of observational data available for our radiometric study. In particular, we used Herschel-PACS data (Alí-Lagoa et al. 2020); IRAS (Tedesco & Desert 2002) and AKARI measurements (Usui et al. 2011), both extracted from the SBNAF public database (Szakáts et al. 2020); UKIRT-MAX and Infrared Space Observatory (ISO)-ISOPHOT data (Müller & Lagerros 1998, 2002); AKARI data (Usui et al. 2019); multiple ground-based data from the literature and archives, as well as additional spectroscopic and photometric data from ISO-ISOPHOT and ISO-ISOCAM (Müller & Blommaert 2004a); and, finally, Spitzer-IRS data (Licandro et al. 2011). We added to this the Herschel SPIRE as explained in Section 2.2.3.

2.2.2. Subaru/COMICS Data Sets for Themis

The mid-infrared photometric observations for Themis were conducted using COMICS (Kataza et al. 2000), installed at the $f/12$ Cassegrain focus of the 8.2 m Subaru Telescope. The 320 × 240 pixel Si:As BIB detector for COMICS has 50 μm square pixels, giving a 42″ × 32″ field of view with a pixel scale of 0.″135. The *N*-band filters were centered on 8.8, 11.7, and 12.4 μm with effective bandwidths of 0.8, 1.0, and 1.2 μm, respectively. See Table 1.

To reduce the atmospheric and telescopic background radiation, a standard chopping and nodding method was used. Because it was positioned near Themis in the sky, HD 108985 was selected as an absolute calibration star (Cohen et al. 1999). The fluxes of Themis and HD 108985 as provided in Table 2 were measured through circular apertures with a diameter of more than four times that of the FWHM size using the APPHOT function in the IRAF software. Since the color differences between the spectral energy distributions of Themis and HD 108985 in the N88 and 11.7 filters were found to be about a few percent, color corrections for observations with COMICS were not performed.

2.2.3. SPIRE Data Sets for Cybele

The Herschel SPIRE instrument covering three far-infrared bands—250, 350, and 500 μm—observed Cybele nine times during the period 2009–2012. See Table 1. The observations were taken directly from the Herschel Science Archive.[10] Photometry was carried out using the timeline fitter method available in HIPE. The derived total monochromatic flux densities were color-corrected to account for the assumed spectral index of $\alpha = 2$. A flux calibration uncertainty of 5.5% was added in quadrature for the total error budget. The output fluxes corresponding to the three SPIRE wavelength bands and associated errors are provided in Table 2.

3. Thermophysical Modeling of the Two Asteroids

A TPM (Lagerros 1996, 1998; Müller & Lagerros 1998, 2002) was used to derive the radiometric properties of the two asteroids. This model has been successfully used in the study of near-Earth asteroids (Müller et al. 2004b, 2011, 2012), main-belt asteroids (Müller & Blommaert 2004a; O'Rourke et al. 2012), and more distant objects (Lim et al. 2010; Müller et al. 2019).

For both asteroids, we performed a radiometric analysis combining all available mid-to-far-IR measurements with the Subaru/COMICS and Herschel/SPIRE values, as described in Section 2.2 of this paper and presented in Tables 1 and 2.

For our work, we followed a similar strategy as in Alí-Lagoa et al. (2020, and references therein). In the case of Themis, nonconvex spin–shape solutions (Viikinkoski et al. 2017; based on two spin solutions from Hanuš et al. 2016), as well as two simpler convex solutions (DAMIT database), were tested against the available thermal measurements presented in Section 2.2 in our model. Since the data coverage in rotational phase, phase angle, aspect angle, and wavelength was very limited, it was not possible to identify the object's true spin and shape properties via our χ^2 approach.

We obtained a best fit, however, using the second convex spin–shape solution with $(\lambda_{\rm ecl}, \beta_{\rm ecl}) = (137°, 59°)$ and $P_{\rm sid} = 8.374187$ hr. This model has 2040 surface elements and 1022 vertices[11] (model ID1006; Hanuš et al. 2016). Our resulting derived radiometric properties are thermal inertia $\Gamma = 20^{+25}_{-10}$ J m^{-2} s$^{-1/2}$ K^{-1}, effective diameter $D_{\rm eff}$ = diameter 192^{+10}_{-7} km, and geometric *V*-band albedo $p_V = 0.07 \pm 0.01$ (connected to an absolute *V*-band magnitude of $H = 7.11$ mag from Oszkiewicz et al. 2011), for an intermediate-to-low level of surface roughness ($0.1 <$ rms < 0.5; Table 4). See Figures 1(c) (left) and (d) (left) for the Themis TPM output. While this multi-observatory data set output provides a diameter consistent with previously published values, it is lower than the NEATM-derived measurements based on Spitzer of 218 ± 1 km (Hargrove et al. 2015).

For Cybele, Viikinkoski et al. (2017) were able to eliminate the pole ambiguity via multiple AO images using a nonconvex shape model with a spin pole at $(\lambda_{\rm ecl}, \beta_{\rm ecl}) = (208 \pm 1°, -3 \pm 3°)$ and $P_{\rm sid} = 6.081435$ hr. They estimated a diameter of 296 ± 25 km, which is within 1σ of the earlier published radiometric diameter of 273 ± 11 km (Müller & Blommaert 2004a) and that published by Alí-Lagoa et al. (2020).

Alí-Lagoa et al. (2020) analyzed IRAS, AKARI, and Herschel-PACS measurements using the latest spin–shape solution (the ADAM model by Viikinkoski et al. 2017) with a spin pole at $(\lambda_{\rm ecl}, \beta_{\rm ecl}) = 208° \pm 1°, -3° \pm 3°$ and a rotation period of 6.08 hr. They found that a best-fitting radiometric diameter of 277^{+4}_{-2} km and thermal inertia value of 30^{+10}_{-15} J m^{-2} s$^{-1/2}$ K^{-1} could explain these thermal fluxes very well based on a reduced χ^2 minimum <1. Therefore, as in the case of Themis, we used the shape model with the size as a free parameter.

In our work, we used the same nonconvex shape model of Cybele as in Alí-Lagoa et al. (2020), which has 2040 surface elements and 1022 vertices[12] (DAMIT Database ID1843) with

[9] https://ird.konkoly.hu/

[10] The Herschel Science Archive website is https://herschel.esac.esa.int/Science_Archive.shtml.

[11] https://astro.troja.mff.cuni.cz/projects/damit/asteroid_models/view/1006

[12] https://astro.troja.mff.cuni.cz/projects/damit/asteroid_models/view/783

a spin pole at (λ_{ecl}, β_{ecl}) = (207, −6) and P_{sid} = 6.081435 hr. The reduced χ^2 minimum was at 0.75 for an intermediate surface roughness (rms of surface slopes of 0.4). We find an effective diameter $D_{eff} = 282 \pm 9$ km, a best-fit thermal inertia of $\Gamma = 25^{+28}_{-19}$ J m^{-2} s$^{-1/2}$ K^{-1}, and a geometric V-band albedo of $p_V = 0.042 \pm 0.005$ (connected to an absolute V-band magnitude of $H = 6.82$ mag from Oszkiewicz et al. 2011; Table 4). Our solution was found to match all photometric IR data points, as well as the Spitzer-IRS spectrum and the ISO-ISOCAM CVF spectrum (except in the range of the emission feature discussed in Müller & Blommaert 2004a). See Figures 1(c) (right) and (d) (right) for the resultant TPM output. The inclusion of the SPIRE data contributed to confirm that Cybele shows a normal submillimeter (spectral) emissivity behavior similar to many other large regolith-covered main-belt asteroids like Ceres, Pallas, and Juno (Müller & Lagerros 1998).

4. Outgassing Rate Upper Limits

To derive the upper limits on the water production rate for the two asteroids, we used a molecular excitation model that calculates the population of the rotational levels of water as a function of distance from the asteroid. Our excitation model takes into account collisions of water and electrons, and infrared pumping of the vibrational bands and treats self-absorption using the escape probability formalism (Zakharov et al. 2007; Biver et al. 2012, 2015). Further to this, the model takes into account the thermal background emission from the asteroid and nonconstant gas kinetic temperature radial profiles (Biver et al. 2019).

Input parameters to the model include the asteroid radius (from our TPM), electron density, gas expansion velocity, derived surface temperature (from our TPM, which includes surface roughness effects that enhance the temperatures significantly), and gas temperature. Synthetic spectra are computed taking into account the transfer of line radiation of ortho-water in the asteroidal "atmosphere." Since the electron density is not well constrained, a scaling factor of $x_{ne} = 0.2$ with respect to the standard profile derived from observations of comet 1P/Halley has been used (Hartogh et al. 2010). For the radial gas density profile, we adopted the standard Haser law (Haser 1957). We assumed a nominal expansion velocity v_{exp} of 0.5 km s^{-1} (characteristic of weak comets).

Assuming a rarefied free-expanding exosphere for the asteroids and based on these "nominal" x_{ne} and v_{exp} values, we calculated the water production rates (see Table 3) based on gas kinetic temperature values of 10, 20, and 50 K, as well as a set of variable temperature profiles. We included 50 K because temperatures of approximately 50–60 K are expected for Ceres at 3000 km from its body center (Küppers et al. 2014). We obtained similar results for the two asteroids, irrespective of the temperature profile applied. This suggests that we are more likely sensitive to the gas temperature at some distance from the surface where collisions become too weak.

We find that for the low production rates we estimate, water excitation is not affected significantly by electron collisions because of low electron densities. Applying a value of $x_{ne} = 0.2$ or 0.0 does not change our results. Using $x_{ne} = 1.0$ decreases the upper limits on the water production rate by 10%, and doubling the collision rate with neutrals decreases the values by 8%.

Taking into account the above findings, we added a column in Table 3 defining highly conservative 3σ upper limits for the water production rate of $Q(H_2O) < 4.1 \times 10^{26}$ molecules s^{-1} for Themis and $Q(H_2O) < 7.6 \times 10^{26}$ molecules s^{-1} for Cybele. These values were obtained by assuming a kinetic temperature of 10 K, a high expansion velocity v_{exp} of 0.7 km s^{-1}, and no excitation by photoelectrons, i.e., $x_{ne} = 0.0$. These upper limits provide more than an order of magnitude improvement on previously published $Q(H_2O)$ values, which are presented in the final column of Table 3 for comparison purposes. We also derived sensitive 3σ upper limits for the column density of $N_{col} < 0.58 \times 10^{12}$ cm s^{-1} for Themis and $N_{col} < 0.82 \times 10^{12}$ cm s^{-1} for Cybele (Tables 3 and 4).

5. Discussion and Conclusions

Using a sublimation model, we use the upper limits for the water-loss rate presented in Section 4 to produce equivalent upper limits for the percentage of exposed ice that is present on the surface of the two asteroids. In our analysis, we study the implications of mixing the ubiquitous dark dust and the ice present on the asteroid surfaces at both a fine scale (intimate mixing) and a more macroscopic level (areal mixing), whereby the level of mixing can affect the contribution of the ice albedo to the area-averaged albedo. For intimate mixing, laboratory experiments show that only a few weight percent of dust is sufficient to reduce the albedo of the ice well below 10% (Pommerol et al. 2015). In the areal mixing case, the cleaner the ice is (less mixed with the dust), the brighter (higher Bond albedo) and colder it will be, resulting in less sublimation. This leads to a higher area percentage coverage deduced from the water production rate for the areal mixing case than for the case of intimately mixed ice (Jewitt & Guilbert-Lepoutre 2012).

We used a sublimation model[13] (Cowan & A'Hearn 1979; slow rotator version) where the rotational pole is pointed toward the Sun. This is appropriate for bodies with a small thermal inertia, as is the case (from our TPM) for Themis and Cybele. This sublimation model provides the average water sublimation rate per surface unit, Z, at a given heliocentric distance. The upper limit on the area of exposed ice A_{exp} is obtained by dividing the upper limit on $Q(H_2O)$ by Z, and the upper limit on the fraction of the surface occupied by ice (f_{ice}) is obtained by dividing A_{exp} by the asteroid surface area ($4\pi r_N^2$, where r_N is the effective radius). In addition to the heliocentric distance, the input parameters of the model include the Bond albedo of the icy material and the infrared emissivity equal to 0.9.

Figure 2 shows the derived upper limits for the ice coverage of the two asteroids. We plot our water production upper limits against the Bond albedo and the percentage ice coverage; acceptable solutions must lie on or below the water production curves, as otherwise, gas production through sublimation would have been large enough for detection by HIFI. In this figure, we study two scenarios for the water ice interaction with the ubiquitous dark dust of the asteroid. In the first scenario, we gradually mix a low geometric albedo (0.02–0.04) surface dust with ice of an increasing Bond albedo value (brightness), resulting in an areal-type mixture. In the second scenario, we study the intimate mixture case on the basis that the Bond albedo of the asteroid represents the combined albedos of the icy dust mixture.

[13] https://pdssbn.astro.umd.edu/tools/ma-evap/

Table 3
H_2O Production Rate ($Q(H_2O)$) and Column Density (N_{col}) Derived for Different Gas Kinetic Temperatures

		Kinetic Temperature T_{kin} (K)				Variable Temperature T_{var} (K)			Previously Published Data
		Upper Limits	10	20	50	($T_f = 10$)	($T_f = 20$)	($T_f = 50$)	
Themis	$Q(H_2O)$ (molecules s^{-1})	$<4.1 \times 10^{26}$	$<3.12 \times 10^{26}$	$<2.78 \times 10^{26}$	$<2.5 \times 10^{26}$	$<2.63 \times 10^{26}$	$<2.59 \times 10^{26}$	$<2.55 \times 10^{26}$	(i) $< 1.3 \times 10^{28}$, (ii) $< 1.0 \times 10^{28}$, (iii) $< 4.5 \times 10^{27}$
	N_{col} (cm^{-2})	$<0.58 \times 10^{12}$	$<0.58 \times 10^{12}$	$<0.52 \times 10^{12}$	$<0.47 \times 10^{12}$	$<0.49 \times 10^{12}$	$<0.49 \times 10^{12}$	$<0.48 \times 10^{12}$	
Cybele	$Q(H_2O)$ (molecules s^{-1})	$<7.6 \times 10^{26}$	$<5.76 \times 10^{26}$	$<5.04 \times 10^{26}$	$<4.46 \times 10^{26}$	$<4.71 \times 10^{26}$	$<4.63 \times 10^{26}$	$<4.53 \times 10^{26}$	(i) $< 1.2 \times 10^{28}$
	N_{col} (cm^{-2})	$<0.82 \times 10^{12}$	$<0.84 \times 10^{12}$	$<0.73 \times 10^{12}$	$<0.65 \times 10^{12}$	$<0.69 \times 10^{12}$	$<0.67 \times 10^{12}$	$<0.66 \times 10^{12}$	

Note. The temperatures are either constant throughout the coma (T_{kin}) or variable ($T_{var} = (T_0–T_f)\ r_N/r + T_f$), with $T_0 = 155$ K for Themis and $T_0 = 138$ K for Cybele, corresponding to 86% of the surface temperature (Crifo et al. 2002); r_N is the radius of the asteroid derived from our TPM, and r is the distance to the body center. The "Upper Limits" column corresponds to the worst-case estimate of the upper limit, whereby $T_{kin} = 10$ K, $v_{exp} = 0.7$, and $x_{ne} = 0$ (see text). All other estimates are performed with the optimal values $v_{exp} = 0.5$ and $x_{ne} = 0.2$. Previously published data references are as follows: (i) Jewitt & Guilbert-Lepoutre (2012); (ii) Lovell et al. (2010); and (iii) Mckay et al. (2017).

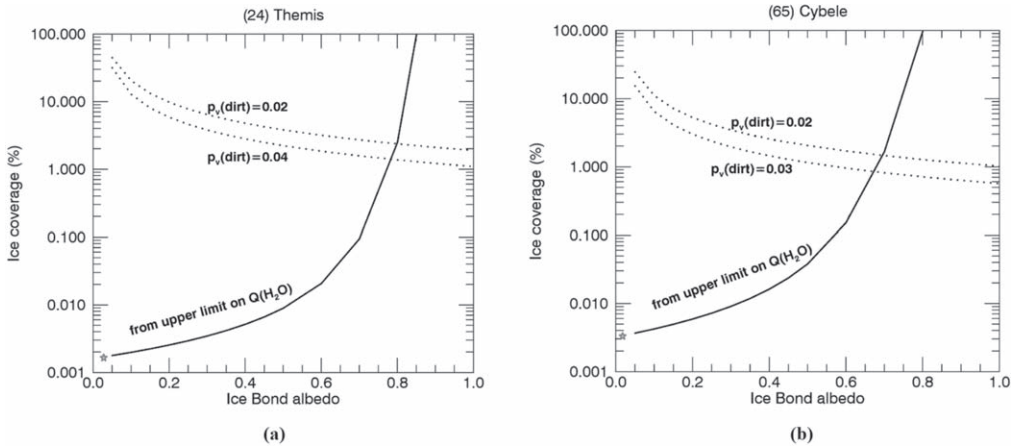

Figure 2. Derived allowed values for the ice coverage for (a) Themis and (b) Cybele as a function of the Bond albedo of surface ice. The solid curve represents the Q (H_2O) constraint derived for each asteroid. Acceptable solutions must lie on or below this curve, as otherwise, gas production through sublimation would have been large enough for detection by HIFI. The dotted curves reflect the albedo constraint (see text) for geometric albedos of surface dust only p_v(dust) in the range 0.02–0.04 for Themis and 0.02–0.03 for Cybele. Acceptable solutions for the areal mixing case must lie along or between these dotted curves to guarantee the area-averaged albedo matches our modeled TPM value. The purple stars represent the positions of the corresponding intimate mixing results.

Table 4
Summary of Main Results of This Paper

Target	$Q(H_2O)$ (molecules s^{-1})	N_{col} (cm^{-2})	Intimate f_{ice} (%)	Areal f_{ice} (%)	Γ (J m^{-2} $s^{-1/2}$ K^{-1})	D (km)	p_V (Geometric)	p_V (Bond)
Themis	$<4.1 \times 10^{26}$	$<0.58 \times 10^{12}$	0.0017	1.4–2.2	20^{+25}_{-10}	192^{+10}_{-7}	0.07 ± 0.007	0.027
Cybele	$<7.6 \times 10^{26}$	$<0.82 \times 10^{12}$	0.0033	0.8–1.5	25^{+28}_{-19}	282 ± 9	$0.042^{+0.03}_{-0.02}$	0.019

Note. Here $Q(H_2O)$ is the water production rate upper limit, N_{col} is the column density upper limit, f_{ice} is the fraction of ice coverage depending on whether it is an intimate or areal mixture, Γ is the thermal inertia, D is the effective diameter, and p_V is the V-band geometric and Bond albedo.

Applying scenario 1 and in line with the approach of Jewitt & Guilbert-Lepoutre (2012), we plot two dotted lines in Figure 2 matching with geometric albedo values for p_v (dust) = 0.02–0.04 for Themis and 0.02–0.03 for Cybele, corresponding to the least reflective asteroid surfaces known. Due to its already very low albedo (from our TPM) of 0.042, 0.03 is set as a conservative value for the Cybele upper range. The two constraints (water production rate limit and albedo) are found to be acceptably achieved only if the water ice on the two asteroids is very bright (Bond albedo of 0.8 for Themis, 0.7 for Cybele) and the water ice covers <2.2% of the surface for Themis and <1.5% for Cybele. Upper limits of 2.2% and 1.5% ice, respectively, on the surface of the Themis and Cybele asteroids will lead to similar upper limits in the depth of water ice in the 3.1 μm absorption feature, as pure water ice is fully absorbing at this wavelength (e.g., Protopapa et al. 2014). As the 3.1 μm band depth of both asteroids is ~10% of the local continuum (Rivkin & Emery 2010; Licandro et al. 2011), we conclude that for areal mixing, the 3.1 μm absorption feature cannot be explained by surface water ice on these asteroids.

In scenario 2, we assume that the water ice is intimately mixed with the dark surface material of the asteroids (as observed on other solar system objects, including 67P) and, as such, corresponds to the area-averaged Bond albedo of the asteroid. A value for the bolometric Bond albedo (A) of 0.027 was calculated for Themis and 0.019 for Cybele based on the formula $A = p * q$, where p is the bolometric geometric albedo assumed to be equal to the V-band albedo p_V and $q = 0.290 + 0.684 * G$. Here G is the slope parameter in the H-G system (Bowell et al. 1989), and it was determined to be 0.16 for Themis and 0.23 for Cybele (Oszkiewicz et al. 2011). From Figure 2 (purple stars) and based on these Bond albedo values, we obtain upper limits for the fraction of the surface covered by ice to be 0.0017% for Themis and 0.0033% for Cybele, meaning that only a tiny fraction of intimately mixed ice is present on the surface of these asteroids. These values are an order of magnitude lower than those obtained by Jewitt & Guilbert-Lepoutre (2012) and Mckay et al. (2017). Like them, we conclude that such an ice–dust mixture percentage is entirely insufficient to explain the 3.1 μm absorption.

To appreciate the possible percentage of intimately mixed ice below the surface, we compare it with values obtained from 67P/Churyumov–Gerasimenko. On 67P, the ice was observed to be intimately mixed with the dust, visible in localized regions, and considered to be just below the surface (Fornasier et al. 2016b). We applied the above model using $Q(H_2O)$ measured values of 67P at 3 au based on a Bond albedo of 0.012 at 3 au (Fornasier et al. 2015) and emissivity of 0.97 (Spohn et al. 2015). We find an ice coverage of 0.6% at 3 au pre-perihelion and 0.2% at 3 au post-perihelion, percentages more than 2 orders of magnitude higher than those derived for the asteroids. In this comparison, if ice is indeed present just below the asteroid's surface and intimately mixed with dust, as in comets, then there is a very low amount present.

While surface water ice may not be the reason for the 3.1 μm absorption feature, the 3 μm region is known to host other volatile species that do show similar absorption curves. The ammonium (NH^{4+}) ion has a band center near 3.1 μm and was interpreted to be present in the (1) Ceres spectrum (King et al. 1992). Poch et al. (2020) recently compared the 3.2 μm spectra of ammonium salts found on comet 67P (Altwegg et al. 2020) with the 3.1 μm feature on Themis and Cybele, finding a distinct correlation between the two. Similar features have been observed on the Jupiter Trojan asteroids and the small moon

Himalia matching with ammoniated minerals on their surfaces (Brown 2016; Poch et al. 2020) at this wavelength. Further to the above, minerals such as brucite (Beck et al. 2011), magnetite (Yang & Jewitt 2010), and adsorbed water molecules in lunar regolith (Clark 2009) all represent other possible alternative explanations to the presence of surface water ice.

In conclusion, we present highly conservative, sensitive 3σ upper limits for the water production rate on (24) Themis and (65) Cybele. Using these limits to model the maximum surface ice fraction, we find that the 3.1 μm absorption feature cannot be explained by water ice, be it areal or intimately mixed. Recognizing the numerous spacecraft that have visited asteroids and comets where far too little surface ice has been detected to be visible in disk-integrated spectra, our results serve to confirm the continued difficulty in observing ice from the Earth, whether via ground- or space-based observatories.

This study was based in part on data collected using the Subaru Telescope, which is operated by NAOJ. S.H. and H.F. would like to acknowledge H. Kataza, T. Ootsubo, T. Sekiguchi, and I. Yamamura for their helpful comments and discussions. The work of S.H. was supported by the Hypervelocity Impact Facility, ISAS, JAXA. T.M. has received funding from the European Union's Horizon 2020 Research and Innovation Programme under grant Agreement No. 687378 as part of the project "Small Bodies Near and Far" (SBNAF). We acknowledge the use of the GILDAS CLASS software (http://www.iram.fr/IRAMFR/GILDAS) in the processing of the HIFI data. We would like to thank the anonymous referee for the insightful and helpful comments provided.

ORCID iDs

L. O'Rourke https://orcid.org/0000-0002-8507-3772
T. G. Müller https://orcid.org/0000-0002-0717-0462
D. Bockelée-Morvan https://orcid.org/0000-0002-8130-0974
S. Hasegawa https://orcid.org/0000-0001-6366-2608
I. Valtchanov https://orcid.org/0000-0001-9930-7886
M. Küppers https://orcid.org/0000-0002-5666-8582
S. Fornasier https://orcid.org/0000-0001-7678-3310
H. Fujiwara https://orcid.org/0000-0001-6536-8656

References

Alí-Lagoa, V., Müller, T. G., Kiss, C., et al. 2020, A&A, 638, A84
Altwegg, K., Balsiger, H., Hänni, N., et al. 2020, NatAs, 4, 533
Beck, P., Quirico, E., & Sevestre, D. 2011, A&A, 526, A85
Biver, N., Bockelée-Morvan, D., Hofstadter, M., et al. 2019, A&A, 630, A19
Biver, N., Bockelée-Morvan, D., Morena, R., et al. 2015, SciA, 1, e1500863
Biver, N., Crovisier, J., Bockelée-Morvan, D., et al. 2012, A&A, 539, A68
Bockelée-Morvan, D., Biver, N., Crovisier, J., et al. 2010, BAAS, 42, 946
Bowell, E. G., Hapke, B., & Domingue, D. 1989, in Asteroids II, ed. R. P. Binzel, T. Gehrels, & M. S. Matthews (Tucson, AZ: Univ. of Arizona Press), 524
Brown, M. E. 2016, AJ, 152, 159
Campins, H., Hargrove, K., Pinilla-Alonso, N., et al. 2010, Natur, 464, 1320
Clark, R. N. 2009, Sci, 326, 562
Cohen, M., Walker, R. G., Carter, B., et al. 1999, AJ, 117, 1864
Combe, J. Ph., McCord, T. B., Tosi, F., et al. 2016, LPSC, 47, 1820
Cowan, J. J., & A'Hearn, M. F. 1979, M&P, 21, 155
Crifo, J. F., Loukianov, G. A., Rodionov, A. V., et al. 2002, Icar, 156, 249
de Graauw, T., Helmich, F. P., Phillips, T. G., et al. 2010, A&A, 518, L6
Fornasier, S., Hasselmann, P. H., Barucci, M. A., et al. 2015, A&A, 583, A30
Fornasier, S., Lantz, C., Barucci, M. A., et al. 2014, Icar, 233, 163
Fornasier, S., Lantz, C., Perna, D., et al. 2016a, Icar, 269, 1
Fornasier, S., Lazzarin, M., Barbieri, C., et al. 1999, A&AS, 135, 65
Fornasier, S., Mottola, S., Keller, H. U., et al. 2016b, Sci, 54, 1566
Hanuš, J., Durech, J., Oszkiewicz, D. A., et al. 2016, A&A, 586, A108
Hargrove, K. D., Emery, J. P., Campins, H., et al. 2015, Icar, 254, 150
Hargrove, K. D., Kelley, M. S., Campins, H., et al. 2012, Icar, 221, 453
Hartogh, P., Crovisier, J., de Val-Borro, M., et al. 2010, A&A, 518, L150
Haser, L. 1957, Liege Inst. Astrophys. Rep., 394
Hsieh, H. H., & Jewitt, D. 2006, Sci, 312, 561
Jewitt, D., & Guilbert-Lepoutre, A. 2012, AJ, 143, 21
Kataza, H., Okamoto, Y., Takubo, S., et al. 2000, Proc. SPIE, 4008, 1144
King, T. V. V., Clark, R. N., Calvin, W. M., et al. 1992, Sci, 255, 1551
Küppers, M., O'Rourke, L., Bockelée-Morvan, D., et al. 2014, Natur, 505, 525
Lagerros, J. S. V. 1996, A&A, 310, 1011
Lagerros, J. S. V. 1998, A&A, 332, 1123
Landsman, Z., Licandro, J., Campins, H., et al. 2016, Icar, 269, 62
Licandro, J., Campins, H., Kelley, M., et al. 2011, A&A, 525, A34
Lim, T. L., Stansberry, J., Müller, T. G., et al. 2010, A&A, 518, 148
Lovell, A. J., Fernendez, Y. R., Campins, H., et al. 2010, BAAS, 42, 1036
Mckay, A. J., Bodewits, D., & Jian-Yang, L. 2017, Icar, 286, 308
McKay, A. J., Chanover, N. J., di Santi, M. A., et al. 2014, Icar, 231, 193
McKay, A. J., Cochran, A., Disanti, M. A., et al. 2015, Icar, 250, 504
Müller, T. G., & Blommaert, J. A. D. L. 2004a, A&A, 418, 347
Müller, T. G., Durech, J., Hasegawa, S., et al. 2011, A&A, 525, 145
Müller, T. G., Kiss, C., Ali-Lagoa, V., et al. 2019, Icar, 334, 39
Müller, T. G., & Lagerros, J. S. V. 1998, A&A, 338, 340
Müller, T. G., & Lagerros, J. S. V. 2002, A&A, 381, 324
Müller, T. G., O'Rourke, L., Barucci, A. M., et al. 2012, A&A, 548, 36
Müller, T. G., Sterzik, M. F., Schütz, O., et al. 2004b, A&A, 424, 1075
Nesvorny, D. 2012, Nesvorny HCM Asteroid Families V2.0, EAR-A-VARGBDET-5-NESVORNYFAM-V2.0, NASA Planetary Data System
O'Rourke, L., Müller, T. G., Valtchanov, I., et al. 2012, P&SS, 55, 192
O'Rourke, L., Snodgrass, C., de Val Borro, M., et al. 2013, ApJL, 774, L13
Oszkiewicz, D. A., Muinonen, K., Bowell, E., et al. 2011, JQSRT, 112, 1919
Ott, S. 2010, in ASP Conf. Ser. 434, Astronomical Data Analysis Software and Systems XIX, ed. Y. Mizumoto, K.-I. Morita, & M. Ohishi (San Francisco, CA: ASP), 139
Pilbratt, G. L., Riedinger, J. R., Passvogel, T., et al. 2010, A&A, 518, L1
Poch, O., Istiqomah, I., Quirico, E., et al. 2020, Sci, 367, 7462
Pommerol, A., Thomas, N., El-Maary, M. R., et al. 2015, A&A, 583, A25
Protopapa, S., sunshine, J., Feaga, L. M., et al. 2014, Icar, 238, 191
Rivkin, A. S., & Emery, J. P. 2010, Natur, 464, 1322
Rivkin, A. S., Howell, E. S., Vilas, F., et al. 2002, in Asteroids III, ed. W. F. Bottke, Jr. et al. (Tucson, AZ: Univ. Arizona Press), 235
Spohn, T., Knollenberg, J., Ball, A. J., et al. 2015, Sci, 349, 6247
Szakáts, R., Müller, T. G., Alí-Lagoa, V., et al. 2020, A&A, 635, A54
Takir, D., & Emery, J. P. 2012, Icar, 219, 641
Tedesco, E. E., & Desert, F.-X. 2002, AJ, 123, 1056
Usui, F., Hasegawa, S., Ootsubo, T., et al. 2019, PASJ, 71, 1
Usui, F., Kuroda, D., Müller, T. G., et al. 2011, PASJ, 63, 1117
Viikinkoski, M., Hanuš, J., Kaasalainen, M., et al. 2017, A&A, 607, A117
Yang, B., & Jewitt, D. 2010, AJ, 140, 692
Zakharov, V., Bockelée-Morvan, D., Biver, N., et al. 2007, A&A, 473, 303

Chapter 4

Previously published works linked to the thesis objectives

4.1 Localised Sources of Water vapour on dwarf planet (1) Ceres

4.1.1 Motivation & Link to Objective 2

The search for water on the surface of (1) Ceres was the key motivation behind a Nature paper released in 2013 titled "Localised Sources of water vapour on the dwarf planet (1) Ceres" (Küppers & O'Rourke et al., 2013) – see Annex A.

Taking into account that (a) Ceres was believed to be differentiated into a silicate core with an icy mantle (b) hydrated minerals had been found on its surface and (c) the presence of water vapour around Ceres was suggested by a marginal detection of the photodissociation product of water, hydroxyl (A'Hearn et al. 1992) which could not be confirmed by later, more sensitive observations (Rousselot et al. 2011), there was a strong push to search for water vapour using the Herschel HIFI instrument; one of the most sensitive instruments ever constructed.

With a detection by HIFI, it would represent the first time that water ice was discovered on an asteroid in the asteroid belt providing significant arguments for the possibility that the Ocean's water originated from both asteroids and comets. The campaign to search for water on (1) Ceres formed part of a Guaranteed Time Proposal submitted by O'Rourke et al. to the Herschel Science Centre.

Ceres represents the biggest object in the asteroid belt having a diameter of 950 km with significant studies having suggested it has an interior ocean. The techniques in use for this paper, the findings we made, and the follow-up of these findings within the planetary science community make this an important paper to take into account in the scope of this thesis and, in particular when addressing objective #2 : The search for and characterisation of surface/subsurface ice on asteroids.

4.1.2 Brief summary of Results

Two observations were carried out – the first in November 2011 where there was no detection. The second was in October 2012 where a detection was obtained. The scheduling of the observation requests were performed in discussion with the PI of the observing programme (LO'Rourke) as well as the type of observing mode to be used. The observations of (1) Ceres were carried out using the HIFI instrument. The ortho 1_{10}-1_{01}

H_2O line at 556.936GHz (λ= 0.54 mm) was observed in dual-beam switch (DBS) mode (see Figure C-7) in HIFI mixers band 1a in November 2011 and in October 2012. A follow-up observation (also a detection) performed in March 2013 also used DBS mode but with band 1b.

The results of this nature paper were significant in that they represented the first confirmed detection of water on an object in the asteroid belt.

Although the HIFI data showing detection was obtained in both HRS and WBS whereby the HRS had a better spectral resolution, it was decided to show in the Nature paper the WBS data due to its higher signal-to-noise. An example of the HRS detected absorption (reprocessed by LO'Rourke for this thesis) is presented in Figure 4-1 while the time averaged WBS data as presented in the Nature paper is plotted in Figure 4-2.

At the frequency of the water line, absorption in the thermal continuum of Ceres is clearly visible in the late 2012 observations, whereas in the 2013 data it is next to a weaker emission line detected at the 3σ level. In addition, the larger absorption strength on 11 October 2012 compared to the observations two weeks later and five months later suggests sporadic changes in the water evaporation. Given that the spin axis of Ceres is nearly perpendicular to its orbital plane (Carry et al. 2008], we expected seasonal variations driven by spin-axis obliquity to contribute little to the variability. The low outflow velocity (0.3–0.7km^{-1}) determined from the offset of the absorption line is comparable to the escape velocity of Ceres (about 0.52 kms^{-1}), showing that a fraction of the evaporated water does not escape from Ceres.

A modelling of the exosphere of Ceres using the DSMC considered that the water vapour was ejected from localized sources, and then slowed down in Ceres' gravity field (which has a 0.5km/sec escape velocity). Using a state-of-the-art two-dimensional excitation model to simulate the water spectra, which considers excitation by radiation from Ceres and the Sun and collisional excitation, the temporal variation of the absorption line observed on 6 March 2013 was found to be well described by a model that considered outgassing from two localised sources on the surface. (see Figure 4-2).

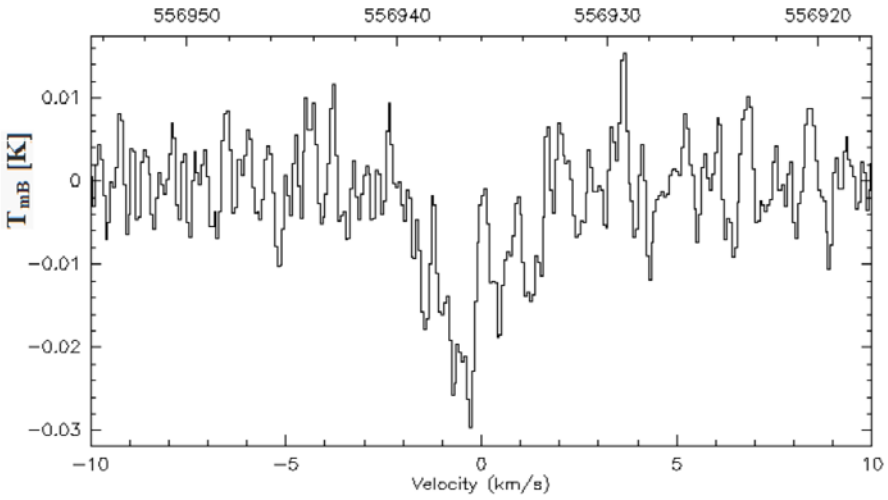

Figure 4-1 : This figure shows the HRS averaged spectra detection from the 11th October 2012; processed by LO'Rourke using HIPE 15.0.1 (Ott 2010), with the spectra exported to CLASS and then averaged with a polynomial baseline correction applied outside of a -1,1 window. A clear absorption feature is visible in the HRS signal.

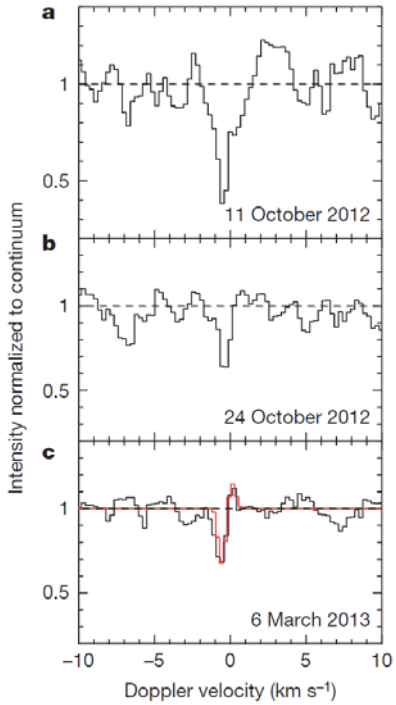

Figure 4-2 : Plots – extracted from the Nature paper - (a) through (c) show WBS spectra generated from the HIFI observations of the H2O line on the 11th October 2012, 24th October 2012 and the 8th March 2013. The x-axis shows the Doppler velocity in the Ceres frame, after correction for the relative motion between Ceres and Herschel. The spectral resolution is 1.1MHz (0.5kms21) with 0.6MHz sampling. In plot (c), the results of the simulation using the DSMC model has been superimposed (in red) on the WBS signal. This shows the excellent fit between the model and our results. It's important to flag that the water signal was shown to reduce from the initial detection to the final one in March 2013.

4.1.3 Work performed since 2014 related to our findings

Figure 4-3 below presents the search campaigns performed for water activity on Ceres. The observatories analysed at the time of our paper in 2014 (Figure 4-3 – purple box) were the International Ultraviolet Explorer (IUE), the Very Large Telescope (VLT), and Herschel. In that figure, the inner orbit is that of Earth, the outer orbit that of Ceres, rh is the heliocentric distance of Ceres and Delta is the distance between Ceres and the observer. If cometary activity was the source of water on Ceres we would expect the onset of activity to appear well before perihelion before becoming much weaker at some time after perihelion.

No activity was detected by VLT and Herschel at distances > 2.83 AU but then Herschel detected activity in all observations within 2.72 AU. The non-detection by IUE at almost the same orbital position as one of the Herschel observations three orbital periods earlier could be explained by the higher sensitivity of Herschel for near-equatorial sources.

The single observation post-perihelion (a marginal detection by IUE - A'Hearn et al. 1992) did not allow us to draw conclusions about the behaviour when Ceres was receding from the Sun. The water absorption was strongest in the first Herschel detection on 11 October 2012, well before passing perihelion which was not what we would expect for cometary activity especially as it was found to be weaker in our observations following that. Based on the activity observed and using our models, we were able to restrict the water ice to a radius of about 100km for each localised region, however, the active surface ice fraction required to produce the detection within those areas was very small (<10^{-5} of the surface area of the identified source regions) and the identification of the active regions was not unique

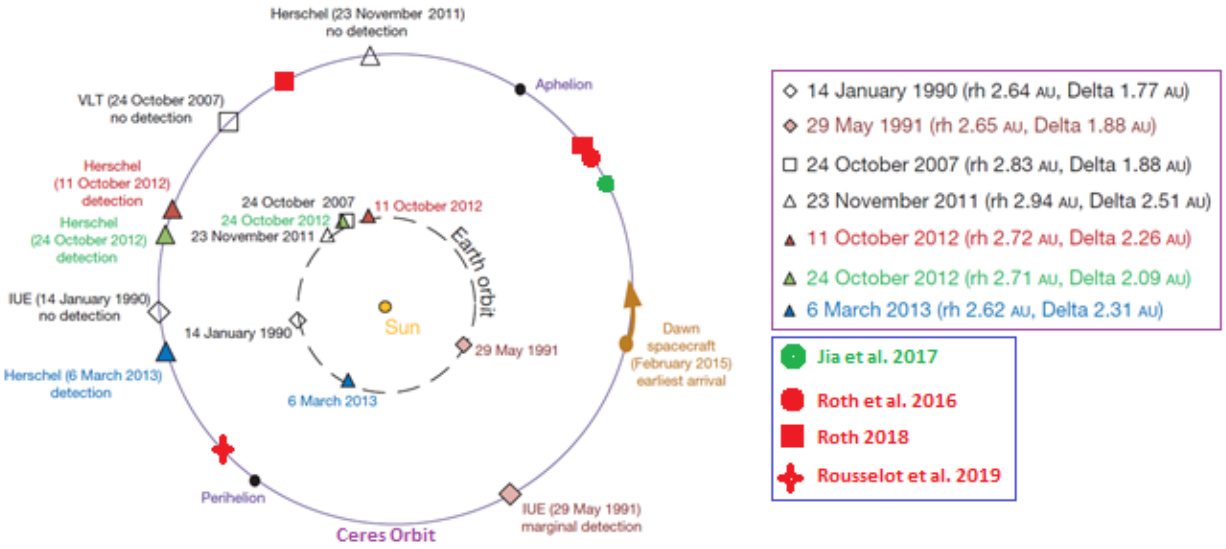

Figure 4-3: Water production of Ceres versus position in the orbit (Adapted for this thesis from Küppers & O'Rourke et al, 2014). The adaptations reflect detections (green) and non-detections (red) since 2014.

Since our paper was published in 2014, five further observations have been made of Ceres in its orbit around the sun (Figure 4-3 – blue box) with only one resulting in a detection. The new additional detection was made from the Dawn spacecraft (Jia et al. 2017) using the GRaND instrument. A measurement taken by Roth et al. (2016) using the HST/COS instrument, two measurements taken by Roth (2018) using the HST/STIS and HST/COS instruments and one measurement by Rousselot et al. (2019) were all non-detections. It's important to flag that the non-detection by Rousselot et al. (2019), which was taken just prior to perihelion provided an upper limit of 2 x 10^{26} mol. s^{-1}, equivalent to the detection made by Herschel/HIFI at a further distance from perihelion.

In our 2014 paper we provided three possible explanatory mechanisms for the production of the water exosphere from these regions. The first was cometary-type sublimation of (near) surface ice. In this case the sublimating ice drags near-surface dust with it and in this way locally removes the surface layer and exposes fresh ice. Transport from the interior is not required. The second mechanism is equivalent to the first in that it relies on sublimation of surface ice, however in this case, the existence of the water ice is as a result of exposure by an impact or landslide rather than due to the continuous exposure of an icy subsurface layer. The third mechanism we mentioned was due to surface geysers or cryovolcanoes, for which an interior heat source is needed.

With the arrival of the Dawn spacecraft at Ceres a number of months after our discovery, our results proved to be a very important input for the observation planning they planned to carry out. Over 130 bright spots were observed by Dawn on the surface of Ceres, of which nine were confirmed to be water ice patches (Combe et al. 2017). These water ice patches were calculated to produce water vapour quantities (0.16 kgs^{-1}; Landis et al. 2019) insufficient to explain the required water ice sublimation matching our Herschel HIFI result (6 kgs^{-1}). Indeed Landis et al. (2019) took into account possible ice exposed due to impact over the course of a Ceres year, finding that the value produced (0.56 $kg.s^{-1}$) was also much lower than the Herschel value.

Further to this, in Rousselot et al. (2019), a detailed analysis is performed of all previous observations (including their own; Figure 4-3) and they found that the lack of a clear correlation between Ceres' heliocentric distance and the observed water production rates did not match with a sublimation process as observed e.g. on comets, whereby the reducing distance to the sun would lead to increased sublimation taking place.

In line with our proposal that cryovolcanism might explain the observed Herschel exosphere, Ruesch et al. (2016) investigated and proposed that the ~17-km-wide and 4-km-high Ahuna Mons "mountain" observed on Ceres could be due to cryovolcanic activity by hydrated salts. This was challenged by Bland et al. (2019) suggesting that the process was due to a solid state flow process in line with terrestrial salt tectonics. However, a recent paper from De Sanctis et al. (2020) presented the discovery of hydrated sodium chloride located on the top of the Cerealia Facula Dome close to a system of radial fractures. Her results pointed to the release of salty fluids from the interior (via cyrovolcanism) as being a likely possibility even today.

One other process which has come to the fore in recent years is based on Solar Energetic Particle events (SEP). The Dawn spacecraft as it approached Ceres in June 2015 detected using the GRaND (Gamma Ray and Neutron Detector) instrument, electron beams of some tens of keV. Jia et al. (2017) found that these could be explained by fast-Fermi acceleration at a temporary bow shock which is produced when the solar wind encounters a temporary atmosphere, similar to a cometary coma. The simplest model proposed in that paper required about 1.8 kg s^{-1} or 6×10^{25} mol.s^{-1} water vapour production rate to form such a shock. Such an estimate relied on characteristics of the solar wind-Ceres interaction. This correlation between SEPs and the detections/non-detections shown in Figure 18 are discussed in more detail in Villareal et al. (2017) of which L.O'Rourke is a co-author.

While the possibility of a SEP event vaporising an optically thin layer of ice formed by condensation of water molecules around the winter pole has been proposed (Schorghofer et al. 2017), the resulting exosphere would still be insufficient to explain the Herschel observations.

In conclusion, although our paper was published in 2014, it still represents the most significant detection in use by planetary science on the presence of an exosphere around Ceres. While the merging of the above processes i.e. sublimation of a recently exposed (by impact) water ice feature, combined with sublimation from multiple water ice patches, combined with the SEP exposure of winter pole water ice coverage, can all contribute to explaining up to 50% of the 6 kgs^{-1} water vapour observed by Herschel/HIFI, it's clear that there remains a scientific question to be answered in order to explain the source of the remaining 50%. With the recent paper from De Sanctis et al. (2020) pointing to cryovolcanism as still being a valid option, this may indeed be the missing piece of the puzzle.

4.2 Determination of a water outgassing upper limit for a Main-Belt Comet

4.2.1 Motivation & Link to Objectives #1 and #2

The search for water on the surface of Main-Belt Comets (MBC) was the key motivation behind an Astrophysics Journal Letters paper (with LO'Rourke as first author) released in 2013, titled "Determination of an upper limit for the water outgassing rate of Main-Belt Comet P/2012 T1 (PANSTARRS)" (O'Rourke et al., 2013). It is attached in Annex B of this thesis.

The paper presents observations performed on Main-Belt Comet (MBC) P/2012 T1 that was discovered in October 2012. As it was discovered by the Pan-STARRS1 survey, its name is extended by "PANSTARRS". The fact that this asteroid presented comet like activity – defining it as a Main-Belt Comet – led to significant interest arising across the scientific community in attempting to understand what might be causing that activity e.g. cometary sublimation or an impact from another asteroid.

With the Herschel Space observatory still in operations at that time, the use of the HIFI instrument and its significant sensitivity to search for water vapour was considered an ideal instrument to observe this MBC and determine if indeed its activity was due to sublimation based processes. Confirming that the activity was indeed ongoing at the time of the observation was considered a must. In that respect, by confirming activity and searching for water vapour, we could bring together the cause and effect and obtain definitive proof that some Main-Belt Comets do sublimate and are indeed cometary in nature.

This MBC was found by our paper to have a diameter < 2.6km. The size of this object is highly comparable to the size range found for comets. The strong link that exists between comets and Main-Belt Comets, the techniques in use for this paper (in line with those we use in Chapter 3), the findings we made all make this an important paper to take into account in the scope of this thesis and, in particular when addressing both of the objectives of this thesis i.e. searching for and characterising surface/subsurface ice on asteroids and on comets.

4.2.2 Brief summary of Results

A request for "Director Discretionary Time" by LO'Rourke was approved to observe this MBC using the Herschel Space Observatory's HIFI instrument in January 2013 approximately 4 months after it had reached perihelion. The observation was to be performed in parallel with the use of the VLT FORS2 imager, on the basis that we could confirm that the MBC was still showing activity when we performed the HIFI spectral search for water vapour.

The line emission from the fundamental ortho-H_2O 1_{10}–1_{01} line at 556.936 GHz was searched for in the upper sideband of the HIFI band 1a mixer. The HIFI observation was carried out on the 16th January 2013

when the MBC was at an approximate heliocentric distance of 2.504 AU. The observing mode (see Figure C-7) used was the frequency-switching observing mode with a frequency throw of 94.5 MHz, using both the wide-band spectrometer (WBS) and the high-resolution spectrometer (HRS).

Contrary to the O'Rourke et al. (2020b) paper, where we used the CLASS software to perform the baseline fit; for this MBC paper, the Lomb–Scargle periodogram method (initially proposed by Lomb 1976, and further developed by Scargle 1982) was applied to the HRS and WBS spectra, fitting the baseline ripple using the strongest peaks in the frequency spectrum. The HIFI data provided sensitive 3σ upper limits 3.6 mK km/s ∫TmBdv from the mean of the HRS and WBS values.

Three 300 s V-band VLT FORS2 images were taken on the 15th January 2013, with the telescope tracking the comet's motion. At this time the comet was at 2.502 AU from the Sun. The resulting images had aperture photometry performed with the result shown below in Figure 4-4. From this observation we calculated a dust production rate of 2.7 kg s^{-1} .

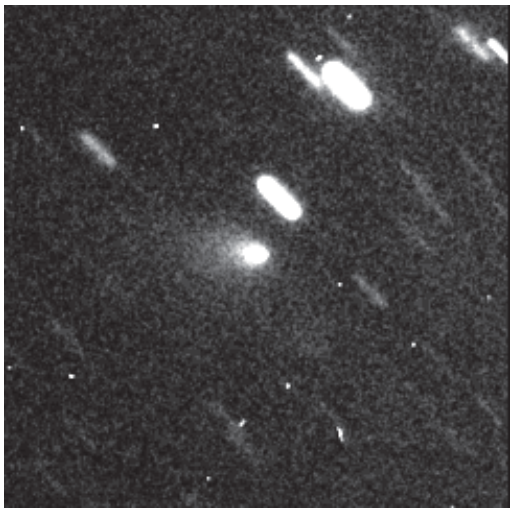

Figure 4-4: Context broad band image of the MBC on the 2013 January 15 using the VLT FORS2 detector. Image taken from O'Rourke et al. (2013a).

The same molecular excitation model as used in the paper in Chapter 3 (O'Rourke et al. 2020b) was used in this paper. We used a molecular excitation model to calculate the population of the rotational levels of water as a function of nucleocentric distance as well as to derive the production rates.

Input parameters to this model include the electron density, gas kinetic temperature, expansion velocity, and the radial gas density profile. Electron density and gas kinetic temperature profile values (extracted from Biver et al. 1997; de Val-Borro et al. 2010) were fed into the model. For the case of the kinetic temperature (used to control the molecular excitation in the collisional region), a range of values from 10 to 20 K were input. Since the electron density in the coma was not well constrained, an electron density scaling

factor of x_{ne} = 0.2 with respect to the standard profile derived from observations of comet 1P/Halley was used (e.g. Hartogh et al. 2010).

Our aim was to determine if the observed activity was indeed cometary in nature by searching for water vapour in the coma surrounding the MBC. The VLT observed the MBC on the 15th January 2013 while Herschel observed it on the 16th January 2013. It was confirmed very soon afterwards in the FORS2 images that the MBC was still active at the time of the Herschel observation.

While no H2O line emission was detected in our observations, we were able to derive sensitive 3σ upper limits for the water production rate and column density of $<7.63 \times 10^{25}$ molecules s^{-1} and of $<1.61 \times 1011$ cm^{-2}, respectively. This non-detection suggested that the ongoing sublimation due to water ice was lower than our upper limit.

Surface coverage estimate (derived for this thesis only) : Although not covered in our paper, it is useful to derive a coverage estimate for the possible ice that would be needed to produce the above water production rate (Snodgrass et al. 2017). If we assume a C-type taxonomy with a geometric albedo of 0.06 (Mainzer et al. 2011) and a phase integral of 0.3, this gives a Bond albedo for the surface of ~0.018. Taking the vapour pressure and latent heats for H_2O from Prialnik et al. (2004), bare ice would sublimate at a rate of 1.8×10^{21} molecules s^{-1} m^{-2}. An upper limit of $Q_{(H2O)} < 7.63 \times 10^{25}$ molecules s^{-1} corresponds to a bare ice patch of area $\leq 4.2 \times 10^4$ m^2. This in turn corresponds to 0.2% of surface area if the nucleus radius is 1.3 km.

4.2.3 Work performed since 2014 related to our findings

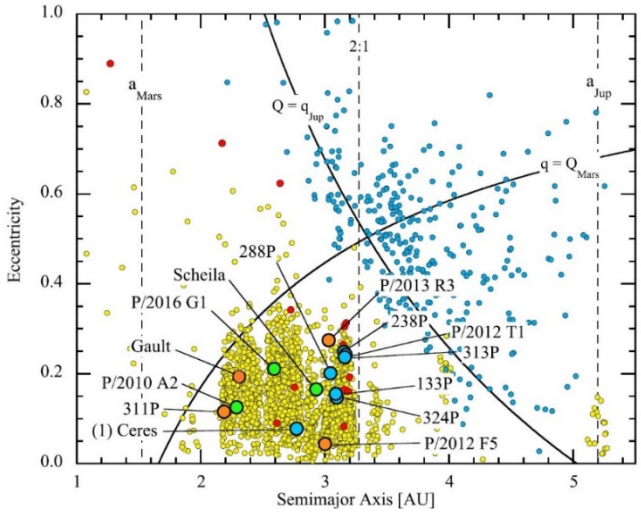

Figure 4-5: [Adapted from Jewitt et al, 2019a] : Semi major axis vs. orbital eccentricity for main belt asteroids (small yellow circles), comets (small blue circles), and active asteroids. The latter are colour coded by their suspected physical origin; ice sublimation (filled blue circles), impact debris (filled green circles), rotational breakups (filled orange circles), and other, mostly unknown origins (filled red circles). Diagonal arcs show the loci of orbits having perihelion distances equal to the aphelion distance of Mars, and aphelion distances equal to the perihelion distance of Jupiter, as marked. Vertical dashed lines indicate the semi major axes of Mars, Jupiter, and the 2:1 mean-motion resonance with Jupiter.

Figure 4-5 above provides a useful graphical view of some of the "active asteroids" that were discovered up to 2019. While not all have been named nor flagged, this figure is quite helpful in highlighting that those objects which are considered to be active due to sublimation (filled blue circles) are located in the outer part of the main belt where temperatures are lower. Those objects which show sublimatory activity fall into the realm of Main-Belt Comets.

At the time of publication of our paper, seven MBCs had been discovered, namely:

- 133P/Elst-Pizarro (1996 – year of discovery)
- 238P/Read (2005)
- 176P/LINEAR (2005)
- 259P/Garradd (2008)
- 324P/La Sagra (2010)
- 288P/2006 VW139 (2011)
- P/2012 T1 (PANSTARRS) (2012)

A study performed in September 2017 (Snodgrass et al, 2017) provides a very useful overview of the area of Main-Belt Comets. By the time of that study, five more MBCs had been identified namely:

- Ceres (2014) : based on the paper addressed in Chapter 4 and in Annex A from Küppers & O'Rourke et al. (2014).
- P/2013 R3 (Catalina-PANSTARRS) (2013)
- 313P/Gibbs (2014)
- P/2015 X6 (PANSTARRS) (2015)
- P/2016 J1-A/B (PANSTARRS) (2016)

In the study from Snodgrass et al. (2017) above, they reviewed the progress made in the first decade investigating all 12 objects above, addressing aspects such as the observations performed, modelling carried out of ice survival, as well as providing a discussion on their origins. While progress was noted across all areas (in line with progress made in the asteroid & cometary fields), the key point flagged was the difficulty in identifying sublimation as the source of the activity on these MBCs. While identification based on dust modelling results, confirmation of recurrent activity, or both represent the standard way, they flagged the importance of direct detection of (escaping) water in these bodies. Our paper was therefore highlighted in this study a number of times due to the direct detection performed using the Herschel HIFI instrument. This method was deemed to be the most reliable as it was determined that for the majority of all other MBCs, the upper limits on water production all relied on the assumption that MBCs have a similar water/CN ratio to other comets, which was deemed to be unlikely to be the case.

Finally they reviewed observatories to be built or launched to determine whether observations to the level of sensitivity observed by Herschel could be carried out. They flagged in particular the importance of JWST in this regards.

Since that review, only one new MBC has been discovered - P/2017 S5 (ATLAS) - in 2017 (Jewitt et al. 2019b). With only 14 MBCs now known, questions are being asked as to the reasoning for why so few are being discovered especially taking into account the extensive asteroidal survey campaigns that are being run across multiple observatories. Hsieh et al. (2018) has found links between the MBCs and the existing asteroid families which are groups of asteroids with similar orbital elements that have been inferred to have formed from the catastrophic fragmentation of single parent bodies at some point in the past (Hirayama 1918). Indeed, Main-Belt Comets 133P/Elst-Pizarro, 176P/LINEAR, 288P/(300163) 2006 VW139, 238P/Read, are all considered to be members of the ∼2.5 Gyr old Themis family (Nesvorný et al. 2003), whose largest member (24) Themis has been investigated in this thesis for sublimation (see Chapter 3).

This link between asteroid families and MBCs is proposed by Hsieh et al. (2018) as being a possible reason as to why they exist in the first place. In his paper, he describes a sequence of processes whereby ice is preserved over gigayear timescales in the large parent bodies. These are then catastrophically disrupted in family-forming collisions leading to the “younger” family members possessing subsurface ice at relatively shallow depths making them more susceptible to activation than older icy asteroids.

Finally, many carbonaceous meteorites (e.g. the CM chondrites) contain hydrated minerals like carbonates and serpentine; indeed even grains of salt have been found on them. Further to this, a recent study by Piani et al. (2020) points to enstatite meteorites having enough water to provide Earth with the mass equivalent of several surface oceans’ worth of water. The Main-Belt Comets may be closely related to these hydrated bodies, except that their ice survived primarily because the temperatures never reached sublimation point.

Chapter 5

Key Results, Conclusions and Future Work

5.1 Key Results & Conclusions

This thesis had as its main goal to search for the presence of ice (primarily water ice) existing on and just below the surfaces of both comets and asteroid, estimate its coverage and where feasible characterise its properties e.g. look at subsurface dynamics in play to release water ice to the surface. Our search included the application of a range of different search techniques as outlined in chapter 1. The above goal was broken into two objectives linked to two main thesis papers complemented by two supporting papers.

The first objective focussed on the search for and characterisation of surface/subsurface ice on comets. To address this objective, our first main paper focussed the search on one specific comet - 67P/Churyumov-Gerasimenko - whereby we used multi-wavelength observations merged with in-situ measurements to successfully identify the ice and to characterise its physical and scientific properties. We also presented a supporting paper which searched for the presence of water ice on a Main-Belt Comet. In line with techniques applied on comets, we looked for and confirmed the presence of a dust coma around the MBC. While not obtaining a detection to confirm sublimation as being the reason for this activity, we did define a very sensitive upper limit on the sublimation rate. Furthermore using photometry techniques we estimated the dust production rate as well as provided an upper limit estimate on the MBC size of 2.6 km.

The second objective focussed on the search for and characterisation of surface/subsurface ice on asteroids. To address this objective, our main paper was based on the study of two of the largest asteroids in the asteroid belt whereby (24) Themis has a size of 192 km and (65) Cybele has a size of 282 km. Using HIFI data where upper limits for the sublimation rate were estimated, we combined these with multi-wavelength datasets to derive their thermophysical properties and use these properties to determine the surface coverage of water ice feasible to produce the upper limit we measured.

We complemented our findings in this main asteroid paper with two supporting papers (published prior to this thesis). The first supporting paper searched for water ice on the largest object in the asteroid belt (1) Ceres where we confirmed the existence of an exosphere and speculated (it turns out now, correctly) on the processes needed to produce it. The second supporting paper was mentioned above as it supports also the first objective. As it is an asteroid which presents cometary activity (MBC), we searched for water ice through the presence of an exosphere. While not obtaining a detection, we did define a very sensitive upper limit on the sublimation rate.

The key results (as well as main implications) from the two main papers and as such, for this thesis, can be summarised as follows:

- We have confirmed the presence of primitive ice inside cometary boulders, lying just below the dusty surface.
- We have determined the softness (compressive strength) of primitive ice on a comet via in-situ methods.
- We have found a porosity inside cometary boulders to be in line with that of the comet interior.
- We have found a low dust-to-ice ratio in line with recently exposed ice observed after an outburst
- We have derived sensitive 3σ water production rate upper limits for two of the biggest asteroids in the asteroid belt (one to two orders of magnitudes better than previous publications).
- We have found that the detection technique using an absorption feature at 3.1 μm, commonly used in the identification of water ice on the surface of asteroids, was not valid. This disproves the results of a Nature paper (Campins et al. 2010). It is clear that if there is water ice present then it is sufficiently deep below the surface that it is not sublimating.
- The % of surface coverage of water ice very much depends on how the ice is mixed with the dust. If we assume it is an intimate mixture then we get a coverage < 0.0017% for Themis, < 0.0033% for Cybele. If we compare these values to those obtained from 67P/Churyumov–Gerasimenko where the ice was also intimately mixed with the dust, an ice coverage of 0.6% at 3 au pre-perihelion and 0.2% at 3 au post-perihelion, was obtained, two orders of magnitude higher thus pointing to the surface coverage of water ice on these asteroids to be very very low.
- We find that, while water ice is generally exposed on comets through thermally induced fractures breaking open the dust covered exterior leading to outbursts and jets, in our case the ice was exposed by movements of the Philae lander itself during its bounce across the surface. Ice on the comet in general has been found to be visible in localized regions only, with the majority of the comet covered by a dust layer.
- For the case of asteroids, various scenarios exist as to how the water ice can be exposed to the sun. Where water ice is continuously present on their surface then as the asteroid comes close to perihelion, sublimation takes place. Direct detection of this sublimated water ice is very difficult to achieve though (as we have seen ourselves) due to the low surface coverage of the ice. In the case where the water ice is buried below the surface then it is only exposed in the event of a surface disruption occurring e.g. due to impact or due to rotational spin-up effects (Yorp affect). In this case, the sudden exposure of water ice may lead to cometary activity being observed as in the case of the Main-Belt Comets. Even so, where activity is confirmed to be present, the detection of an exosphere has proved to be elusive as we found in our MBC supporting paper.

In the case of the supporting papers presented in this thesis:

- We have provided the first detection of water ice in the asteroid belt on the largest object (the dwarf planet (1) Ceres) and proposed it originated from either sublimation of ice from localised positions on the

surfaces or indeed due to the presence of cryovolcanoes. With all other Dwarf Planets lying in the Trans-Neptunian region where icy bodies are believed to be present, our finding of ice on this object provides a unique basis for the study of ice on these objects. The ice coverage on this body was estimated to be 2 x 10^{-7} of the surface area.

- The existence of a reservoir of water ice below the surface of Ceres has been proposed by multiple publications. Our study of Dwarf Planet (1) Ceres does appear to suggest that cryovolcanism may be a valid process for this reservoir to be tapped into.
- We have derived sensitive upper limits for the water production rate from an active Main-Belt Comet. The MBC was confirmed to be active but our results point to the water ice coverage needed to produce that activity as not being sufficient to allow detection. We derive an upper limit for the water ice surface coverage on the MBC to be <0.2%.

In general:

- We have demonstrated the significant benefits of combining in-situ and remote based observation campaigns; whether it is from a satellite orbiting a comet working with a probe on its surface, or observations performed from the Earth in support of the satellite or the lander, it is clear that each different result helps to resolve a small piece of the puzzle.
- We have demonstrated the joint benefits of merging the use of space-based observations and ground based observations whereby we searched for water vapour while using a ground observatory to confirm the target was active.
- We have demonstrated the benefits of studying asteroids and comets using multi-wavelengths and different types of telescopes be they on ground or in space combined with engineering and scientific techniques.

5.2 Future work

Making use of new ground based and space based observatories

The search to understand the comet/asteroid ice continuum will continue well into the future primarily because while we may be able to understand better a few more asteroids (through flybys of spacecraft), they are always going to be a select few among millions – of all sizes. In that respect, there will be a need to benefit from new ground based telescopes being constructed which can provide sensitivities in measurements not seen up to now; a case in point will be James Webb telescope, or indeed observatories expected to cover the 0.7 to 3μm regions

Finding new techniques to identify surface/subsurface water ice on comets and asteroids

In this thesis, we present the different techniques in use to discover water ice on or below the surface of comets and asteroids. Indeed, we have shown the difficulty of uniquely identifying water ice from single near-infrared lines. It is clear that new techniques will need to be identified and applied to help confirm the presence of water ice (be it via sublimation from below or on the surface itself) for different sizes of objects.

Merging multi-wavelength data from ground based and space based observatories

It becomes clear (especially in this thesis) that using data from different sources can help understand what is happening on these objects and indeed what is being seen in the data itself. The benefits of the internet, large data processing capabilities, improved modelling techniques and cloud technologies (whereby significant benefits can be made in the use of greater processing power & storage capabilities present 'in the cloud" that go beyond what is available locally to the scientist) are making this capability a reality. The benefits and the results will be significant.

Some specific future work linked to the four papers presented

- Ice in a cometary boulder: the discovery of soft ice just below the surface of a cometary boulder is a game changer when it comes to preparing future missions wishing to land and excavate a comet. The knowledge of the materials on and below the surface helps the mission design significantly. The "Ambition" mission which is a mission under study by ESA at present (white paper has been produced) can use our results in its investigative preparational phase.
- Reprocessing the Ceres HIFI data: The author of this thesis will be doing a full reprocessing of the Ceres HIFI data (based on latest pipeline/calibration) as part of a NASA DDAP proposal that has been accepted.
- Understanding the polarisation result found by HIFI on Ceres: An unexpected aspect of the Ceres data was that the H_2O absorption line appeared to be strongly polarized in October 2012 ($V/H = 0.40 \pm 0.12$, 0.38 ± 0.13 for 11 and 24 October, respectively) whereas no significant polarization was seen in March

2013 (V/H = 0.74 ± 0.20). This is an area which seems to have fallen between the cracks but an investigation should be carried out (envisaged to review this in the DDAP proposal) to try to get a clearer understanding on what might have caused the polarisation effect found by Ceres

- Investigating the implications of SEP events on asteroids: The presence of an exosphere around Ceres has been proposed to be (partially) the result of a SEP event measured when Dawn was at the Dwarf Planet. This link between SEP events, exosphere and surface/subsurface water ice could prove to be another method to search for water ice on asteroids.
- The search for water ice on Main-Belt comets: It's clear that this is an area which will continue for many years to come as more MBCs are discovered and found to be active. The dust produced allows an estimate to be made of the gas needed to produce it, the fact that the dust is produced below 3AU and that a dust trail is observed: all of these point to sublimation based effects. The key now is to find a way to clearly demonstrate this taking into account the existing ground and space based observatories limitations in that regard. Of note is the ZhengHe satellite mission under study by the Chinese academy of Space technology (Zhang et al. 2019) which proposes to rendezvous with MBC 133P/Elst-Pizarro in 2029/2030.
- Search for water on the Dwarf planets: Although only touched on briefly in this thesis, our finding of water ice on Dwarf Planet (1) Ceres can be used as a basis for follow-up in research on objects located in the Trans-Neptunian region. While water ice has been proposed to exist also on other Dwarf Planets e.g. Haumea (Dumas et al. 2011), a more comprehensive survey of these objects would be noteworthy to carry out.

Annex A

Localised sources of water vapour on the dwarf planet (1) Ceres

This chapter is linked to the second of the objectives of the thesis whereby we search for and characterise ice found on the surface and subsurface of asteroids. The article covered in this chapter "Localized sources of water vapour on the dwarf planet (1) Ceres", was published in Nature on January 23rd 2014. In the bibliography, it is referenced as Küppers & O'Rourke et al., 2014. While the main paper of this thesis (presented in chapter 3) studies the case for two of the larger asteroids in the main belt namely (24) Themis and (65) Cybele, this is a supporting paper that covers the largest asteroid – Dwarf planet (1) Ceres.

This paper presents observations of this asteroid performed by the Herschel Space Observatories HIFI instrument initially as part of a Guaranteed Time proposal (PI : LO'Rourke). The instrument was used to search for water vapour in the atmosphere on the asteroid based on common hypothesises pointing to Ceres being differentiated into a silicate core with an icy mantle. At the time of this Nature paper's release, there had been no water ice discovered in the asteroid belt thus its release had a significant impact in the area of planetary science.

With HIFI we detected water vapour with at least 10^{26} molecules being produced per second, originating from localized sources that appeared to be linked to mid-latitude regions on the surface. The water evaporation was considered to be possibly due to comet-like sublimation or to cryovolcanism, in which volcanoes erupt volatiles such as water instead of molten rocks. A study is presented in Chapter 4.1 which covers the scientific progress achieved in this area since we published our paper.

LETTER

doi:10.1038/nature12918

Localized sources of water vapour on the dwarf planet (1) Ceres

Michael Küppers[1], Laurence O'Rourke[1], Dominique Bockelée-Morvan[2], Vladimir Zakharov[2], Seungwon Lee[3], Paul von Allmen[3], Benoît Carry[1,4], David Teyssier[1], Anthony Marston[1], Thomas Müller[5], Jacques Crovisier[2], M. Antonietta Barucci[2] & Raphael Moreno[2]

The 'snowline' conventionally divides Solar System objects into dry bodies, ranging out to the main asteroid belt, and icy bodies beyond the belt. Models suggest that some of the icy bodies may have migrated into the asteroid belt[1]. Recent observations indicate the presence of water ice on the surface of some asteroids[2–4], with sublimation[5] a potential reason for the dust activity observed on others. Hydrated minerals have been found[6–8] on the surface of the largest object in the asteroid belt, the dwarf planet (1) Ceres, which is thought to be differentiated into a silicate core with an icy mantle[9–11]. The presence of water vapour around Ceres was suggested by a marginal detection of the photodissociation product of water, hydroxyl (ref. 12), but could not be confirmed by later, more sensitive observations[13]. Here we report the detection of water vapour around Ceres, with at least 10^{26} molecules being produced per second, originating from localized sources that seem to be linked to mid-latitude regions on the surface[14,15]. The water evaporation could be due to comet-like sublimation or to cryo-volcanism, in which volcanoes erupt volatiles such as water instead of molten rocks.

We observed Ceres with the Heterodyne Instrument for the Far Infrared (HIFI)[16] on the European Space Agency's Herschel Space Observatory[17] on four occasions between November 2011 and March 2013 (Extended Data Table 1) as part of the MACH-11 ('Measurements of 11 asteroids and comets with Herschel') guaranteed time programme (principal investigator L.O'R.) and of a follow-up Director's Discretionary Time Program. We used HIFI to search for water vapour directly, because it is more sensitive to water concentrated in the near-Ceres environment than previous instruments used to search for hydroxyl (OH). We observed the water ground-state line at a frequency of 556.936 GHz. The angular diameter of Ceres was <1 arcsec for all observations, compared to the beam width of HIFI, which was approximately 40 arcsec at the frequency of the water line. Although we cannot resolve Ceres spatially, we can derive information about the longitudinal distribution of the water sources on the surface from the variation of the absorption over the rotation of Ceres. Details of observations and data reduction are provided in the Supplementary Information and in Extended Data Table 1.

Figure 1 shows time-averaged spectra taken in October 2012 and on 6 March 2013, normalized to the thermal continuum of Ceres (measured with the expected brightness, see Extended Data Table 2). At the frequency of the water line, absorption in the thermal continuum of Ceres is clearly visible in the late 2012 observations, whereas in the 2013 data it is next to a weaker emission line detected at the 3σ level. The low outflow velocity (0.3–0.7 km s^{-1}) determined from the offset of the absorption line is comparable to the escape velocity of Ceres (about 0.52 km s^{-1}; ref. 18), showing that a fraction of the evaporated water does not escape from Ceres. For line strengths and offset information, see Extended Data Table 3.

The strength of the absorption is variable on short timescales (hours; Fig. 2) as well as on longer timescales (weeks and months; Extended Data Fig. 1 and Extended Data Table 3). We interpret the short-term variation in terms of localized sources on Ceres rotating into and out of the hemisphere visible by Herschel. Figure 2 shows the correlation of the strength of the absorption line with the position of features on the

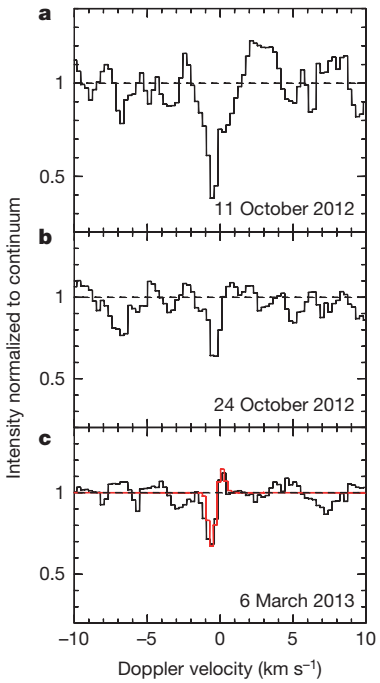

Figure 1 | Submillimetre water absorption line from the dwarf planet (1) Ceres. The spectra of the ground-state transition line 1_{10}–1_{01} of ortho-water at 556.939 GHz were obtained on 11.83–11.92 October 2012 UT (**a**), 24.84–24.96 October 2012 UT (**b**) and 6.13–6.55 March 2013 UT (**c**), with HIFI's Wide-Band Spectrometer. The spectra, which are the averages of the linear H and V polarizations, were divided by the Ceres continuum thermal emission. The abscissa represents the Doppler velocity in the Ceres frame, after correction for the relative motion between Ceres and Herschel. The spectral resolution is 1.1 MHz (0.5 km s^{-1}) with 0.6 MHz sampling. The water line is seen in absorption against the thermal emission of Ceres. Material moving towards the observer causes the absorption line to be blue-shifted. In the 6 March spectrum (**c**), a redshifted emission line is visible next to the blue-shifted absorption line, showing that the exosphere of Ceres extends towards the limbs. The possible polarization of this line is discussed in the Supplementary Information. Overplotted on the 6 March spectrum is a model of the spectrum of the water line for two active spots 60 km in diameter situated on the surface of Ceres (red spectrum in **c**). The simulation takes into account the variation of the sub-observer point longitude during the 10-hour-long observation. The model spectrum is adjusted to the depth of the observed spectrum. The relative strengths of the redshifted and blue-shifted peaks are correctly reproduced.

[1]European Space Agency, European Space Astronomy Centre, PO Box 78, Villanueva de la Cañada 28691, Spain. [2]Laboratoire d'études spatiales et d'instrumentation en astrophysique, Observatoire de Paris, CNRS, Université Pierre et Marie Curie (UPMC), Université Paris-Diderot, 5 Place Jules Janssen, 92195 Meudon, France. [3]Jet Propulsion Laboratory, Pasadena, 4800 Oak Grove Drive, La Cañada Flintridge, California 91011, USA. [4]Institut de Mécanique Céleste et de Calcul des Éphémérides, Observatoire de Paris, Unité Mixte de Recherche (UMR) 8028. CNRS, 77 Avenue Denfert Rochereau, 75014 Paris, France. [5]Max-Planck-Institut für extraterrestrische Physik (MPE), Giessenbachstrasse 1, 85748 Garching, Germany.

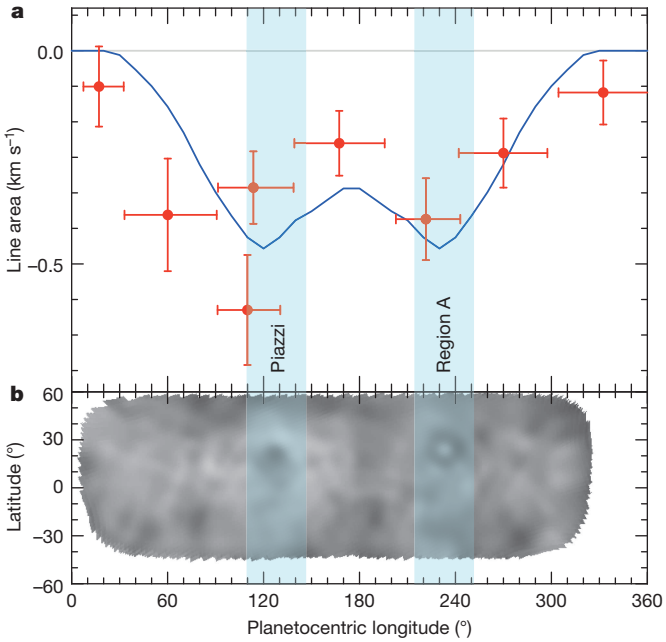

Figure 2 | Variability of water absorption on 6 March 2013. **a**, Line area of the water absorption line (normalized to the continuum emission of Ceres) at 557 GHz as a function of the longitude of the sub-observer point. Measurements are shown as red dots; error bars on the intensity are 1σ and the horizontal bars show the range of sub-observer longitudes covered by individual measurements. The two conflicting data points at sub-observer point longitude $\Lambda \approx 110^\circ$ were taken within a time interval of 9 hours (corresponding to the rotation period of Ceres), and suggest temporal variability at the regional scale. Vertical bands indicate the planetocentric longitude of the dark regions: Piazzi (longitude, 123°, latitude +21°) and Region A (longitude 231°, latitude +23°)[14,15,19]. The curve in blue is the result of a gas-kinetic model of the exosphere of Ceres[21] (see Supplementary Information). Water is released from localized sources 60 km in diameter situated at the longitudes and latitudes of regions Piazzi and Region A, with a total production rate of 10^{26} molecules per second for each source. The surface temperature of Ceres varies from 235 K (subsolar, that is, when the Sun is at zenith) to 168 K (morning and evening). The excitation and radiative transfer models of the water 1_{10}–1_{01} line include excitation of the vibrational bands by the Sun's infrared radiation, excitation of the rotational lines by thermal radiation from Ceres, collisions with water and self-absorption effects[22] (see Supplementary Information). **b**, A map of Ceres from near-infrared adaptive-optics imaging observations[14]. Piazzi and Region A are seen as dark regions, with a bright centre within Region A.

Ceres surface that are known from ground-based[14,15] and Hubble Space Telescope[19] observations. In all observations that detected water vapour from Ceres, the absorption line strength is strongly correlated with the visibility of surface areas identified as dark regions (about 5% darker than the average surface) in near-infrared observations. We identify those regions as the likely source of most of the evaporating water. A bright region known from observations in the visible region of the spectrum does not appear to contribute. Possibly, the dark regions are warmer than the average surface, resulting in efficient sublimation of small water-ice reservoirs.

Although the small number of observations does not allow a unique interpretation of the long-term variation, the lack of detection of the water line at 2.94 astronomical units (AU; where 1 AU is the mean distance from Earth to the Sun) in November 2011 and its first detection at 2.72 AU are consistent with the steep increase of water-ice sublimation between 3 AU and 2.5 AU (ref. 20). In addition, the larger absorption strength on 11 October 2012 compared to the observations two weeks later and five months later suggests sporadic changes in the water evaporation. Given that the spin axis of Ceres is nearly perpendicular to its orbital plane[14], we expect seasonal variations driven by spin-axis obliquity to contribute little to the variability.

We analysed the water exosphere of Ceres with a gas kinetic Direct Simulation Monte Carlo[21] model (Extended Data Fig. 2) that considers water vapour to be ejected from localized sources, and then to slow down in Ceres' gravity field. To simulate water spectra, we use a state-of-the-art two-dimensional excitation model[22], which considers excitation by radiation from Ceres and the Sun and collisional excitation (see details in Supplementary Information). The temporal variation of the absorption line observed on 6 March 2013 is well described by a model that considers outgassing from two sources coincident with dark regions Piazzi and Region A (Fig. 2). Modelling predicts line emission at positive velocities (Fig. 1), caused by gas expansion from dense to more rarefied regions. The resulting total production rate of about 2×10^{26} molecules (or 6 kg) per second of water requires only a tiny fraction of the Ceres surface to be covered by water ice. The surface of Ceres receives on average a solar input power of approximately 50 W m^{-2} (a quarter of the total solar power at the heliocentric distance of Ceres, with the factor 1/4 being the ratio between the cross-section of Ceres and its surface area). Because Ceres is located in the transition range between the outer Solar System, where most of the solar energy will be re-emitted as thermal radiation, and the inner Solar System, where most of the energy will go into sublimation of the ice, we assume that half of the energy will be used for sublimation. With a latent heat of sublimation of 2.5×10^6 J kg^{-1}, the corresponding sublimation rate is 10^{-5} kg m^{-2} s^{-1}. To sublimate 6 kg s^{-1} of water ice, Ceres must have a surface area covered with water ice of 0.6 km^2, or approximately 10^{-7} of its total surface area. If the activity is restricted to areas with a radius of about 100 km (the approximate size of the identified source regions), the active surface fraction required within those areas is still very small ($<10^{-5}$ of the surface area of the identified source regions).

An unexpected aspect of the data is that the absorption line appears to be strongly linearly polarized in October 2012, whereas no significant polarization was seen in March 2013. See Extended Data Table 3, Extended Data Fig. 3, and Supplementary Information for further analysis.

The measured water production is two orders of magnitudes higher than is predicted from a model of sublimation maintained from water supplied from the interior of Ceres[23]. In addition, the water activity is most probably not concentrated on polar regions, where water ice would be most stable. We propose two mechanisms for maintaining the observed water production on Ceres. The first is cometary-type sublimation of (near) surface ice. In this case the sublimating ice drags near-surface dust with it and in this way locally removes the surface layer and exposes fresh ice. Transport from the interior is not required. The second mechanism is geysers or cryovolcanoes, for which an interior heat source is needed. For Jupiter's satellite Io and Saturn's moon Enceladus the source of activity is dissipation of tidal forces from the planet[24,25]. That can be excluded for Ceres, but some models suggest that a warm layer in the interior heated by long-lived radioisotopes may maintain cryovolcanism on Ceres at the present time (ref. 26 and references therein).

One way of distinguishing between the two mechanisms is to analyse the variation of the water activity of Ceres over its orbit. Taking the activity of main-belt comets as a reference, cometary activity is expected to be concentrated at the perihelion passage[5]. On the other hand, cryovolcanism receives its energy from the interior and so no dependence on heliocentric distance would be seen, although sporadic variations of activity are likely. The currently available data appear to be consistent with the cometary hypothesis, but more observations are needed to distinguish between these possibilities (see Fig. 3).

Although ground- and space-based observations may further map the behaviour of Ceres over its orbit, the Dawn spacecraft mission[27] arriving to orbit Ceres in early 2015 is expected to be key in providing a long-term follow-up on the water outgassing behaviour of Ceres. In particular, it will provide long-term monitoring of the water outgassing concentration and stability of the activity in the dark regions where we suggest that the water-ice mantle of Ceres may reach the surface. Two of the instruments on Dawn—the near-infrared spectrometer (VIR)

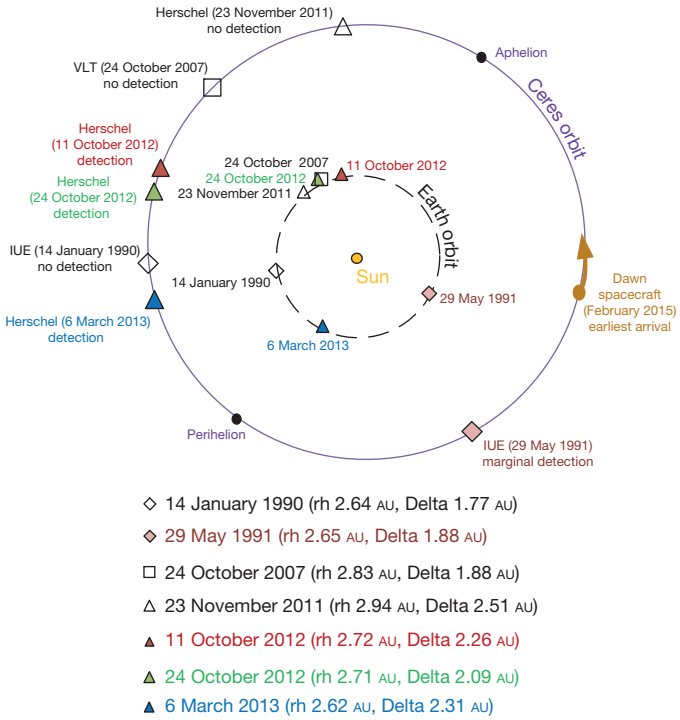

Figure 3 | Water production of Ceres versus position on its orbit. Searches for water activity on Ceres were performed with the International Ultraviolet Explorer (IUE), the Very Large Telescope (VLT), and Herschel. The inner orbit is that of Earth, the outer orbit that of Ceres. rh is the heliocentric distance of Ceres and Delta is the distance between Ceres and the observer. If cometary activity is the source of water on Ceres we would expect the onset of activity to appear well before perihelion before becoming much weaker at some time after perihelion. The pre-perihelion data are consistent with that picture. No activity was detected by VLT and Herschel at less than 2.83 AU; then Herschel detected activity in all observations within 2.72 AU. The non-detection by IUE at almost the same orbital position as one of the Herschel observations three orbital periods earlier can be explained by the higher sensitivity of Herschel for near-equatorial sources. The single observation postperihelion (a marginal detection by IUE) does not allow us to draw conclusions about the behaviour when Ceres is receding from the Sun. Dawn will visit Ceres on the postperihelion arc. The water absorption was strongest in the first Herschel detection on 11 October 2012, well before passing perihelion. To first order this is not what we would expect for cometary activity. It may have been caused by an analogue of a cometary outburst. Alternatively, it could have been a volcanic eruption. In that case, the correlation of the detectability with heliocentric distance may be coincidental. Additional observations are required to distinguish better between different mechanisms for the water activity.

and the gamma ray and neutron detector (GRaND)—may contribute significantly to this task. Although no observations of water are available for the orbital position of Ceres at the time of its arrival (Fig. 3) and the heliocentric distances in the spacecraft's initial few months around Dawn of 2.85–2.95 AU appear to be unfavourable for detecting activity, it may be that the post-perihelion activity is maintained to larger distances.

The identification of more than one water source on Ceres suggests outgassing from a small ice fraction near the surface as opposed to sporadic activity triggered by a singular event like a recent large impact. This supports the idea that Ceres possesses an icy mantle, and it also implies that we have detected water activity in the asteroid main belt. If the water is from cometary sublimation, it demonstrates that activity driven by water sublimation is not limited to classical comets, but is present in the asteroid belt as well. This supports the new vision of our Solar System with a continuum in composition and ice content between asteroid and comet populations[28].

Online Content Any additional Methods, Extended Data display items and Source Data are available in the online version of the paper; references unique to these sections appear only in the online paper.

Received 23 August; accepted 26 November 2013.

1. Walsh, K. J., Morbidelli, A., Raymond, S. N., O'Brien, D. P. & Mandell, A. M. A low mass for Mars from Jupiter's early gas-driven migration. *Nature* **475,** 206–209 (2011).
2. Campins, H. *et al.* Water ice and organics on the surface of the asteroid 24 Themis. *Nature* **464,** 1320–1321 (2010).
3. Rivkin, A. S. & Emery, J. P. Detection of ice and organics on an asteroidal surface. *Nature* **464,** 1322–1323 (2010).
4. Licandro, J. *et al.* (65) Cybele: detection of small silicate grains, water-ice, and organics. *Astron. Astrophys.* **525,** A34 (2011).
5. Jewitt, D. The active asteroids. *Astron. J.* **143,** 66 (2012).
6. Lebofsky, L. A., Feierberg, M. A., Tokunaga, A. T., Larson, H. P. & Johnson, J. R. The 1.7- to 4.2-micron spectrum of asteroid 1 Ceres: evidence for structural water in clay minerals. *Icarus* **48,** 453–459 (1981).
7. King, T. V. V., Clark, R. N., Calvin, W. M., Sherman, D. M. & Brown, R. H. Evidence for ammonium-bearing minerals on Ceres. *Science* **255,** 1551–1553 (1992).
8. Milliken, R. E. & Rivkin, A. S. Brucite and carbonate assemblages from altered olivine-rich materials on Ceres. *Nature Geosci.* **2,** 258–261 (2009).
9. Thomas, P. C. *et al.* Differentiation of the asteroid Ceres as revealed by its shape. *Nature* **437,** 224–226 (2005).
10. McCord, T. B. & Sotin, C. Ceres: evolution and current state. *J. Geophys. Res.* **110,** E05009 (2005).
11. Castillo-Rogez, J. C. & McCord, T. B. Ceres' evolution and present state constrained by shape data. *Icarus* **205,** 443–459 (2010).
12. A'Hearn, M. F. & Feldman, P. D. Water vaporization on Ceres. *Icarus* **98,** 54–60 (1992).
13. Rousselot, P. *et al.* A search for water vaporization on Ceres. *Astron. J.* **142,** 125 (2011).
14. Carry, B. *et al.* Near-infrared mapping and physical properties of the dwarf-planet Ceres. *Astron. Astrophys.* **478,** 235–244 (2008).
15. Carry, B. *et al.* The remarkable surface homogeneity of the Dawn mission target (1) Ceres. *Icarus* **217,** 20–26 (2012).
16. de Graauw, Th *et al.* The Herschel-Heterodyne Instrument for the Far-Infrared (HIFI). *Astron. Astrophys.* **518,** L6 (2010).
17. Pilbratt, G. L. *et al.* Herschel Space Observatory. An ESA facility for far-infrared and submillimetre astronomy. *Astron. Astrophys.* **518,** L1 (2010).
18. Carry, B. Density of asteroids. *Planet. Space Sci.* **73,** 98–118 (2012).
19. Li, J.-Y. *et al.* Photometric analysis of 1 Ceres and surface mapping from HST observations. *Icarus* **182,** 143–160 (2006).
20. Biver, N. *et al.* The 1995–2002 long-term monitoring of comet C/1995 O1 (Hale–Bopp) at radio wavelength. *Earth Moon Planets* **90,** 5–14 (2002).
21. Crifo, J. F., Loukianov, G. A., Rodionov, A. V. & Zakharov, V. V. Comparison between Navier–Stokes and direct Monte-Carlo simulations of the circumnuclear coma I. Homogeneous, spherical sources. *Icarus* **156,** 249–268 (2002).
22. Zakharov, V., Bockelée-Morvan, D., Biver, N., Crovisier, J. & Lecacheux, A. Radiative transfer simulation of water rotational excitation in comets. Comparison of the Monte Carlo and escape probability methods. *Astron. Astrophys.* **473,** 303–310 (2007).
23. Fanale, F. P. & Salvail, J. R. The water regime of asteroid (1) Ceres. *Icarus* **82,** 97–110 (1989).
24. Peale, S. J., Cassen, P. & Reynolds, R. T. Melting of Io by tidal dissipation. *Science* **203,** 892–894 (1979).
25. Howett, C. J. A., Spencer, J. R., Pearl, J. & Segura, M. High heat flow from Enceladus' south polar region measured using 10–600 cm-1 Cassini/CIRS data. *J. Geophys. Res.* **116,** E03003 (2011).
26. McCord, T. B., Castillo-Rogez, J. & Rivkin, A. Ceres: its origin, evolution and structure and *Dawn's* potential contribution. *Space Sci. Rev.* **163,** 63–76 (2011).
27. Russell, C. T. & Raymond, C. A. The Dawn mission to Vesta and Ceres. *Space Sci. Rev.* **163,** 3–23 (2011).
28. Gounelle, M. *et al.* in *The Solar System Beyond Neptune* (eds Barucci, M. A., Boehnhardt, H., Cruikshank, D. P. & Morbidelli, A.) 525–541 (Univ. Arizona Press, 2008).

Supplementary Information is available in the online version of the paper.

Acknowledgements Herschel is an ESA space observatory with science instruments provided by European-led principal investigator consortia and with important participation by NASA. The HIFI was designed and built by a consortium of institutes and university departments from across Europe, Canada and the United States under the leadership of SRON, the Netherlands Institute for Space Research, and with major contributions from Germany, France and the USA. This development was supported by national funding agencies: CEA, CNES, CNRS (France); ASI (Italy); and DLR (Germany). Additional funding support for some instrument activities was provided by the ESA. We thank the team at the Herschel Science Centre for their flexibility in scheduling the observations. We thank the Herschel Project Scientist and the Time Allocation Committee for the allocation of Director Discretionary Time. B.C. acknowledges support from the faculty of the European Space Astronomy Centre (ESAC). We thank A. Pollock for proofreading the final text.

Author Contributions M.K. proposed the observations of Ceres with HIFI as part of L.O'R.'s MACH-11 Guaranteed Time Program. M.K., L.O'R., D.B.-M., B.C., D.T. and A.M. planned the observations. M.K., D.B.-M., B.C., D.T., R.M. and J.C. contributed to the data analysis. The modelling was performed by D.B.-M., V.Z., S.L., P.v.A. and T.M. The manuscript was written by M.K., L.O'R., D.B.-M., B.C. and M.A.B. All authors discussed the results and reviewed the manuscript.

Author Information Reprints and permissions information is available at www.nature.com/reprints. The authors declare no competing financial interests. Readers are welcome to comment on the online version of the paper. Correspondence and requests for materials should be addressed to M.K. (michael.kueppers@sciops.esa.int).

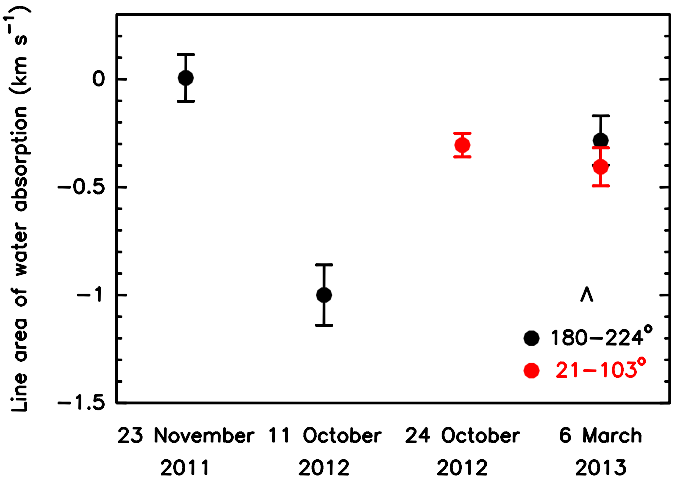

Extended Data Figure 1 | Long-term variability of water absorption. The absolute value of the area of the water absorption line at 557 GHz (line area normalized to Ceres continuum emission) is plotted for dates of observations covering the same sub-observer point longitudes: $\Lambda = 180^\circ$–204° on 23 November 2011, 11 October 2012 and 6 March 2013 (black dots); $\Lambda = 21^\circ$–103° on 24 October 2012 and 6 March 2013 (red dots). Error bars are 1σ. The strength of the absorption is variable on timescales of hours or months.

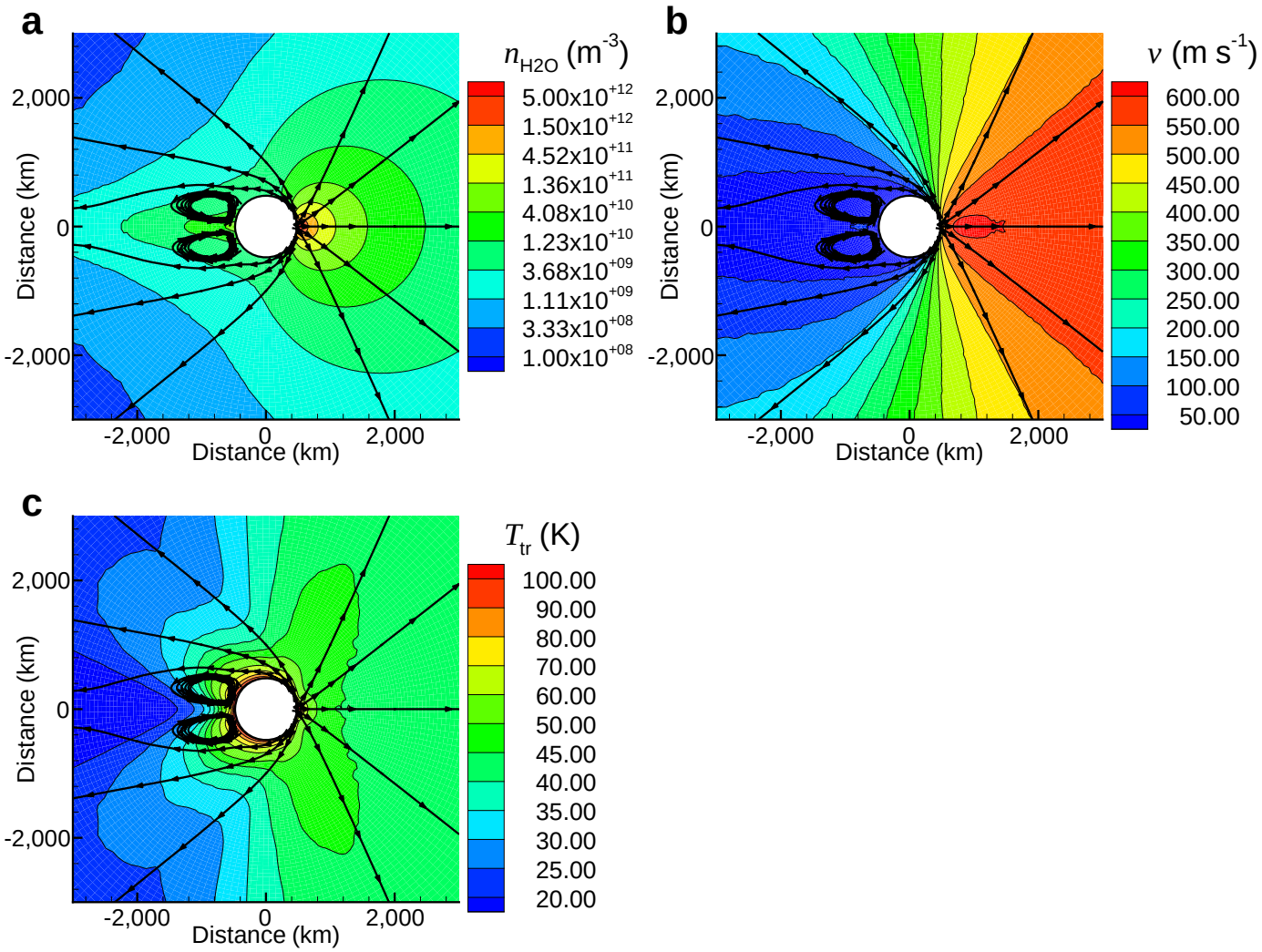

Extended Data Figure 2 | Direct Simulation Monte Carlo calculations of the exosphere of Ceres. **a–c,** Number density n_{H2O} (**a**), velocity v (**b**) and translational temperature T_{tr} (**c**) for water outgassing from an active spot about 60 km in diameter situated on the surface of Ceres at the subsolar point. The Sun is towards the right. The total water production rate is 10^{26} molecules per second. The Ceres surface temperature varies from 235 K (subsolar) to 168 K. See Supplementary Information. Stream lines are shown in black. The vortex seen on the night side is caused by the competition of molecules falling back on the surface owing to gravity and those molecules diffusing outwards. The local maximum in velocity observed above the active spot is also an effect of gravity. The gravity of Ceres causes 3% of the evaporated molecules to fall back to the surface, whereas 7% fall back owing to collisions between water molecules in the atmosphere.

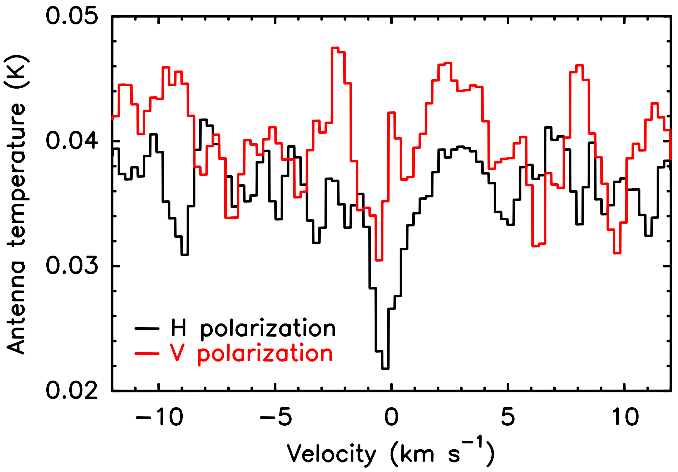

Extended Data Figure 3 | The spectrum from 11 October 2012 in H and V polarizations. Although there is no significant polarization in the continuum, the line area is about 2.5 times larger in horizontal polarization than in the marginal detection of the line in vertical polarization.

Extended Data Table 1 | Overview of the acquired data

Start date and time	Duration	r	Δ	Sub-observer point		Sub-solar point		Phase
				Λ	ε	Λ_S	ε_S	ϕ
(UT)	(s)	(AU)	(AU)	(°)	(°)	(°)	(°)	(°)
2011-11-23 11:31:20	4010	2.94	2.51	224-180	5	243-200	3	19
2012-10-11 19:53:46	8245	2.72	2.26	247-156	1	227-139	−1	21
2012-10-24 20:04:28	8575	2.71	2.09	103-8	1	84-350	−1	19
2013-03-06 03:05:42	8575	2.62	2.31	130-35	−7	152-57	−3	22
2013-03-06 05:30:03	9146	2.62	2.31	34-293	−7	56-318	−3	22
2013-03-06 08:03:55	9146	2.62	2.31	292-192	−7	317-214	−3	22
2013-03-06 10:37:47	9146	2.62	2.31	191-90	−7	213-111	−3	22

Geometric parameters of the observations are the heliocentric distance of Ceres r, the Ceres–Herschel distance Δ, the sub-observer point longitude Λ and subsolar point longitude Λ_S at the beginning and end of each observation[14,29], the sub-observer point latitude ε and subsolar point latitude ε_S (refs 14 and 29), and the phase angle ϕ. The Herschel observation identification numbers (Obsids) are 1342232694 (23 November 2011), 1342253122 (11 October 2012), 1342254428 (24 October 2012) and 1342266018–1342266021 (6 March 2013).

29. Chamberlain, M. A., Sykes, M. V. & Esquerdo, G. A. Ceres light curve analysis—period determination. *Icarus* **188,** 451–456 (2007).

Extended Data Table 2 | Continuum brightness in the spectra

Date (UT)	Measured continuum (Jy)	Expected continuum (Jy)
23.48-23.53 November 2011	7.24 ± 0.65	7.35 ± 0.4
11.83-11.92 October 2012	8.71 ± 1.16	9.78 ± 0.5
24.84-24.96 October 2012	11.48 ± 0.72	11.54 ± 0.6
6.13-6.55 March 2013	8.61 ± 0.62	8.74 ± 0.4

Measured and expected brightness of the continuum. The expected thermal continuum was calculated with a thermophysical model[30]. The estimated accuracy of the model is 5%.

30. Müller, T. G. *et al.* Herschel celestial calibration sources: four large main-belt asteroids as prime flux calibrators for the far-IR/sub-mm range. *Exp. Astron.* http://dx.doi.org/10.1007/s10686-013-9357-y (in the press).

Extended Data Table 3 | Characteristics of H_2O spectra

Date (UT)	Polarization	Line area (km s^{-1})	Offset (km s^{-1})	Width (km s^{-1})	Absorbance (%)
23.48-23.53 November 2011	H+V	0.07± 0.10	-	-	< 10
11.83-11.92 October 2012	H	−1.07 ± 0.12	−0.26 ± 0.07	1.37 ± 0.21	74
	V	−0.43 ± 0.12	−0.76 ± 0.15	0.96 ± 0.26	42
	H+V	−0.79 ± 0.10	−0.40 ± 0.09	1.43 ± 0.22	52
24.84-24.96 October 2012	H	−0.56 ± 0.09	−0.72 ± 0.11	1.21 ± 0.19	44
	V	−0.22 ± 0.06	−0.16 ± 0.09	0.61 ± 0.18	34
	H+V	−0.31 ± 0.06	−0.39 ± 0.07	0.73 ± 0.16	39
6.13-6.55 March 2013	H	−0.27 ± 0.04	−0.67 ± 0.05	0.69 ± 0.10	37
	V	−0.20 ± 0.04	−0.69 ± 0.09	0.67 ± 0.18	28
	H+V	−0.24 ± 0.03	−0.68 ± 0.05	0.68 ± 0.09	33

Results of Gaussian fits to the water 1_{10}–1_{01} absorption line, after normalizing by the thermal continuum emission from Ceres. Offset refers to the radial velocity of the line centre relative to that of Ceres. The last column provides the absorbance (the percentage of the continuum that is absorbed) at the line centre from a Gaussian fit to the absorption line (1σ upper limit for the first observation). The V/H line area ratios are 0.40 ± 0.12, 0.38 ± 0.13 and 0.74 ± 0.20, for 11 October, 24 October and 6 March, respectively.

Annex B

Determination of an upper limit for the water outgassing rate of MBC P/2012 T1

This chapter is linked to both of the objectives of the thesis whereby we search for and characterise ice found on the surface and subsurfaces of both comets and asteroids. The article covered in this chapter "Determination of an upper limit for the water outgassing rate of Main-Belt Comet P/2012 T1 (PANSTARRS)" was published in Astrophysics Journal Letters on September 1st 2013. In the bibliography, it is referenced as O'Rourke et al. 2013a. While the main cometary paper of the thesis (chapter 2) addresses the presence of water ice on the surface/subsurface of comet 67P/Churyomov-Gerasimenko, and the main asteroid paper (chapter 3) studies the case for two of the larger asteroids in the main belt, this current paper supports both objectives in that we searched for a dust and water vapour coma around a very small asteroid which displayed cometary behaviour (Main-BeltComet) with the aim to determine if there was surface ice being sublimated. We also estimated the size of the asteroid itself as well as (specific to this thesis) derived the upper limit for surface ice coverage.

This paper presents observations performed on Main-Belt Comet (MBC) P/2012 T1 that was discovered in October 2012. A request for "Director Discretionary Time" by LO'Rourke was approved to observe this MBC using the Herschel Space Observatory's HIFI instrument in January 2013 approximately 4 months after it had reached perihelion. The observation was to be performed in parallel with the use of the VLT FORS2 imager, on the basis that we could confirm that the MBC was still showing activity when we performed the HIFI spectral search for water vapour.

The VLT observed the MBC on the 15th January 2013 and Herschel on the 16th January 2013. It was confirmed very soon afterwards in the FORS2 images that the MBC was still active at the time of the Herschel observation. From this observation we calculated a dust production rate of 2.7 kg s^{-1} as well as derived an upper limit for the radius of the asteroid to be < 1.3km. While no H_2O line emission was detected by HIFI in our observations, we were able to derive sensitive 3σ upper limits for the water production rate and column density of $<7.63 \times 10^{25}$ molecules s^{-1} and of $<1.61 \times 10^{11}$ cm^{-2}, respectively.

Although a non-detection, our results represents the first (and only) direct search for gaseous H_2O in an exosphere around an MBC while it was confirmed to be active. A study is presented in Chapter 4.2 which covers the scientific progress achieved in the area of MBCs since we published our paper.

The Astrophysical Journal Letters, 774:L13 (4pp), 2013 September 1 doi:10.1088/2041-8205/774/1/L13

DETERMINATION OF AN UPPER LIMIT FOR THE WATER OUTGASSING RATE OF MAIN-BELT COMET P/2012 T1 (PANSTARRS)*

L. O'Rourke[1], C. Snodgrass[2], M. de Val-Borro[2,3], N. Biver[4], D. Bockelée-Morvan[4], H. Hsieh[5], D. Teyssier[1], Y. Fernandez[6], M. Kueppers[1], M. Micheli[7], and P. Hartogh[2]
[1] European Space Astronomy Centre, ESAC, Villanueva de la Canada, E-28691 Madrid, Spain; lorourke@esa.int
[2] Max Planck Institute for Solar System Research, Max-Planck-Str. 2, D-37191 Katlenburg-Lindau, Germany
[3] Department of Astrophysical Sciences, Princeton University, Princeton, NJ 08544, USA
[4] LESIA, Observatoire de Paris, CNRS, UPMC, Université Paris-Diderot, 5 place Jules Janssen, F-92195 Meudon, France
[5] Institute for Astronomy, University of Hawaii, 2680 Woodlawn Drive, Honolulu, HI 96822, USA
[6] Department of Physics, University of Central Florida, 4000 Central Florida Blvd, Orlando, FL 32816-2385, USA
[7] Institute for Astronomy, University of Hawaii, 2680 Woodlawn Drive, Honolulu, HI 96822, USA
Received 2013 July 6; accepted 2013 July 25; published 2013 August 21

ABSTRACT

A new Main-Belt Comet (MBC) P/2012 T1 (PANSTARRS) was discovered on 2012 October 6, approximately one month after its perihelion, by the Pan-STARRS1 survey based in Hawaii. It displayed cometary activity upon its discovery with one hypothesis being that the activity was driven by sublimation of ices; as a result, we searched for emission assumed to be driven by the sublimation of subsurface ices. Our search was of the H_2O 1_{10}–1_{01} ground state rotational line at 557 GHz from P/2012 T1 (PANSTARRS) with the Heterodyne Instrument for the Far Infrared on board the *Herschel Space Observatory* on 2013 January 16, when the object was at a heliocentric distance of 2.504 AU and a geocentric distance of 2.064 AU. Perihelion was in early 2012 September at a distance of 2.411 AU. While no H_2O line emission was detected in our observations, we were able to derive sensitive 3σ upper limits for the water production rate and column density of $<7.63 \times 10^{25}$ molecules s^{-1} and of $<1.61 \times 10^{11}$ cm^{-2}, respectively. An observation taken on 2013 January 15 using the Very Large Telescope found the MBC to be active during the *Herschel* observation, suggesting that any ongoing sublimation due to subsurface ice was lower than our upper limit.

Key words: comets: individual (P/2012 T1 PANSTARRS) – minor planets, asteroids: individual (P/2012 T1 PANSTARRS)

Online-only material: color figure

1. INTRODUCTION

Recent observational and theoretical developments have suggested that the objects between Mars and Jupiter in the Main Asteroid Belt hold considerably more water ice than traditionally thought—as distinct from the widespread observation of hydrated minerals in asteroids (e.g., Rivkin et al. 2002; Vilas & Gaffey 1989). They would hold this water ice despite being in orbits that are presumably stable over the lifetime of the solar system and thus having surfaces that have received significant solar energy input. For example, the snow line at the time of planet formation could have been close to Mars' orbit (Sasselov & Lecar 2000; Lecar et al. 2006); subsurface ice in asteroids can survive for the age of the solar system if buried under a dusty surface (Schorghofer 2008); surface ice has possibly been detected on the large main-belt asteroid (24) Themis (Rivkin & Emery 2010; Campins et al. 2010).

Further evidence for significant water in the Main Belt comes from the so-called Main-Belt Comets (MBCs; Hsieh & Jewitt 2006; Bertini 2011; Jewitt 2012). These objects show cometary activity, and that cometary activity appears to be sustained rather than impulsive. The MBCs have orbits squarely within the Main Belt, and their orbits are found to be stable; as such, the objects are considered likely to be native to their current residence regions in the Main Belt. Thus, the implication is that volatile material incorporated into these bodies when they formed has survived to the present day. This also means that MBCs have the potential to place observational constraints on the temperature and compositional structure of the early solar system and our protoplanetary disk, giving insight into the solar system's formation.

In a recent study (Waszczak et al. 2013) of the Palomar Transient Factory survey database, upper limits on the possible population size of active MBCs were derived at a 2σ level of 22 active MBCs (per million main-belt asteroids down to 1 km diameter). We note that of the 10 known Main Belt objects observed to have shown extended emission from dust, we consider 7 of them to be MBCs (i.e., excluding P/2010 A2, P/2012 F5, and (596) Scheila), apparently having sustained activity due to sublimation of ices as the more traditional comets do. P/2012 T1, the object considered here, would be the seventh MBC.

The MBC P/2012 T1 (PANSTARRS) was discovered on October 6 by the 1.8 m Pan-STARRS1 (PS1) survey telescope on Haleakala with follow-up images confirming the object to be cometary in nature with a 10″–15″-long tail (Wainscoat et al. 2012). Observation campaigns performed by various ground-based observatories (Keck 10 m, the University of Hawaii 2.2 m, 6.5 m Baade, 6.5 m Clay Magellan, 1.8 m Perkins, etc.; Hsieh et al. 2013) found the object's intrinsic brightness roughly doubling from the time of its discovery until mid-November, after which it was then seen to decrease by ≈60% from late December to early February. Similar long-lived photometric behavior has been observed for several other MBCs, suggesting that the activity of P/2012 T1, deemed to

* *Herschel* is an ESA space observatory with science instruments provided by European-led Principal Investigator consortia and with important participation from NASA.

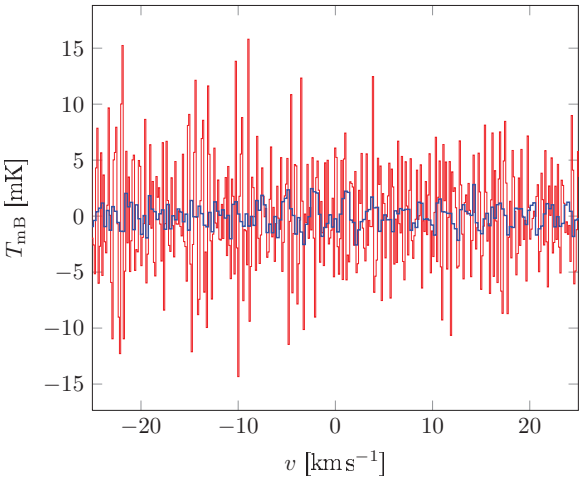

Figure 1. Averaged spectra of the two orthogonal polarizations of the H_2O line 1_{10}–1_{01} at 556.936 GHz toward the MBC P/2012 T1 (PANSTARRS) obtained by *Herschel*/HIFI on UT 2013 January 16.31 with the WBS (thick blue line) and HRS (thin red line) spectrometers. The HRS spectrum have been resampled to a 480 kHz resolution per channel with a rectangular window function. The vertical axis is the calibrated main beam brightness temperature and the horizontal axis is the cometocentric Doppler velocity.

(A color version of this figure is available in the online journal.)

belong to the Lixiaohua asteroid family, could likewise be driven by sublimation (Hsieh et al. 2012a, 2012b, 2013).

While sublimation of water ice in main-belt objects is strongly implied by MBC activity, gas has never been directly observed via spectroscopy, though attempts have been made (Jewitt et al. 2009; Hsieh et al. 2012b, 2012c, 2013; de Val-Borro et al. 2012a). Given the difficulty of detecting weak, distant, and transient gas emission, these non-detections do not rule out the presence of gas, however. A bright and actively sublimating MBC offers the unique opportunity to confirm the presence of sublimating volatile material in a main-belt object, and thus confirm the plausibility of ice in all of the other MBCs. This would strongly validate the potential that MBCs are believed to have for tracing the volatile content of the inner solar system. The Heterodyne Instrument for the Far Infrared (HIFI; de Graauw et al. 2010) on board the ESA *Herschel Space Observatory* (Pilbratt et al. 2010) proves to be the most sensitive instrument for directly observing water in a distant comet (e.g., Bockelée-Morvan et al. 2010). The HIFI instrument provides very high-resolution spectroscopy that can resolve the line shape and enable the determination of accurate production rates (e.g., Hartogh et al. 2010).

In this Letter, we present the *Herschel* DDT (Director Discretionary Time) observation of the 1_{10}–1_{01} fundamental rotational transition of H_2O at 557 GHz in P/2012 T1. This observation was requested to be performed on 2013 January 16, at the opening of the *Herschel* visibility window for the target, when the MBC was deemed to be still active; this was confirmed via our DDT observations using the VLT FORS2 instrument (Appenzeller et al. 1998) performed on January 15. The *Herschel* observation was intended to test the prediction that the observed cometary activity of MBCs is driven by sublimation of water ices and to constrain the production process.

2. OBSERVATIONS

On the basis of its obvious and ongoing activity following its perihelion passage in early 2012 September, the MBC P/2012 T1 was observed by *Herschel* on UT 2013 January 16.31 with a total on-target integration time of 4.8 hr, when it was at an approximate heliocentric distance of 2.504 AU, a distance of 2.064 AU from the satellite (*Herschel* ObsID 1342259756), and at a phase angle of 22.°55. The object was tracked using an up-to-date ephemeris provided by the JPL Horizons system.

The line emission from the fundamental *ortho*-H_2O 1_{10}–1_{01} line at 556.936 GHz was searched for in the upper sideband of the HIFI band 1a mixer. The observation was performed in the frequency-switching observing mode with a frequency throw of 94.5 MHz, using both the wide-band spectrometer (WBS) and the high-resolution spectrometer (HRS). In this observing mode there is no need to observe a reference position on the sky and the on-target integration time is maximized. However, the statistical noise may be underestimated for observations in frequency-switched mode owing to uncertainties in baseline removal (Bockelée-Morvan et al. 2012).

In addition to the *Herschel* observations, three 300 s *V*-band VLT FORS2 images were taken around 01:00 UT on 2013 January 15, with the telescope tracking the comet's motion. At this time the comet was at 2.502 AU from the Sun, 2.052 AU from Earth, and at a phase angle of 22.°26.

3. DATA ANALYSIS

In the case of the HIFI data set, the standard HIFI processing pipeline v9.2 (belonging to the Herschel interactive processing environment software package; Ott 2010) was used to reduce the data to calibrated level 2 data products.

The spectral resolution of the WBS is 1 MHz (0.54 km s^{-1} at the frequency of the observed line), while the HRS was used in its high-resolution mode with a resolution of 120 kHz (0.065 km s^{-1}). The main beam brightness temperature scale was computed using a beam efficiency of 0.75 and a forward efficiency of 0.96. The folded spectrum was obtained by averaging the original spectrum with a shifted and inverted copy. Horizontal and vertical polarizations were averaged, weighted by the root mean square amplitude, to increase the signal-to-noise ratio. The pointing offset of horizontal and vertical polarization spectra is 6.″6 in band 1a, which, at the observed frequency, is approximately 20% of the half-power beam width.

The frequency switching observing mode introduces quite a strong baseline ripple that can be removed by performing a least-squares fit of a linear combination of sine waves. We applied the Lomb–Scargle periodogram method (initially proposed by Lomb 1976, and additionally developed by Scargle 1982) to the HRS and WBS spectra and fitted the baseline ripple using the strongest peaks in the frequency spectrum. The reduction methods applied for baseline removal and denoising of the *Herschel*/HIFI data are described in greater detail in de Val-Borro et al. (2012b). We show the averaged spectra of the two orthogonal polarizations in the HRS and WBS spectra in Figure 1.

In the case of the three VLT FORS2 *V* band images, the first image was affected by a cosmic ray near to the comet, but the sum of the remaining frames is shown in Figure 2. The comet was clearly active at that time, approximately one day before the *Herschel* observations. The seeing, measured using the FWHM of the star trails in this image, was around 0.″8 and conditions were photometric. Photometry was performed with an aperture of radius 3.″06 to avoid contamination from the nearby trailed star. The magnitude within this aperture is $m_V = 21.47 \pm 0.01$, corresponding to a reduced magnitude of $V(1,1,0) = 17.47$, assuming a phase function of 0.02 mag deg^{-1}, appropriate for cometary dust (Meech & Jewitt 1987). The corresponding

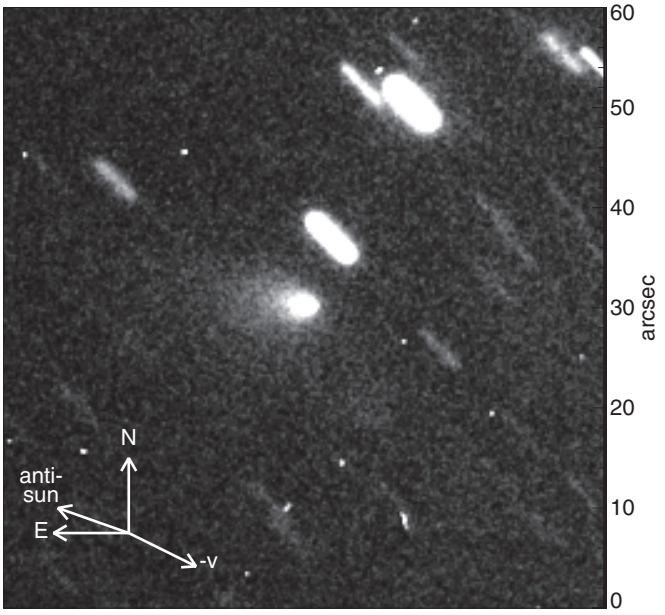

Figure 2. Context broad band image of the MBC on the 2013 January 15 using the VLT FORS2 detector.

$Af\rho$ value (A'Hearn et al. 1989) is 2.7 cm (not including any phase angle correction), with the $\rho = 3''.06$ aperture radius corresponding to 4560 km at the distance of the comet.

The slope of the radial profile is −1.6, slightly steeper than expected for a steady-state coma under the influence of radiation pressure (Jewitt & Meech 1987), which means that $Af\rho$ is not independent of the choice of ρ in this case. We can say that it is very low, implying a weakly active comet. This low value is comparable with what has been provided by Hsieh et al. (2013) on this target for the January timeframe. The photometry also allows us to place an upper limit on the size of the nucleus: We obtain $r < 1.3$ km, assuming typical comet nucleus values for the geometric albedo (4%) and phase function (0.04 mag deg^{-1}).

4. OUTGASSING RATE UPPER LIMIT

Upon analyzing our data, we found no detection of H_2O, although with the fact that it was shown to be still active at the time of our observation, we expected the dust emission activity to be driven by the sublimation of subsurface material.

We used a molecular excitation model to calculate the population of the rotational levels of water as a function of nucleocentric distance as well as to derive the production rates. The model in use is based upon the publicly available accelerated Monte Carlo radiative transfer code ratran (Hogerheijde & van der Tak 2000). To derive the production rates, the code includes collisional effects as well as infrared fluorescence by solar radiation. We used the one-dimensional spherically symmetric version of the code as described in Bensch & Bergin (2004). This same version has been utilized to analyze both *Herschel* and ground-based cometary observations (Hartogh et al. 2010, 2011; de Val-Borro et al. 2010, 2012a, 2012b).

Input parameters to this model include the electron density, gas kinetic temperature, expansion velocity, and the radial gas density profile.

Electron density and gas kinetic temperature profile values extracted from (Biver et al. 1997; de Val-Borro et al. 2010) were fed into the model. For the case of the kinetic temperature (used to control the molecular excitation in the collisional region), a range of values from 10 to 20 K was input. Since the electron density in the coma is not well constrained, an electron density scaling factor of $x_{n_e} = 0.2$ with respect to the standard profile derived from observations of comet 1P/Halley has been used (e.g., Hartogh et al. 2010).

Table 1
H_2O Production Rate (Q_{H_2O}) and Column Density (N_{col}) Derived for Different Gas Kinetic Temperatures

Temperature (K)	Q_{H_2O} (molecules s^{-1})	N_{col} (cm^{-2})
10	$<8.0 \times 10^{25}$	$<1.68 \times 10^{11}$
15	$<7.6 \times 10^{25}$	$<1.60 \times 10^{11}$
20	$<7.3 \times 10^{25}$	$<1.54 \times 10^{11}$
Mean	$<7.63 \times 10^{25}$	$<1.61 \times 10^{11}$

Notes. Assuming a line area upper limit of 3.6 mK km s^{-1} $T_{mB}dv$ at 3σ, with the following excitation parameters $r_h = 2.504$ AU, $\Delta = 2.064$ AU, $v_{exp} = 0.5$ km s^{-1}, $x_{ne} = 0.2$, pointing offset $= 3''.5$ (if the comet was in between the two band 1A beams), one can obtain the following H_2O production rates and associated column densities for P/2012 T1, at different gas temperatures. Note that if a $v_{exp} = 0.4$ km s^{-1} is used, this would lower the Q_{H_2O} by 15%.

The expansion velocity (assumed constant in the coma), and the radial gas density profile for water was obtained based upon a standard spherically symmetric Haser distribution. For lower-activity comets, and in this case P/2012 T1, an expansion velocity of 0.5 km s^{-1}1 has been used (Tseng et al. 2007; Biver et al. 2007). While Tseng et al. (2007) are limited by measurements taken for $Q_{OH} < 10^{28}$ at r_h distances >2 AU, the Biver et al. (2007) paper gives the FWHM = 0.95 km s^{-1} for the comet C/2003 K4 (LINEAR) water line at 2.2 AU from the Sun, which can be interpreted as $v_{exp} = 0.5$ km s^{-1}, taking into account the fact that self-absorption makes the line a little narrower. Finally, from the temperature expected at the subsolar point where ice sublimates, we derived a thermal velocity of 0.35 km s^{-1}.

For the line area upper limit, based upon removal of sine baselines, with smoothing of approximately 25% and computed on a [−0.7 0.7 km s^{-1}] window, we derive a $1\sigma \int T_{mB}dv$ value of 1.63 mK km s^{-1} from the HRS spectrum and 0.88 mK km s^{-1} from the WBS spectrum.

Taking an upper limit of 3.6 mK km s^{-1} $\int T_{mB}dv$ at 3σ from the mean of the HRS and WBS values, we can obtain upper limits for the water production rate (Q) at different temperature ranges.

With this line area upper limit, using expansion velocity characteristic of weak comets (0.5 km s^{-1}), a gas kinetic temperature of 20 K, we derive a sensitive 3σ upper limit of $Q < 7.3 \times 10^{25}$ molecules s^{-1} from the WBS and HRS data (see Table 1). An upper limit of $<7.63 \times 10^{25}$ molecules s^{-1} is derived from the mean of the WBS and HRS upper limits for a gas expansion velocity of 0.5 km s^{-1} and gas kinetic temperatures of 10, 15, and 20 K.

5. DISCUSSION AND CONCLUSIONS

With the *Herschel* capability to directly detect H_2O in MBCs, it is important to stress the key relevance of such results to the knowledge of water production on these bodies.

In addition to the current work, this capability for direct measurements on MBCs has been demonstrated when MBC

176P/LINEAR was observed using *Herschel*/HIFI in 2011 August, about one month post-perihelion. In that case, no water line emission was detected and a 3σ upper limit was obtained on the production rate of $<4 \times 10^{25}$ molecules s^{-1} (de Val-Borro et al. 2012b).

Besides a direct detection, other means exist to derive water production rates although they are limited in nature and primarily model-dependent. We will look at two of these briefly for comparative purposes.

One particular way to derive H_2O production is via the search for CN. Searches for CN (and thus deriving a water production rate via a log based ratio linking Q_{CN} and Q_{OH} in "typical" comets) have taken place with four of the other MBCs, all of which were unsuccessful. For those MBCs, estimated water production rates of $Q < 10^{26}$ molecules s^{-1} were proposed using a Q_{CN}/Q_{OH} mixing ratio of 10^{-3}. For P/2012 T1, Hsieh et al. (2013) report that CN was also not detected but an estimate of the expected H_2O upper limit of $Q < 5 \times 10^{25}$ molecules s^{-1} based upon an average ratio for other comets has been made.

One can also derive a value for the production rate via the $Af\rho$ measurement using visible light observations to estimate the coma brightness of a typical Jupiter Family Comet. The visible light proxy for dust production is the quantity $Af\rho$, where A is the bond albedo of the dust, f is the dust area filling factor in the field-of-view, and ρ is the projected radius of the field-of-view, typically expressed in units of cm (A'Hearn et al. 1984). For comae with constant isotropic outflows, $Af\rho$ is independent of aperture size. With our FORS2 observation, a corresponding $Af\rho$ value (A'Hearn et al. 1989) of 2.7 cm (not including any phase angle correction) has been estimated. Assuming a first order approximation, where $Af\rho$ in cm is found to be roughly equal to the dust production rate in kg s^{-1} (A'Hearn et al. 1995), we find 2.7 kg s^{-1} of $H_2O = 9 \times 10^{25}$ molecules s^{-1}. Separate to this, we note that the photometry from our FORS2 observation also allowed us to place an upper limit on the radius of the nucleus which we estimate to be <1.3 km, assuming typical comet nucleus values for the geometric albedo (4%) and phase function (0.04 mag deg^{-1}).

The goal of the *Herschel* DDT observation was to detect H_2O in a clearly active MBC, assumed to be produced from sublimating subsurface ices. Besides sublimation of subsurface ices, other mechanisms have been proposed to drive mass loss from small bodies, including rotational instability, impact ejection and thermal fracture (see Jewitt 2012 for a recent review of mass loss mechanisms in MBCs). A study performed on this comet by Hsieh et al. (2013) for these different possibilities concluded that sublimation is indeed considered the key behind the observed activity.

Although the goal conditions of observing an active MBC were met, with our VLT FORS2 observation clearly showing activity and ground-based observations since that date confirming that the activity continued until the end of 2013 February (Moreno et al. 2013), we were, in the end, unsuccessful in achieving that goal as no detection of H_2O was made.

However, based upon our analysis above, and recognizing that: (1) the activity of the MBC observed at the time of the *Herschel* observation was already less than what was observed in the preceding months (Hsieh et al. 2013); (2) *Herschel* did not detect water but the measurement was successful in providing a sensitive 3σ upper limit; (3) the upper limits derived from less direct methods (Hsieh et al. 2013), e.g., $Af\rho$ measurements, provide values equivalent and comparable to our direct measurement (thus effectively supporting the strategies being used in such cases, where no direct measurements are available), we conclude that if the activity was due to sublimation of subsurface water ice, the water production rate at the time of our observations was lower than $<7.63 \times 10^{25}$ molecules s^{-1} for MBC P/2012 T1 (PANSTARRS).

We thank the Herschel Project Scientist and Time Allocation Committee for awarding five hours of Director Discretionary Time for this observation.

M.d.V.B. acknowledges support from grants NSF AST-1108686 and NASA NNX12AH91H.

Based in part on observations collected at the European Southern Observatory, Paranal, Chile, under programme 290.C-5028.

C.S. received funding from the European Union Seventh Framework Programme (FP7/2007-2013) under grant agreement No. 268421.

REFERENCES

A'Hearn, M. F., Campins, H., Schleicher, D. G., & Millis, R. L. 1989, ApJ, 347, 1155
A'Hearn, M. F., Millis, R. L., Schleicher, D. G., Osip, D. J., & Birch, P. V. 1995, Icar, 118, 223
A'Hearn, M. F., Schleicher, D. G., Millis, R. L., Feldman, P. D., & Thompson, D. T. 1984, AJ, 89, 579
Appenzeller, I., Fricke, K., Fürtig, W., et al. 1998, Msngr, 94, 1
Bensch, F., & Bergin, E. A. 2004, ApJ, 615, 531
Bertini, I. 2011, P&SS, 59, 365
Biver, N., Bockelée-Morvan, D., Colom, P., et al. 1997, EM&P, 78, 5
Biver, N., Bockelée-Morvan, D., Crovisier, J., et al. 2007, P&SS, 55, 1058
Bockelée-Morvan, D., Biver, N., Crovisier, J., et al. 2010, BAAS, 42, 946
Bockelée-Morvan, D., Biver, N., Swinyard, B., et al. 2012, A&A, 544, L15
Campins, H., Hargrove, K., Pinilla-Alonso, N., et al. 2010, Natur, 464, 1320
de Graauw, T., Helmich, F. P., Phillips, T. G., et al. 2010, A&A, 518, L6
de Val-Borro, M., Hartogh, P., Crovisier, J., et al. 2010, A&A, 521, L50
de Val-Borro, M., Hartogh, P., Jarchow, C., et al. 2012a, A&A, 545, A2
de Val-Borro, M., Rezac, L., Hartogh, P., et al. 2012b, A&A, 546, L4
Hartogh, P., Crovisier, J., de Val-Borro, M., et al. 2010, A&A, 518, L150
Hartogh, P., Lis, D. C., Bockelée-Morvan, D., et al. 2011, Natur, 478, 218
Hogerheijde, M. R., & van der Tak, F. F. S. 2000, A&A, 362, 697
Hsieh, H. H., & Jewitt, D. 2006, Sci, 312, 561
Hsieh, H. H., Kaluna, H. M., Novakovic, B., et al. 2013, ApJL, 771, L1
Hsieh, H. H., Yang, B., Haghighipour, N., et al. 2012a, AJ, 143, 104
Hsieh, H. H., Yang, B., Haghighipour, N., et al. 2012b, ApJL, 748, L15
Hsieh, H. H., Yang, B., & Haghighipour, N. 2012c, ApJ, 744, 9
Jewitt, D. 2012, AJ, 143, 66
Jewitt, D., Yang, B., & Haghighipour, N. 2009, AJ, 137, 4313
Jewitt, D. C., & Meech, K. J. 1987, ApJ, 317, 992
Lecar, M., Podolak, M., Sasselov, D., & Chiang, E. 2006, ApJ, 640, 1115
Lomb, N. R. 1976, Ap&SS, 39, 447
Meech, K. J., & Jewitt, D. C. 1987, A&A, 187, 585
Moreno, F., Cabrera-Lavers, A., Vaduvescu, O., Licandro, J., & Pozuelos, F. 2013, ApJL, 770, L30
Ott, S. 2010, in ASP Conf. Ser. 434, Astronomical Data Analysis Software and Systems XIX, ed. Y. Mizumoto, K.-I. Morita, & M. Ohishi (San Francisco, CA: ASP), 139
Pilbratt, G. L., Riedinger, J. R., Passvogel, T., et al. 2010, A&A, 518, L1
Rivkin, A. S., & Emery, J. P. 2010, Natur, 464, 1322
Rivkin, A. S., Howell, E. S., Vilas, F., & Lebofsky, L. A. 2002, Asteroids III (Tucson, AZ: Univ. Arizona Press), 235
Sasselov, D. D., & Lecar, M. 2000, ApJ, 528, 995
Scargle, J. D. 1982, ApJ, 263, 835
Schorghofer, N. 2008, ApJ, 682, 697
Tseng, W.-L., Bockelée-Morvan, D., Crovisier, J., Colom, P., & Ip, W.-H. 2007, A&A, 467, 729
Vilas, F., & Gaffey, M. J. 1989, Sci, 246, 790
Wainscoat, R., Hsieh, H., Denneau, L., et al. 2012, CBET, 3252, 1
Waszczak, A., Ofek, E. O., Aharonson, O., et al. 2013, MNRAS, 433, 3115

Annex C

Observatories & Instrumentation used in this work

C.1 The Rosetta Spacecraft & the Philae Lander instruments

C.1.1 Background to the Rosetta mission & the Philae Landing

The Rosetta mission was a cornerstone mission of the ESA Horizon 2000 programme (Glassmeier et al. 2007). Launched in March 2004, it arrived at its prime destination comet 67P/Churyumov-Gerasimenko (CG) in August 2014, after a 10-year voyage across the solar system. After arrival, activities immediately kicked off to select a landing site for the Philae Lander that had accompanied Rosetta on its journey (Ulamec et al. 2015). With the landing site "Agilkia" selected in September 2014, preparation began for the separation of Philae a number of weeks later.

Philae separated from Rosetta in the early hours of 12th of November 2014 and drifted down to the surface during a seven-hour descent phase. Communication between Philae and Rosetta was via the "Electrical Support System" (ESS) located on Rosetta (McKenna Lawlor et al. 2016). Contact with the ESS was established approximately 1 hour after separation allowing the touchdown to be monitored by the control centres located at ESOC (European Space Operations Centre) for the Rosetta Spacecraft and at DLR (Deutsches Zentrum für Luft- und Raumfahrt) for the Philae Lander.

At touchdown, the lander's harpoons failed to fire resulting in Philae bouncing and rising once again from the surface. It travelled across the surface for a period of 2 hours, touching the surface twice more (as a collision and then a touchdown) before finally settling down in a region over one kilometre away from Agilkia (Biele et al. 2015).

Philae was operational throughout this full period and was to continue for another 63.73 hours providing unique in-situ science from all of its ten instruments (Science Special Issue, 2015). Images taken by the CIVA camera (Bibring et al. 2015) provided crucial information as to the local terrain surrounding Philae.

Communication (Dudal et al. 2016) between Philae and Rosetta via the ESS gave clues as to the location of the lander with respect to Rosetta. In addition, data from the CONSERT (Comet Nucleus Sounding Experiment by Radiowave Transmission) instrument, located on both Rosetta and Philae, was key to help identify Philae's location in a region just off the edge of the Hatmehit depression. When its primary batteries had depleted Philae entered into hibernation leaving its exact location on the surface undetermined. Following an extensive campaign led by O'Rourke et al. (2019), the Philae lander was finally imaged in great detail in

the “Abydos” region on the 2nd September 2016 (see Figure C-1). The Rosetta mission ended on the 30th September 2016.

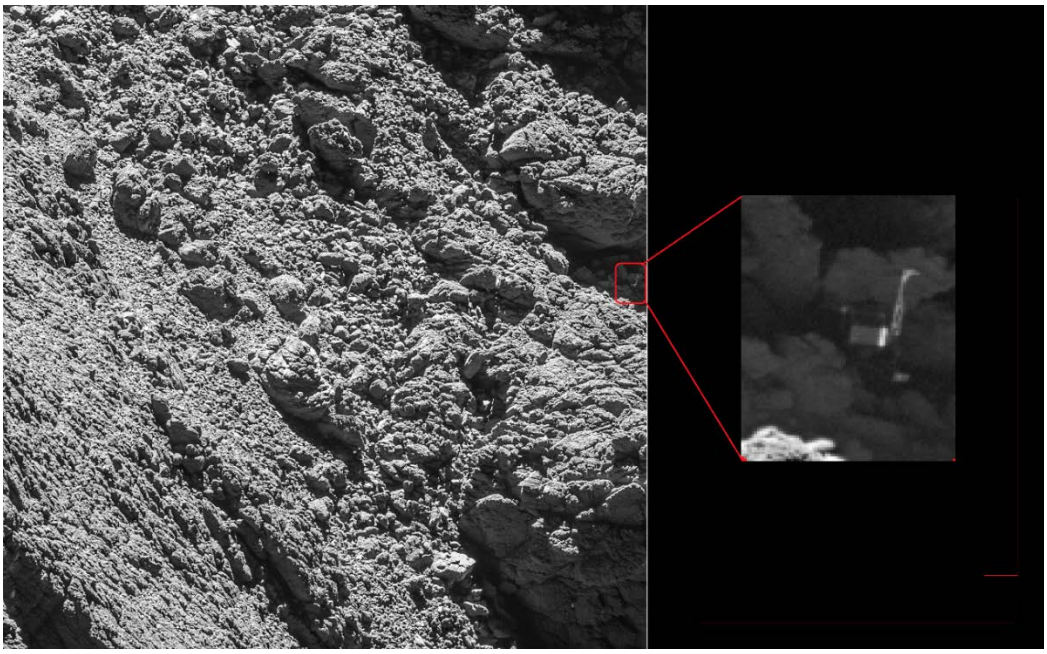

Figure C-1 taken from O’Rourke et al. (2019) : OSIRIS image taken on the 2nd of September 2016 from a distance of 2.7 km. The image scale is about 5 cm/pixel. The image shows Philae’s 1 m-wide body and two of its three legs can be seen extended from the body. The images also provide proof of Philae’s orientation. Credit: ESA/Rosetta/MPS for OSIRIS Team MPS/UPD/LAM/IAA/SSO/INTA/UPM/DASP/IDA. Processed by ESA/Rosetta/SGS

C.1.2 The Rosetta Spacecraft instrumentation used in support of this paper

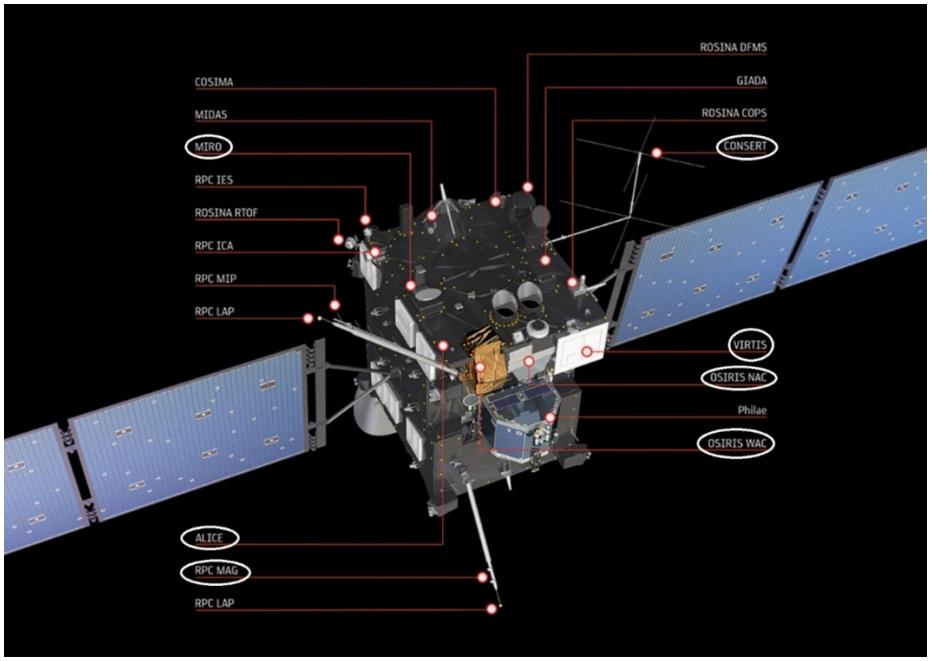

Figure C-2 : Rosetta Spacecraft with instrumentation marked. Image credit : European Space Agency

The following instruments, as shown in Figure C-2, were used in support of this scientific paper :

- **ALICE (Ultraviolet Imaging Spectrometer)** analyses gases in the coma and tail and measures the comet's production rates of water and carbon monoxide/dioxide. It also provides information on the surface composition of the nucleus.
- **MIRO (Microwave Instrument for the Rosetta Orbiter)** is used to determine the abundances of major gases, the surface outgassing rate and the nucleus subsurface temperature.
- **OSIRIS (Optical, Spectroscopic and Infrared Remote Imaging System)** has a wide-angle camera and narrow-angle camera that can obtain high-resolution images of the comet's nucleus. The OSIRIS instrument (Keller et al. 2007) comprised two cameras: a high resolution Narrow Angle Camera (NAC) and a Wide Angle Camera (WAC). Both are unobstructed off-axis mirror systems, equipped with two filter wheels containing 8 positions each, and with backside illuminated CCD detectors comprising 2048 x 2048 pixels with a pixel size of 13.5 µm.
- **RPC-MAG (Rosetta Plasma Consortium)**. In this instrument, five sensors measure the physical properties of the nucleus, examine the structure of the inner coma, monitor cometary activity, and study the comet's interaction with the solar wind. The RPC-MAG instrument in particular serves as a solar wind monitor.
- **VIRTIS (Visible and Infrared Thermal Imaging Spectrometer)** maps and studies the nature of the solids and the temperature on the surface of the nucleus. Also identifies comet gases, characterises the physical conditions of the coma and helps to identify the best landing sites.

C.1.3 The Philae Lander instrumentation used in support of this paper

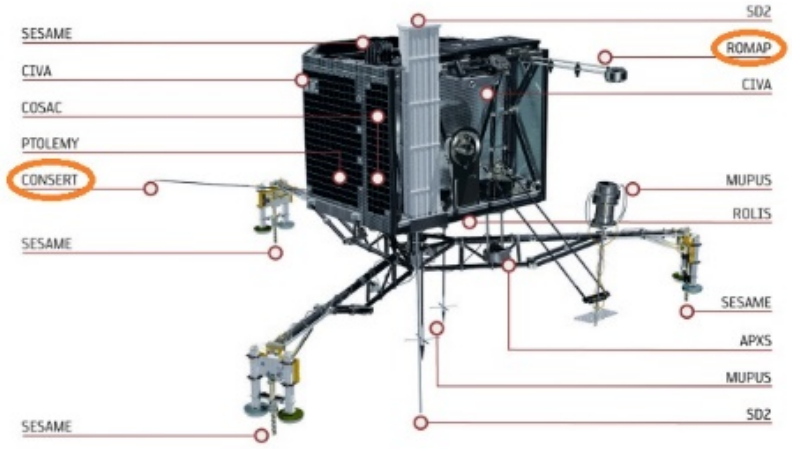

Figure C-3 : Philae Lander with instrumentation marked. Image credit : European Space Agency

- The CONSERT radar (COmet Nucleus Sounding Experiment by Radio wave Transmission) – see Figure C-3 – (Kofman et al. 2015) determined the comets internal structures as well as deduced information on its composition by performing tomography of the nucleus measuring

electromagnetic wave propagation between the Philae Lander and the Rosetta Orbiter as it passed throughout the comet nucleus.

- ROMAP (Rosetta Lander Magnetometer and Plasma detector) (Auster et al. 2007) was a combination of a magnetometer and plasma instrument with high temporal and spatial resolution.

Other instruments not specifically used but mentioned in the paper are the SD2 tower which sticks out from the top of the lander and left its impression in the ice. Also the MUPUS instrument which tried to hammer into the surface but failed (most likely because it fell over after deployment).

C.2 The Herschel Space Observatory

C.2.1 Background to the Herschel mission

Figure C-4 : The Herschel Space Telescope (ESA)

The Herschel Space Observatory (Pilbratt et al. 2010) was the largest infrared space observatory ever launched (Figure C-4). Equipped with a 3.5 metre diameter reflecting telescope and instruments cooled to close to absolute zero using liquid Helium, Herschel observed at wavelengths that had never previously been explored. Launching on an Ariane 5 rocket in May 2009, it entered its operational orbit around the second Lagrange point of the Sun-Earth system (L2) approximately 50 days later, to begin a nominal mission lifetime of three years. Herschel ran out of Helium on the 29th April 2013.

It had three instruments on-board covering from the far infrared to sub-millimetre parts of the spectrum (from 55 to 672 μm). These were:

- HIFI (**H**eterodyne **I**nstrument for the **F**ar **I**nfrared), a very high resolution heterodyne spectrometer
- PACS (**P**hotodetector **A**rray **C**amera and **S**pectrometer) - an imaging photometer and medium resolution grating spectrometer

- SPIRE (**S**pectral and **P**hotometric **I**maging **R**eceiver) - an imaging photometer and an imaging Fourier transform spectrometer

C.2.2 Background to the HIFI Instrument

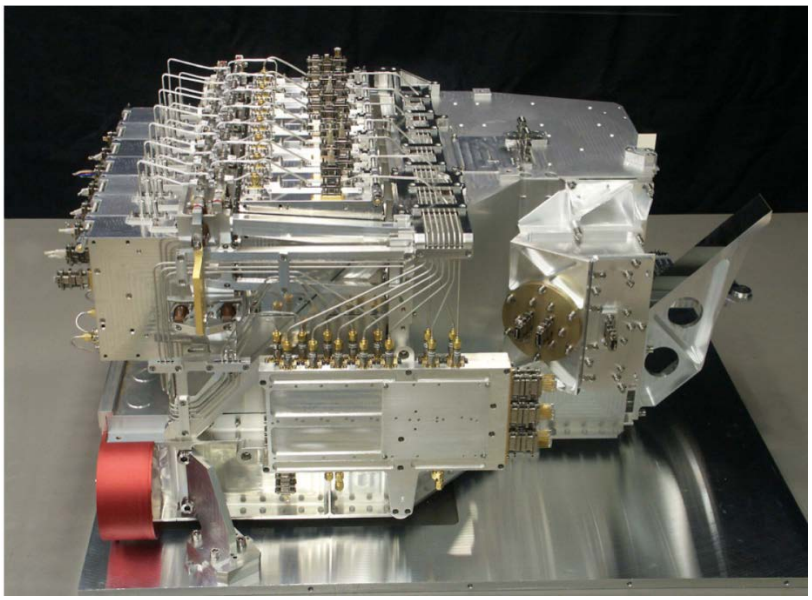

Figure C-5 : The HIFI Instrument (de Graauw et al. 2010)

HIFI (the Heterodyne Instrument for the Far-Infrared) – Figure C-5 - was the high-resolution spectrometer flown on-board the Herschel Space Observatory (de Graauw et al. 2010). It provided continuous frequency coverage from 480–1272 GHz and 1430–1906 GHz (625–240 and 208–157 μm, respectively), by means of 7 dual-polarisation (H and V) mixer bands which were used one pair at a time. Each of these 7 bands were then further split into two sub-bands ("a" and "b") representing the Local Oscillator (LO) chains covering adjacent frequency ranges.

HIFI was a Double Sideband (DSB) heterodyne detector, meaning that two areas of the electromagnetic spectrum could be simultaneously sampled onto each respective spectrometer bandwidth. Those two spectral ranges, called the Upper Sideband (USB) and the Lower Sideband (LSB), can be seen in Figure C-6 below.

HIFI consisted of two different types of spectrometers:

- a Wide-Band Spectrometer (WBS) allowing to sample the data on simultaneous bandwidths of 4 GHz (for bands 1 to 5) or 2.4 GHz (for bands 6 and 7) with a constant spectral resolution of 1.1MHz (0.17 to 0.7 km/s depending on the observed frequency), and

- a High-Resolution Spectrometer (HRS) with a spectral resolution adaptable between 0.125 and 1MHz and four different modes (High-resolution, Nominal resolution, Low resolution and Wideband resolution, respectively), and a simultaneous bandwidth between 230MHz and 2 GHz.

HIFI was a single pixel instrument with diffraction-limited spatial resolution. This implied that the Half-Power Beam Widths (HPBWs) were in the range 11–44 arcsec.

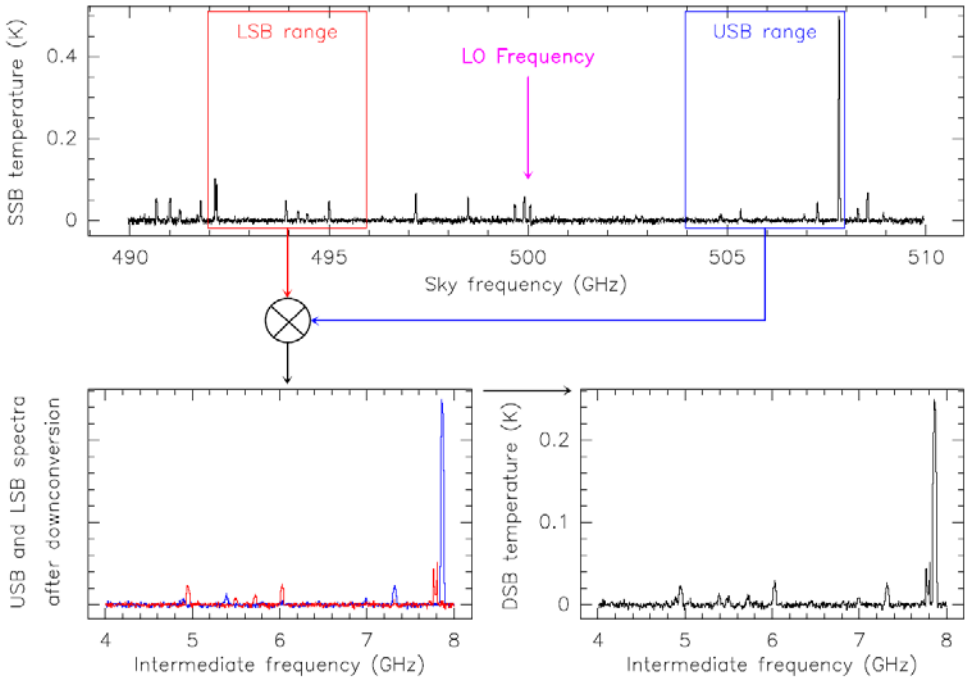

Figure C-6: Taken from the HIFI quick user guide (copyright ESA); Illustration of the heterodyne mixing on a band 1a HIFI spectrum. The spectrum on a sky frequency scale is shown in the upper panel, together with the respective LSB and USB frequency ranges implied by tuning frequency of 500 GHz, and a separation (also called Intermediate Frequency, or IF) of 6 GHz. The respective sideband spectra (LSB in red, USB in blue) in the lower panel is shown as it gets combined in the Double Sideband spectrum by the heterodyne down-conversion. Note how the LSB spectrum is flipped in its frequency scale. The final DSB spectrum, lower right panel, is the sum of the respective USB and LSB spectra.

The HIFI Pointing Modes

The HIFI instrument had three main pointing modes (and multiple sub-modes). These were :

- Single Point, for observing science targets at one position on the sky;
- Mapping, for covering extended regions;
- Spectral Scanning, for surveying a single position on the sky over a continuous range of frequencies within one of HIFI's 14 LO subbands.

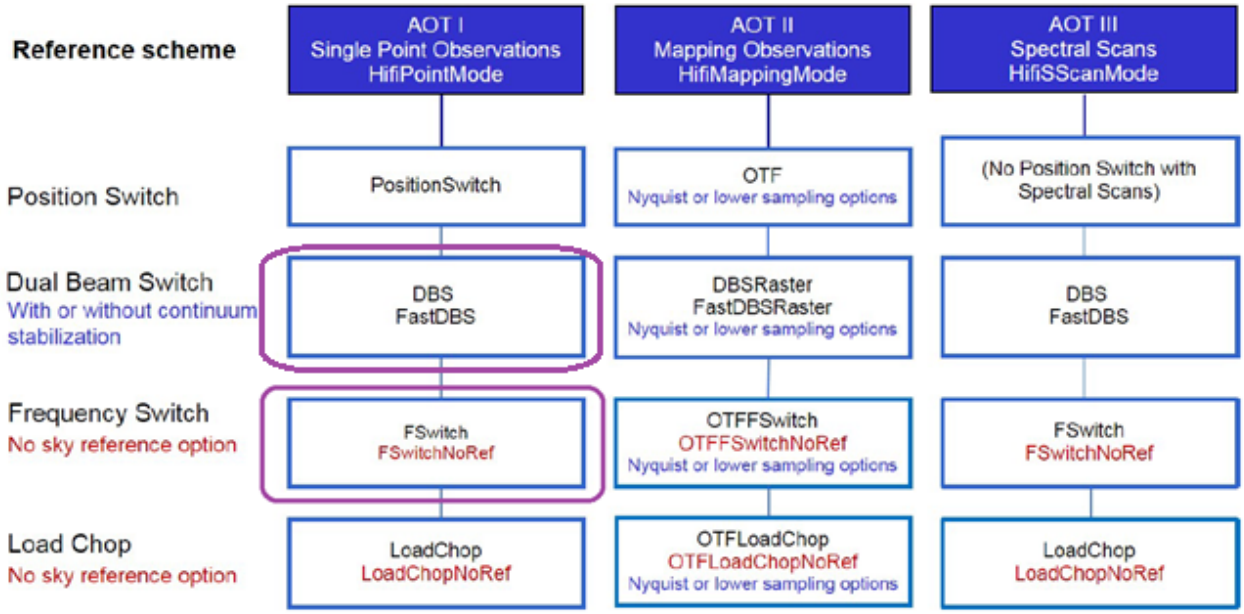

Figure C-7 : Taken from the HIFI quick user guide (copyright ESA), shows the different sub-modes contained within the three main HIFI observing modes (defined above as AOTs). The observations described in the next section were carried out in Dual Beam Switch mode (DBS) and the Frequency Switching mode (no Reference) highlighted in purple in the figure.

All observations presented in this thesis used the HIFIPointMode - Single Point observations mode.

C.2.3 Background to the SPIRE Instrument

The SPIRE instrument on-board the Herschel Space Observatory was a camera and low to medium resolution spectrometer covering the wavelengths 194-672 μm. It consisted of an imaging photometer and a Fourier Transform Spectrometer (FTS), both of which use bolometer detector arrays. There were a total of five arrays, three of which were dedicated for photometry and two for spectroscopy. The observing modes used in the observations performed were the large mapping mode and the small mapping mode.

C.3 The Subaru Telescope & COMICS Instrument

C.3.1 The Subaru Telescope

The Subaru telescope is an 8.2-meter optical-infrared telescope located on the summit of Maunakea, Hawaii. It is operated by the National Astronomical Observatory of Japan (NAOJ) and by the National Institutes of Natural Sciences. It is equipped with six prime instruments and one secondary observational instrument, using a wide range of methods to observe the sky in wavelengths from visible light to infrared.

C.3.2 Background to the COMICS Instrument

The Mid-infrared photometric observations for Themis were conducted using the Cooled Mid-Infrared Camera and Spectrometer (COMICS; Kataza et al. 2000) which is installed at the f/12 Cassegrain focus of the

8.2 m Subaru Telescope (see Figure C-8 below). The 320 x 240 pixel Si:As BIB detector for COMICS consists of 50 μm square pixels. This gives a 42" x 32" field of view with a pixel scale of 0.135".

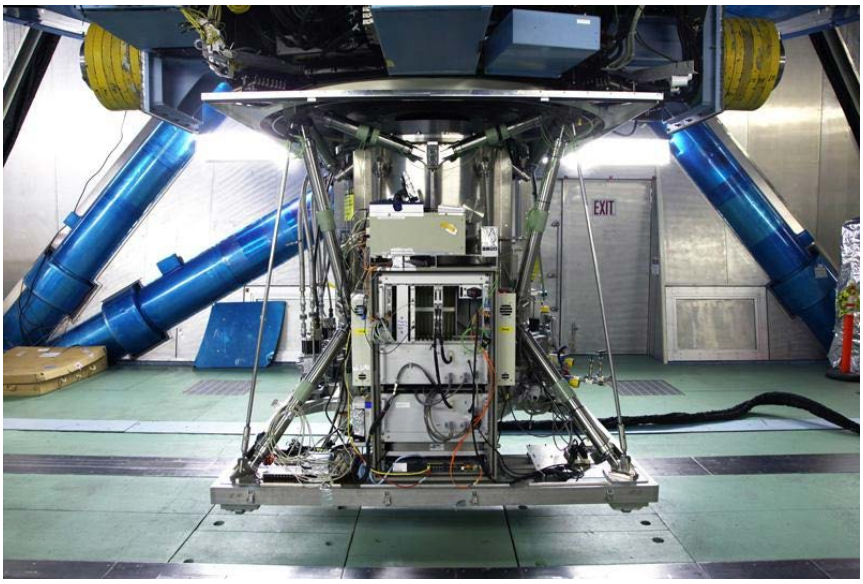

Figure C-8 : COMICS instrument in the Subaru telescope

C.4 The VLT & FORS2 Instrument

C.4.1 The Very Large Telescope

The **Very Large Telescope array (VLT)** is the world's most advanced optical instrument, consisting of four Unit Telescopes (UT1 to UT4) with main mirrors of 8.2m diameter and four movable 1.8m diameter Auxiliary Telescopes. The 8.2m diameter Unit Telescopes can also be used individually. With one such telescope, images of celestial objects as faint as magnitude 30 can be obtained in a one-hour exposure

C.4.2 VLT FORS2 Instrument

Figure C-9: FORS instrument in the Very Large Telescope. copyright : ESO

FORS2 – see Figure C-9 - is a multi-mode (imaging, polarimetry, long slit and multi-object spectroscopy) optical instrument mounted on the UT1 Cassegrain focus. FORS2 works in the wavelength range from 330 to 1100 nm. Two different magnifications is feasible to be used with pixel scales of 0.25"/pixel (for the Standard Resolution collimator) and 0.125"/pixel (for the High Resolution collimator). The corresponding field sizes are 6.8' x 6.8' and 4.25' x 4.25' respectively. The two different magnifications are chosen by selecting one of two different collimators, hence each magnification has to be calibrated independently.

FORS2 offers imaging with a wide range of broad- and narrow-band filters. The narrow-band filters are exchangeable and chosen from a large range available filters depending on the user-request.

Annex D

Bibliography

A'Hearn M.F., Feldman P.D. 1992, Water vaporization on Ceres, Icarus, 98:54–60.

A'Hearn M.F, Feaga L.M., Keller H.U., et al. 2012, Cometary volatiles and the origin of comets, ApJ, 758, 29.

Altwegg K., Balsiger H., Bar-Nun A., et al. 2015, 67P/Churyumov-Gerasimenko, a Jupiter family comet with a high D/H ratio, Science, 347, 27.

Altwegg, K., Balsiger, H., Hänni, N., et al. 2020, Evidence of ammonium salts in comet 67P as explanation for the nitrogen depletion in cometary comae, Nature Astronomy, 4, 533-540.

Auster, H.U., et al., 2007, ROMAP: Rosetta Magnetometer and Plasma Monitor, Space Sci Rev, 128, 221–240.

Beck, P., Quirico, E., Sevestre, D., et al. 2011, Ice vs. Goethite as the Origin of the 3 Micron Feature on Low Albedo Asteroids, 42nd LPSC, #2047, 2011.

Bibring, J.P., Langevin, Y., Carter, J., et al. 2015, 67P/Churyumov–Gerasimenko surface properties as derived from CIVA panoramic images, Science, 349.

Biele, J., et al. 2015, The landing(s) of Philae and inferences about comet surface mechanical properties. Science, 349.

Biver, N., Bockelée-Morvan, D., Colom, P., et al, 1997, Long-term Evolution of the Outgassing of Comet Hale-Bopp From Radio Observations, EM&P, 78, 5.

Biver, N., Bockelée-Morvan, D., Crovisier, J., et al. 2007, Submillimetre observations of comets with Odin: 2001-2005, PSS, 55, 1058-1068.

Biver, N., Szutowicz, S., Bockelée-Morvan, D., et al. 2010, Comet 10P/Tempel 2 Outgassing and Composition from Herschel and Ground-based Sub-millimeter Observation, BAAS, 42, 946.

Biver N, Crovisier J, Bockelée-Morvan D., et al. 2012, Ammonia and other parent molecules in comet 10P/Tempel 2 from Herschel/HIFI and ground-based radio observations, A&A, 539, A68.

Biver, N., Bockelée-Morvan, D., Morena, R., et al. 2015, Ethyl alcohol and sugar in comet C/2014 Q2 (Lovejoy), Sci. Adv., 1, 9, e1500863.

Bland, M.T., Buczkowski, D.L., Sizemore, H.G. et al. 2019, Dome formation on Ceres by Solid-State flow analogous to terrestrial salt tectonics, Nature Geoscience, 12, 797-801.

Blaney D. L. 1991, Infrared imaging of Mars between 2.4 microns and 5.0 microns (abstract). Lunar and Planetary Science XXII, pp. 111–112, Lunar and Planetary Institute, Houston.

Blum, J. et al. 2017, Evidence for the formation of comet 67P/Churyumov-Gerasimenko through gravitational collapse of a bound clump of pebbles, MNRAS, 469, S755-S773.

Bockelée-Morvan, D., Crovisier, J., Mumma, M.J., Weaver H.A., 2004, The composition of cometary volatiles. In: Festou M, Keller H, Weaver H (eds), Comets II, University of Arizona Press, Tucson, pp 391–423.

Bockelée-Morvan, D., 2008, Cometary science with ALMA, Astrophys Space Sci, 313:183–189.

Bodewits, D., Kelley, M.S., Li, J.Y., 2011, Collisional excavation of asteroid (596) Scheila, ApJ, 733, L3.

Bregman J. D., Tielens A. G. G. M., Witteborn F. C., et al. 1988, 3 micron spectrophotometry of Comet Halley: Evidence for water ice, ApJ, 334, 1044–1048.

Brooke, T. Y., Knacke R. F., Owen T. C., and Tokunaga A. T. 1989, Spectroscopy of emission features near 3 microns in Comet Wilson (1986l), ApJ, 336, 971–978.

Brown R. H., Cruikshank D. P., Pendleton Y. J., and Veeder G. J. 1997, Surface composition of Kuiper belt object 1993 SC. Science, 276, 937–939. 10.1126/science.276.5314.937

Brown, M.E. 2016, The 3–4 μm Spectra of Jupiter Trojan Asteroids, Astron. J., 152, 159.

Campins, H., Hargrove, K., Pinilla-Alonso, N. et al. 2010, Water ice and organics on the surface of the asteroid 24 Themis. Nature, 464:1320–1321.

Carry, B., Dumas, C., Fulchignoli, M., et al. 2008, Near-infrared mapping and physical properties of the dwarf-planet Ceres, A&A, 478, 235–244,

Cernicharo, J. & Crovisier, J., 2005, Water in space: the water world of ISO, Space Sci. Rev., 119, 29–69.

Clark, R.N & Roush, T.L., 1984, Determination of mineral abundance from reflectance spectra, Bulletin of American Astronomical Society, 16, 685.

Clark, R.N., 2009, Detection of adsorbed water and hydroxyl on the moon, Science, 326:562–564.

Colangeli, L., Epifani, E., Brucato, J.R., et al. 1999) Infrared spectral observations of comet 103P/Hartley 2 by ISOPHOT, A&A, 343, L87–L90.

Crovisier, J., Leech, K., Bockelée-Morvan, D., et al. 1997, The spectrum of comet Hale–Bopp (C/1995 01) observed with the infrared space observatory at 2.9 AU from the Sun, Science, 275, 1904–1907.

Crovisier, J., Colom, P., Biver, N., et al. 2013, Observations of the 18 cm OH lines of comet 103P/Hartley 2 at Nançay in support to the EPOXI and Herschel missions, Icarus, 222, 679–683.

Combe, J.Ph-, McCord, T.B., Tosi, F., et al. 2016, 47th Lunar and Planetary Science Conference, 1820.

Davidsson, B.J.R., Sierks, H., Güttler, C., et al. 2016, The primordial nucleus of comet 67P/Churyumov-Gerasimenko, A&A, 592.

Davies, J.K., Roush, T.L., Cruikshank, D.P., et al. 1997, The detection of water ice in comet Hale–Bopp. Icarus,127, 238–245.

De Graauw, T., Helmich, F. P., Phillips, T. G., et al. 2010, A&A, 518, L6.

Delsemme A. H., 2000, 1999 Kuiper prize lecture, Icarus, 146, 313–325.

De Sanctis, M.C., Capaccioni, F., Ciarniello, M., et al. 2015, The diurnal cycle of water ice on comet 67P/Churyumov–Gerasimenko. Nature, 525, 7570, 500–503.

De Sanctis, M.C., Ammannito, E., Raponi, A., et al. 2020, Fresh emplacement of hydrated sodium chloride on Ceres from ascending salty fluids, Nature Astronomy, 4, 786-793.

De Val-Borro, M., Hartogh, P., Crovisier, J., et al. 2010, Water production in comet 81P/Wild 2 as determined by Herschel HIFI, A&A, 521, L50.

De Val-Borro, M., Bockelée-Morvan, D., Jehin, E., et al. 2014, Herschel observations of gas and dust in comet C/2006 W3 (Christensen) at 5 AU from the Sun. A&A, 564, A124.

Dudal, C., & Loisel, C., 2016, Rosetta-Philae RF link, challenging communications from a comet, Acta Astron. 125, 137–148.

DuFresne, E. R. & Anders, E., 1962, On the chemical evolution of the carbonaceous chondrites, Geochim. Cosmochim. Acta, 26, 1084–1114.

Dumas, C., Carry, B., Hestroffer, D., & F. Merlin, F. 2011, High-contrast observations of (136108) Haumea. A&A, 528: A105.

Encrenaz T., Drossart P., Feuchtgruber H., 1999, The atmospheric composition and structure of Jupiter and Saturn from ISO observations; A preliminary review, Planet. Space Sci., 47, 1225–1242.

Fanale, F.P., & Salvail, J.R. 1989, The water regime of asteroid (1) Ceres, Icarus, 82, 97-110.

Feaga, L.M., A'Hearn, M.F., Farnham, T.L., et al. 2014, Uncorrelated volatile behavior during the 2011 apparition of comet C/2009 P1 Garradd, Astron. J, 147, 24.

Feierberg M. A., Lebofsky L. A., and Larson H. P., 1981, Spectroscopic evidence for aqueous alteration products on the surfaces of low-albedo asteroids, Geochim. Cosmochim. Acta, 45, 971–981.

Feldman, P.D., A'Hearn, M.F., Bertaux, J.L., et al. 2015, Measurements of the near-nucleus coma of comet 67P/Churyumov-Gerasimenko with the Alice far-ultraviolet spectrograph on Rosetta, A&A, 583, A8.

Florczak M., Lazzaro D., Mothé-Diniz T., et al. 1999, A spectroscopic study of the Themis family, A&A, Suppl. Ser., 134, 463–471.

Fornasier, S., Lazzarin, M., Barbieri, C., et al. 1999, Spectroscopic comparison of aqueous altered asteroids with CM2carbonaceous chondrite meteorites, A&A, Suppl. Ser., 135, 65-73.

Gomes, R., Levison, H.F., Tsiganis, K., et al. 2005, Origin of the cataclysmic late Heavy Bombardment Period of the terrestrial planets, Nature, 435, 466–469.

Grundy, W.M., & Schmitt, B. 1998, The temperature-dependent near-infrared absorption spectrum of hexagonal H2O ice, Journal Geophys. Res., 103, 25, 809–25, 822.

Glassmeier, K., Boenhardt, H., Koschny, D., et al. 2007, The Rosetta Mission: Flying Towards the Origin of the Solar System, Space Sci. Rev., 128, 1–21.

Hartogh, P., Crovisier, J., de Val-Borro, M., et al. 2010, HIFI observations of water in the atmosphere of comet C/2008 Q3 (Garradd), A&A, 518, L150.

Hartogh, P., Lis, D. C., Bockelée-Morvan, D., et al. 2011, Ocean-like water in the Jupiter-family comet 103P/Hartley 2, Nature, 478, 218.

Hasegawa, S., Murakawa, K., Ishiguro, M., et al. 2003, Evidence of hydrated and/or hydroxylated minerals on the surface of asteroid 4 Vesta, Geophys. Research Letters, 30, 21.

Herique, A., Kofman, W., Zine, S., et al. 2019, Homogeneity of 67P/Churyumov-Gerasimenko as seen by CONSERT: implication on composition and formation, A&A, 630, A6.

Hsieh, H.H., & Jewitt, D. 2006, A population of comets in the main asteroid belt, Science, 312, 561–563.

Hsieh, H.H., Novakovic, B., Kim, Y. et al, 2018, Asteroid Family Associations of Active Asteroids, Astron. J., 155, 2, 96.

Hui, M.T., & Jewitt, D. 2017, Non-gravitational acceleration of the active asteroids. Astron. J, 153, 80.

Jewitt, D., Weaver, H., Mutchler, M., et al. 2011, Hubble space telescope observations of Main-Belt Comet (596) Scheila, ApJ, 733, L4.

Jewitt, D., Kim, Y., Luu, J., et al. 2019a, Episodically Active Asteroid 6478 Gault, ApJ Letters, 876:L19.

Jewitt, D., Kim, Y., Rajagopal, J. et al. 2019b, Active Asteroid P/2017 S5 (ATLAS), ApJ, 157:54.

Jia, Y.-D., Villarreal, M. N., & Russell, C. T. 2017, Possible Ceres Bow shock surfaces based on fluid models, J. Geophys. Res. Space Phys.,122, 4976.

Landis, M.E., Byrne, S., Combe, J.Ph-, et al. 2019, Water vapour contribution to Ceres' exosphere from observed surface ice and postulated ice-exposing impacts, JGR Planets, 124, 1, 61-75.

Larson H. P., Fink U., Treffers R., and Gautier T. N. 1975, Detection of water vapor on Jupiter. ApJ Letters, 197, L137–L140.

Levison, H.F., Bottke, W.F., Gounelle, M., et al. 2009, Contamination of the asteroid belt by primordial trans-Neptunian objects, Nature, 460, 364–366.

Kawakita, H., Watanabe, Ji., Ootsubo, T., et al. 2004, Evidence of icy grains in comet C/2002 T7 (LINEAR) at 3.52 au, ApJ, 601, L191–L194.

Keller, H.U., Barbieri, C., Lamy, P., et al. 2007, OSIRIS – The scientific camera system onboard Rosetta, Space Science Rev., 128, pp. 433-506.

Kataza, H., Okamoto, Y., Takubo, S., et al. 2000, Proc. SPIE, 4008, 1144.

King, T.V.V., Clark, R.N., Calvin, W.M., et al. 1992, Science, 255, 5051, 1551-1553.

Küppers, M, O'Rourke, L, Bockelée-Morvan, D, et al. 2014, Localized sources of water vapour on the dwarf planet (1) Ceres, Nature, 505, 525–527.

Kofman, W., Herique, A., Barbin, Y., et al. 2015, Properties of the 67P/Churyumov-Gerasimenko interior revealed by CONSERT radar, Science, 349.

Lebofsky L. A. 1978, Asteroid 1 Ceres: Evidence for water of hydration. Monthly Notices Royal Astron. Soc., 182, 17–21.

Licandro, J., Campins, H., Kelley, M., et al. 2011, (65) Cybele: detection of small silicate grains, water-ice, and organics, A&A, 525, A34.

Lomb, N. R. 1976, Least-squares frequency analysis of unequally spaced data, Ap&SS, 39, 447.

Mainzer, A., Grav, T., Masiero, J., et al. 2011, Thermal Model Calibration for Minor Planets Observed with WISE/NEOWISE, ApJ, 737, 1.

Meech, K. and Raymond, S. 2020, Searching for the Origin of Earth's Water, in: Planetary Astrobiology, ed. V. Meadows, G. Arney, B. Schmidt, D. J. DesMarais, p. 325, 2020.

McCord T. B., Hansen G. B., Matson D. L., et al. 1999, Hydrated salt minerals on Europa's surface from the Galileo near-infrared mapping spectrometer (NIMS) investigation, J. Geophys. Res., 104, 11827–11852.

Morbidelli, A., Chambers, J., Lunine, J.I., et al. 2000, Source regions and time scales for the delivery of water to Earth, Meteorite Planet Sci, 35, 1309–1320.

Morbidelli, A., Levison, H.F., Tsiganis, K. & Gomes, R. et al. 2005, Chaotic capture of Jupiter's Trojan asteroids in the early solar system, Nature, 435, 7041, 462-5.

Morbidelli, A., Bottke, W. F., Nesvorný, D., & Levison, H. F. 2009. Asteroids were born big, Icarus, 204, 2, 558–573.

Morbidelli A. 2013, Dynamical Evolution of Planetary Systems, Oswalt T.D., French L.M., Kalas P. (eds) Planets, Stars and Stellar Systems, Springer, Dordrecht.

Moreno, F., Licandro, J., Cabrera-Lavers, A. 2012, A short-duration event as the cause of dust ejection from Main-Belt Comet P/2012 F5 (Gibbs), ApJ, 761, L12.

Moreno, F., Pozuelos, F.J., Novakovíc, B., et al. 2017, The splitting of double-component active asteroid P/2016 J1 (PANSTARRS). ApJ, 837, L3.

Mckay, A.J., Bodewits, D., & Jian-Yang, L. 2017, Observational constraints on water sublimation from 24 Themis and 1 Ceres, Icarus, 286, 308–313.

McKenna-Lawlor, S., Rusznyak, P., Balaz, J., et al. 2016, Performance of the mission critical Electrical Support System (ESS) which handled communications and data transfer between the Rosetta Orbiter and its Lander Philae while en route to and at comet 67P/Churyumov-Gerasimenko, Acta Astron., Vol. 125, pp. 118-136.

Mukai, T. 1986, Analysis of a dirty water–ice model for cometary dust, A&A, 164, 397–407.

Nesvorrný, D., Bottke, W.F., Levison, H.F. et al. 2003, Recent origin of the Solar System Dust bands, ApJ, 591, 1, 486.

Ootsubo, T., Kawakita, H., Hamada, S., et al. 2012, AKARI near-infrared spectroscopic survey for CO2 in 18 comets. ApJ, 752, 15.

O'Rourke, L., Snodgrass, C., de Val-Borro, M., et al. 2013a, Determination of an upper limit for the water outgassing rate of Main-Belt Comet P/2012 T1 (PANSTARRS). ApJ, 774, L13.

O'Rourke, L., Bockelée-Morvan, D., Biver, N., et al. 2013b, Herschel and IRAM-30m observations of comet C/2012 S1 (ISON) at 4.5AU from the Sun, A&A, 560, A101.

O'Rourke, L., Tubiana, C., Güttler, C., et al. 2019, The search campaign to identify and image the Philae Lander on the surface of comet 67P/Churyumov-Gerasimenko, Acta Astronautica, 157, 199-214.

O'Rourke, L., Heinisch, P., Blum, J., et al. 2020a, The Philae lander reveals low strength primitive ice inside cometary boulder, Nature, 586, 697-701

O'Rourke, L., Müller, T.G., Biver, N., et al. 2020b, Low Water outgassing from (24) Themis and (65) Cybele – 3.1 µm NIR spectra implications, ApJ Letters, 898, 2.

Ott, S. 2010, The Herschel Interactive Pipeline (HIPE), ASP Conf. Ser. 434, Astronomical Data Analysis Software and Systems XIX, ed. Y. Mizumoto, K.-I. Morita, & M. Ohishi , San Francisco, CA: ASP, 139.

Petrenko, V.F., & Whitworth, R.W. 1999, Physics of ice. Oxford University Press, Oxford.

Piani, L., Marrocchi, Y., Rigaudier, T., et al. 2020, Earth's water may have been inherited from material similar to enstatite chondrite meteorites, Science, 369, 1110.

Pieters, C.M., Goswami, J.N., Clark, R.N., et al. 2009, Character and spatial distribution of OH/H2O on the surface of the moon seen by M3 on Chandrayaan-1, Science, 326, 568.

Pilbratt, G. L., Riedinger, J. R., Passvogel, T., et al. 2010, Herschel Space Observatory, A&A, 518, L1.

Poch, O., Istiqomah, I., Quirico, E., et al. 2020, Ammonium salts are a reservoir of nitrogen on a cometary nucleus and possibly on some asteroids, Science, 367, 7462.

Prettyman, T.H., Mittlefehldt, D.W., Yamashita, N., et al. 2012, Elemental Mapping by Dawn Reveals Exogenic H in Vesta's Regolith, Science, 338, 6104.

Prettyman, T.H., Yamashita, N., Toplis, M.J., et al. 2017, Extensive water ice within Ceres' aqueously altered regolith: evidence from nuclear spectroscopy, Science, 355, 55–59.

Prialnik, D., & Rosenberg, E. D. 2009, Can ice survive in main-belt comets? Long-term evolution models of comet 133P/Elst-Pizarro, MNRAS, 399, L79.

Protopapa, S., Sunshine, J.M., Feaga, L.M., et al. 2014, Water ice and dust in the innermost coma of comet 103P/Hartley 2, Icarus, 238, 191–204.

Reddy, V., Le Corre, L., O'Brien, D.P. et al. 2012, Delivery of dark material to Vesta via carbonaceous chondritic impacts, Icarus, 221, 2, 544.

Rivkin, A. S., Volquardsen, E. L., & Clark, B. E. 2006, The surface composition of Ceres: Discovery of carbonates and iron-rich clays, Icarus, 185, 563–567.

Rivkin, A.S., & Emery, J.P. 2010, Detection of ice and organics on an asteroidal surface, Nature, 464, 1322–1323.

Rivkin, A.S., Campins, H., Emery, J.P., et al. 2015, Astronomical observations of volatiles on asteroids. Space Science Series Book: Asteroids IV, 65–87.

Rivkin, A.S., Howell, E.S., Emery, J.P., Sunshine, J. 2017, Evidence for OH or H2O on the surface of 433 Eros and 1036 Ganymed, Icarus, 235-253.

Roth, L. 2018, Constraints on water vapor and sulfur dioxide at Ceres: Exploiting the sensitivity of the Hubble Space Telescope, Icarus, 305, 149.

Roth, L., Ivchenko, N., Retherford, K. D., et al. 2016, Constraints on an exosphere at Ceres from Hubble Space Telescope observations, Geophys. Res. Lett., 43, 2465.

Rousselot, P., Jehin, E., Manfroid, J., et al. 2011, A search for water vaporization on Ceres, Astron. J., 142,125.

Rousselot, P., Optimom, C., Jehin, E., et al. 2019, Search for water outgassing of (1) Ceres near perihelion, A&A, 628, A22.

Ruesch, O., Platz, T., Schenk, P., et al. 2016, "Cryovolcanism on Ceres", Science, 353, 428.

Scargle, J. D. 1982, Studies in astronomical time series analysis. II. Statistical aspects of spectral analysis of unevenly spaced data, ApJ, 263, 835.

Schorghofer, N., Byrne, S., Landis, M. E., et al. 2017, The putative Cerean exosphere, ApJ, 850, 85.

Philae initial scientific results, Science Special issue, 2015, Issue 349, 6247.

Sinton W. M. 1967, On the composition of Martian surface materials. Icarus, 6, 222–228.

Snodgrass, C., Agarwal, J., Combi, M. et al. 2017, The Main Belt Comets and ice in the Solar System, A&A Review, 25, 5.

Snodgrass, C., Yang, B., Fitzsimmons, A., 2017, X-shooter search for outgassing from main belt comet P/2012 T1 (Pan-STARRS), A&A, 605, A56.

Stevenson, R, Kramer, EA, Bauer, JM, et al. 2012, Characterization of active main belt object P/2012 F5 (Gibbs): a possible impacted asteroid, ApJ, 759, 142.

Su K Y.L, Rieke, G.H., Malhotra, R., et al. 2013, Asteroid belts in Debris Disk twins : VEGA and Fomalhaut, ApJ, 763, 11.

Sunshine, J.M., A'Hearn, M.F., Groussin, O., et al. 2006, Exposed water ice deposits on the surface of Comet 9P/Tempel 1, Science, 311, 1453–1455.

Sunshine, J.M., Farnham, T.L., Feaga, LM., et al. 2009, Temporal and spatial variability of lunar hydration as observed by the deep impact spacecraft, Science, 326, 565.

Swings, P., Elvey, C.T., Babcock, H.W. 1941, The spectrum of comet Cunningham, 1940C, ApJ, 94, 320.

Takir, D., & Emery, J.P. 2012, Outer main belt asteroids: identification and distribution of four 3 μm spectral groups, Icarus, 219, 641–654.

Takir, D., Reddy, V., Sanchez, J.A., et al. 2017, Detection of water and/or hydroxyl on asteroid (16) Psyche, Astron J., 153, 31.

Usui, F., Hasegawa, S., Ootsubo, T., et al. 2019, PASJ, 714, 1.

Ulamec, S., Biele, J., Blazquez, A., et al. 2015, Rosetta Lander – Philae: landing preparations, Acta Astron., Vol. 107, pp. 79-86.

Villareal, M. N., Russell, C. T., Luhmann, J. G., Thompson, W. T., Prettyman, T. H., A'Hearn, M. F., Küppers, M., O'Rourke, L., & Raymond, C. A. 2017, The dependence of the Cerean exosphere on solar energetic particle events. ApJ Letters, 833, L8.

Walsh, K., J., Morbidelli, A., Raymond, S. N., et al. 2011, Low mass for Mars from Jupiter's early gas-driven migration, Nature, 475, 206–209.

Yang, B., & Jewitt, D. 2010, Identification of Magnetite in B-Type Asteroids. Astron. J., 140, 692-698.

Yang, B., Jewitt, D, Bus, S.J. 2009, Comet 17P/Holmes in outburst: the near infrared spectrum, Astron. J., 137, 4538–4546.

Yang, B., Keane, J., Meech, K., et al. 2014, Multi-wavelength observations of comet C/2011 L4 (Pan-STARRS), ApJ, 784, L23.

Zhang, X., Huang, J., Wang, T. and Zhuoxi, H. 2019, Zhenghe-A mission to a Near-Earth Asteroid and a Main-belt comet, LPSC, 2132, 1045.

Annex E

List of Publications

Müller, T.G., O'Rourke, L., Barucci, A.M., et al. 2012, Physical Properties of OSIRIS-REx Target Asteroid (101955) 1999 RQ36 derived from Herschel, ESO-VISIR and Spitzer observations, A&A, 548, A36.

O'Rourke, L., Müller, T.G., Valtchanov, I., et al. 2012, Thermal and shape properties of asteroid (21) Lutetia from Herschel observations around the Rosetta flyby, Planetary and Space Science, 66, 192–199.

O'Rourke, L., Snodgrass, C., de Val-Borro, M., et al. 2013a, Determination of an upper limit for the water outgassing rate of Main-Belt Comet P/2012 T1 (PANSTARRS). ApJ, 774, L13.

O'Rourke, L., Bockelée-Morvan, D., Biver, N., et al. 2013b, Herschel and IRAM-30m observations of comet C/2012 S1 (ISON) at 4.5AU from the Sun, A&A, 560, A101.

Küppers, M, O'Rourke, L, Bockelée-Morvan, D, et al. 2014, Localized sources of water vapour on the dwarf planet (1) Ceres, Nature, 505, 525–527.

Villareal, M. N., Russell, C. T., Luhmann, J. G., Thompson, W. T., Prettyman, T. H., A'Hearn, M. F., Küppers, M., O'Rourke, L., & Raymond, C. A. 2017, The dependence of the Cerean exosphere on solar energetic particle events, ApJL, 833, L8.

O'Rourke, L., Tubiana, C., Güttler, C., et al. 2019, The search campaign to identify and image the Philae Lander on the surface of comet 67P/Churyumov-Gerasimenko, Acta Astronautica, 157, 199-214.

O'Rourke, L., Heinisch, P., Blum, J., et al. 2020a, The Philae lander reveals low strength primitive ice inside cometary boulder, Nature, 586, 697-901

O'Rourke, L., Müller, T.G., Biver, N., et al. 2020b, Low Water outgassing from (24) Themis and (65) Cybele – 3.1 µm NIR spectra implications, ApJL, 898, 2, L45.

Annex F

Supplementary Methods & Figures of Chapter 2

The following represents an extract taken from the Supplementary methods document that accompanies the Nature paper. As the document contains over 95 pages, I extracted specific sections I believe will be important for readers of this thesis. I also provide the Supplementary Figures that are referred to in the Nature paper itself.

F1. OSIRIS Supplementary supporting information

The NAC camera of the OSIRIS imaging system onboard Rosetta imaged the boulder and surroundings regions pre- and post- landing in 2014. The pre-landing color images were acquired at relatively low resolution, on 2 September (11 filters, 0.97 m/px) and 15 September (5 filters, 0.52 m/px), see Extended Data Fig. 2a and b. Post-landing images at 0.34-0.36 m/px resolution were acquired first on 6-14 December (Extended Data Fig. 2c, d and e) , with no clear evidence of bright spots on the skull boulder, possibly because the observing geometry was not favorable to see the crevice generated by Philae. A few bright patches were also visible in these image sequences, and they were located at a distance ~50-60 m from the skull boulder.

During the Rosetta mission extended phase in 2016, the crevice of the skull boulder was first observed in March (Extended Data Fig. 6h and i) and early May at resolution 0.34-0.19 m/px with two color filters (blue and orange), during which one side of the boulder was in shadows and no evidence of exposure of volatiles was found. The boulder was captured at high spatial resolution with 3 filters covering the 360-649 nm range on 25 May (0.10 m/px) and 1 June (0.14 m/px) (Extended Data Fig.2j), with materials inside the crevice that was approximately 1.6 times brighter than the reference dark terrain and had a red spectra similar to the surroundings.

Starting from 12 to 14 June 2016 (observations available with 3 filters in the 480-882 nm range, res 0.50 m/px) a bright spot of exposed volatiles was observable on the Skull boulder, inside the crevice generated by Philae ((Extended Data Fig. 2 j, k, l and m). Its normal albedo is estimated to be up to 46% (Fig. 3a, and it covers an area of 3.5 m^2. The spectral modelling of these bright spots made by areal mixture of the cometary dark terrain and water ice indicate a local water ice abundance up to 46.4% (Extended Data Table 1).

The dust to ice ratio varies from 1.07 to 1.25 for water ice abundance of 48.4% and 44.4 %, respectively, with the value of $1.15^{+0.1}_{-0.08}$ for water ice abundance of 46.4.%. By assuming a dust to ice bulk density ratio of two[17], and a similar porosity for dust and ice material, we derive a local dust/ice mass ratio of $2.3^{+0.2}_{-0.16}$: 1 for the water ice abundance listed in Extended Data Table 1.

Later images acquired in September 2016, before the end of the Rosetta mission, indicate that the bright

patch inside the skull boulder crevice was still present, indicating an exposure of water ice for several months. Those images, however, were acquired with a single filter, and no color sequence was available for an estimation of the local water ice content. The fact that fresh water ice is observed in the new formed crevice supports previous observations that water ice is abundant just beneath the surface[21] as well as observations on other comets[7]. Other evidence of freshly exposed water ice were found in comet 67P in case of cliff collapse[4], in new scarps formed by collapse and cometary activity[5,53].

F2. ROMAP/RPC-MAG detailed analysis describing Philae's flight through TD2

ROMAP and RPC-MAG concurrent observations: A combination of magnetic field measurements of the ROMAP instrument and Rosetta RPC-MAG observations were used to reconstruct the lander dynamics. Extended Data Fig. 5 shows the three components of the magnetic field observations starting before TD2 at 17:23:00 UTC and ending shortly after the boom movement was detected. This figure also shows the concurrent orbiter RPC-MAG observations as reference.

The magnetometer boom is only supported in its nominal position by springs and not locked, leading to a rotational degree of freedom along the lander y-axis[13]. A detailed description of the mechanical properties of the mounting mechanism is given by Heinisch et al[56]. Hence, acceleration of the lander body along the z-axis causes a deflection of the boom, due to the inertia of the boom and sensors assembly. This displacement of the sensor relative to its nominal positions creates a change in the observed magnetic field due to the relatively strong magnetic bias field of the lander[13]. These characteristic changes create a specific pattern of spikes in the three components of the magnetic field observations and have been described by Heinisch et al[56] in detail and were also used in the analysis of the other touchdowns[1,11]. The duration of the acceleration can easily be determined by the length of this signature and the direction of the boom movement (i.e. sign of the acceleration vector) can be determined by the sign of the individual magnetic field spikes in the 3D magnetic field observations (see Fig. 4.4 in [56]).

Due to the complex and inhomogeneous nature of the lander bias field, which is influenced not only by the lander operations but also superimposed by the background magnetic field, the 1 Hz temporal resolution of the magnetic field observations does not provide enough detail to derive the deflection angle of the boom directly from the observed spikes. Therefore, only a qualitative estimation of the magnitude of the acceleration causing the boom deflection relative to the other touchdown events is possible.

The estimates of kinetic energy, velocity, contact time and energy loss described in the following pages are summarised in Extended Data Table 2. It is important to flag that Philae had no attitude control capabilities during its flight across the surface.

Touchdown point – TD2a – Initial touchdown : Initially Philae was rotating with (42.0±1.0) mHz and had an initial total kinetic energy[11] of (2.97±0.15) J. Similar to the collision with the rim of the Hatmehit crater at 16:20 UTC, between 17:23:48±10s and 17:24:22±1s UTC the rotation pattern changed and in contrast to the previous contacts and the final touchdown no significant boom signature was detected. Hence, no significant acceleration along the lander z-axis was present during this contact (TD2a). Additionally, the axis of rotation tilted by approximately 120° around the lander z-axis and 30° around the lander y-axis. The rotation frequency increased from (42.0±1.0) mHz to (64.0±1.0) mHz. The angular velocity and rotation axis orientation were determined based on the methods explained by[12].

For a rigid body only influenced by gravity an increase in angular velocity and a change in the rotation axis orientation can only be caused by an interaction with the surface, as external forces are required. The most likely site of this collision (TD2a) was identified on OSIRIS images as shown in Supplementary Fig. 5 (point 1), in Supplementary Video 3, and Supplementary Fig. 6 right hand image. This site was identified in the TD2 region using before and after images, which showed a change in the local surface features. A groove-like crater approximately (1.92 ± 0.24) m in length and a width of (1.53 ± 0.24) m was created by the impact of Philae.

Based on the change in rotation rate, the rotational energy $E_{rot} = 2\pi^2 {f_{rot}}^2 I$, where f_{rot} is the rotation frequency and $I = 16.6$ kgm² is the corresponding moment of inertia, increased from (0.578±0.028) J to (1.342±0.042) J. This increase of approximately 0.764 J in rotational energy was caused by the transformation of translational kinetic energy into rotational energy during the ground contact. This behavior can be explained by the landing gear hitting the surface at an oblique angle, acting as a lever to pivot Philae and thereby converting forward velocity into rotation.

As this contact was inelastic, most of this energy was dissipated by compressing the surface at the contact area, while some of the energy could have also been dissipated inside the landing gear structure. Due to the geometry of the contact, the landing gear damper did not contribute to the energy loss, as it only acts in the lander z-direction.

Touchdown point - TD2b – Dust wall creation : The analysis of the rotational signature in the magnetic field showed, that the rotation rate changed again between 17:24:53±1s UTC and 17:24:57±1s UTC dropping from (64.0±1.0) mHz to (28±1.0) mHz with a corresponding rotational energy of (0.257±0.018) J. The OSIRIS images show a dust wall (extending along the crevice) in the flight path of Philae, at a distance of (3.37±0.32) m, the relative difference in height is (1.19±0.24) m. See Supplementary Fig. 5 (TD2b), Supplementary Video 3, the dust wall animation in Supplementary Video 4, Supplementary Fig. 6 right hand image (blue arrow).

Based on the analysis of the ROMAP observations i.e. the timing of the changes in rotation rate, the flight time between the initial contact at TD2a and the dust wall (TD2b) was determined to be (31±1) s (17:24:22±1s until 17:24:53±1s UTC). This results in a horizontal velocity relative to the surface of $v_h =$ (0.109±0.011) m/s and a relative vertical velocity of $v_v =$ (0.034±0.008) m/s. The total kinetic energy $E_{kin} = \frac{1}{2}mv^2$, where m=97 kg is the mass of Philae and $v = \sqrt{{v_h}^2 + {v_v}^2}$ is the total velocity, is (0.632±0.138) J. Combined with the rotational energy of (1.342±0.042) J, this results in a total energy after the initial TD2a of (1.974±0.18) J, which translates to a loss of approximately 33% or (0.996±0.33) J during the initial contact at TD2a.

After hitting the dust wall during TD2b Philae continued for an additional (30±1) s and (3.76±0.23) m in horizontal direction and only approximately (0.50±0.18) m in vertical direction, until 17:25:24 UTC at which point the next boom movement was detected (TD2c). This translates to a horizontal velocity of

(0.125±0.013) m/s, a vertical velocity of (0.017±0.006) m/s and a kinetic energy of (0.771±0.179) J. Combined with the rotational energy this results in a total kinetic energy before TD2c and after the dust wall was hit at TD2b of (1.028±0.197) J. In total the contact with the dust wall prior to TD2c dissipated (0.817±0.377) J of the kinetic energy of the lander.

The increase in velocity after the dust wall was hit compared to after TD2a is consistent with torque created by the fast-rotating lander hitting the dust wall with one of the feet. While the drag created by the foot slowed down the rotation, it also accelerated the lander forward relative to the surface explaining the increase in velocity.

The Philae lander proceeded down the length of the crevice creating the dust wall for the entire length. The crevice narrows at the end and it is believed that it is because of this narrowing (down to a width of 0.99m) that Philae stopped its motion down the crevice and changed direction. The angle of the overhang will also have contributed to the change in direction.

Touchdown point – TD2c – Stamping/compression of water ice : The ROMAP boom showed another movement at 17:25:24±1s and this acceleration continues until approximately 17:25:27±1s during which the boom was moving upwards. Afterwards the boom started to move downwards away from the lid, which means the acceleration of the lander stopped or reversed. The change at 17:25:27±1s is considered the end point of the stamping because the geometry from the deceleration of Philae during stamping causes an upwards deflection of the boom which is what was observed. This resulted in a duration of 3±1s for the stamping/compression of the ice (see Fig. 1c and d).

The outgoing horizontal velocity is estimated to be zero as the stamping stopped the forward motion. The outgoing vertical velocity after the stamping is estimated to have a lower bound of (0.073±0.01) m/s while the energy loss at TD2c caused by the stamping is estimated to be (0.671±0.297) J. The calculation of these values stems from what occurred after TD2c namely the rotation of Philae out of the crevice on its way to TD2d.

Rotation of Philae out of the Crevice : With clear imprints visible in the images, it is believed that at 17:25:27±1s Philae started to roll out of the crevice, pivoting around the main lander body causing a rotation of approximately 60°. Such a rotation would normally cause a characteristic signature in the magnetic field however as this rotation coincided with the boom movement no such signature is visible compared to the RPC-MAG orbiter observations.

The compressed ice wall itself is angled upwards by 10 degrees. The fall of Philae towards the wall combined with the angle of the wall is believed to be the reason that the rotation began after the compression/stamping took place. Philae will have started to rise and rotate at the same time. There is no

evidence of ploughing i.e. a vertical rise, as we would have seen the SD2 drill cover creating a longer hole in the ice, which we do not see.

To roll out of the crevice more than half of the Lander body would have needed to be above the crevice wall. This is confirmed by the measurements obtained from the OSIRIS images which has approximately 0.20m of the Philae balcony rising above the crevice when the stamping occurs. This required Philae to rise a vertical distance of (0.22±0.025) m from the position of stamping as part of the actual rotation taking place.

From 17:25:27±1s until 17:25:30±1s, the boom is observed to move back down relatively freely after the stamping had completed. At 17:25:30+/- 1s, we see another abrupt change in direction of the boom which we believe is due to one of Philae's feet touching the skull-top-hat boulder during the rotation. The ROMAP sensor and boom entered the dust wall at the top of the crevice also at this time.

The constraint that Philae had to move approximately (0.22±0.025) m to reach the top of the crevice once the stamping completed at 17:25:27, as well as the changes in the boom state at 17:25:30, serves to provide us with an approximate duration of (3±1) s for this set of movements. This duration leads to a lower bound of (0.073±0.01) m/s for a theoretical average vertical velocity relative to the bottom of the crevice during this part of the rotation. As regards the rotation itself, we believe it had a maximum duration of (5±1)s leading to a rotation frequency of (33±5) mHz and a rotational energy of (0.357±0.1) J. This is consistent with a significant part of the translational kinetic energy being converted into rotational energy and translates to an energy loss during TD2c of (0.671±0.297) J.

As there were two legs sticking out of the crevice during the stamping event, these will not have collided with the boulders during the rotation that followed. However, the third leg which was fully inside and located at the base of the crevice will have touched the skull-top-hat boulder during the rotation out of the crevice. We find evidence of a possible indentation in the skull-top hat boulder which is believed to have been created by the foot of the lander on its exit from the crevice. The distance measured from start of the TD2d impression to the crevice also confirms the feasibility of a collision event. It is this collision of the foot with the boulder which we believe changes the boom direction at 17:25:30+/- 1s.

Further to this, between TD2b and TD2c, as Philae travelled along the crevice it created a dust wall along its entire length. However, in the imagery, the fact that this dust wall is not present directly above the location where Philae compressed the ice can be perfectly explained by Philae rotating out of the crevice and pushing through the dust wall at that location. Based upon the position of the ROMAP boom when Philae will have rotated out of the crevice, it will most certainly also have passed through and removed the dust wall during its transition across it. The distance measurements confirm this. We believe that the ROMAP boom enters the dust wall at the top of the crevice around the time period of 17:25:30+/-1s and is covered by dust. This is consistent with data from the ROMAP sensor itself which nominally provided science data integrated over 32 seconds but as of 17:32:35+/-1s the first packet received showed no further counts. In Heinisch et al[12],

it is stated that the only reason that no data could be received was due to the ROMAP SPM sensor getting completely covered by dust.

Touchdown TD2d – skull-face dust compression : The reaction of the boom beyond 17:25:30±1s taking into account that the dust itself will act as a damping force to the boom and will also hide other shocks to the system, makes further analysis difficult. The touch of the Philae foot to the skull-top-hat boulder during the rotation out of the crevice changed the upward velocity direction of Philae to point it slightly downward once more leading to the Philae balcony compressing the dust on the skull face boulder region (see Supplementary Video 3, Supplementary Fig. 3, Supplementary Fig. 6 central image). After this compression which we believe lasted a maximum duration of 2 ±1s, Philae continued with its rotation away from skull-top ridge. Based on Heinisch et al.[11] the total kinetic energy of Philae directly before TD3 was (0.10±0.02) J. As 0.928 J were dissipated during TD2c and TD2d and the energy loss during TD2c was estimated to be (0.671±0.297) J, the remaining energy lost at TD2d is estimated to be (0.257±0.12) J

F3. Porosity of cometery boulder ice - Supplementary information

Hierarchical arrangement of building blocks inside the comet nucleus and the boulder : We assume that the comet nucleus consists of solid particles in the sub-μm size range[28,29], which form larger porous aggregates ("pebbles"). These pebbles are clustered together, which leaves void spaces between the pebbles. If the comet nucleus is a collisional rubble pile, larger clusters of pebbles may be packed together with additional void spaces between the clusters. Thus, the overall filling factor of the comet nucleus in this three-level hierarchical arrangement is given by:

$$\Phi_{\text{nucleus}} = \Phi_{\text{pebble}} \cdot \Phi_{\text{cluster}} \cdot \Phi_{\text{rp}}$$

Equation (3)

with Φ_{pebble}, Φ_{cluster} and Φ_{rp} being the filling factors of the dust grains inside the pebbles, of the pebbles inside the clusters and of the clusters inside the rubble pile. Estimates of the radii of the pebbles have been made based upon a multi-Rosetta instrument approach[45] and thermal modelling[57] finding values between a few millimetres and one decimetre. The cluster sizes are less constrained, but analyses of the Rosetta Consert experiment show that they have to be smaller than approximately 1 meter in radius[3,24]. As the size of the boulder that Philae compressed has a height of ~2.3m, a width of ~2.5m and a length of ~5.5 m, Philae compacted therefore a volume in which potentially all hierarchical levels should be present meaning that the boulder could be considered to be representative of the bulk cometary material. As there is a lack of direct evidence however for the existence of the pebble clusters, we use as the nominal model for the setup of the comet nucleus a two-stage hierarchical model whose filling factor is given by $\Phi_{\text{nucleus}} = \Phi_{\text{pebble}} \cdot \Phi_{\text{cluster}}$.

Examples of how pebble assemblage can compact when boulder interior is formed (from Methods) : To estimate the volume filling factor Φ_{cluster}, we take into account the manner in which the pebbles assemblage compacts when the boulder interior is formed.

If the deposition velocity of the pebbles is smaller than the threshold velocity for sticking (e.g., Random Ballistic Deposition, RBD), a body with high-porosity is formed. Experiments and numerical simulations have shown[27,58] that the volume filling factor in this case is in the range $\Phi_{\text{cluster}} \approx 0.07 - 0.15$. However, due to the macroscopic size of the pebbles in the mm-dm range[45,57] and taking into account the following possible (non-exhaustive) list of modes of formation of the cometary nucleus or surface:

- the gravitational re-accumulation of debris after a sub-catastrophic collision
- the fallback of pebbles stemming from active areas elsewhere on the comet
- the gravitational collapse of a pebble cloud at formation,

the expected deposition speed is a substantial part of the gravitational escape speed ($\sim$ 1 m/s) and exceeds the sticking threshold of $< 10^{-3}$ m/s so that much denser configurations than RBD are expected.

Due to the dominance of the gravitational attraction of the forming body of at least a few km in size over the inter-particle forces of pebbles moving towards the comet nucleus at speeds exceeding the sticking threshold during their deposition, random loose packing (RLP[51]) can be expected if no additional vibrational motion of the granular assembly is present[59]. However, the volume filling factor of packed granular media heavily depends on the shape and size distribution of the pebbles as well as on the mode of formation and post-formation treatment. As a rule, the filling factor in the gravity-dominated regime increases with increasing width of the size frequency distribution and with increasing size of the pebbles[50,59]. Granular media formed by particle deposition (e.g., RLP) possess lower filling factors than media, which were additionally post-compacted by vibrational treatment[58]. Taking these constraints into account, the minimum volume filling factor should be[59] $\Phi_{\mathrm{cluster,min}} \approx 0.45$.

If we look at nucleus formation based on our model[45], the gravitational collapse of a pebble cloud caused by the streaming instability, the pebbles have to possess sizes in a narrow range around an optimal radius[60]. Added to this is the condition to grow to these sizes by collisional sticking[61] which narrows the size distribution even further. As a result, we expect the pebbles to be quasi-monidisperse. Without any post-formation compaction of the pebble accumulation, we assume in the main paper a volume filling factor of the pebble accumulation of[51] $\Phi_{\mathrm{cluster}} = \Phi_{RLP} \approx 0.55$ which also assumes that inter-pebble friction is strong[52]. As shown in the main paper, this volume filling factor and the assumption of a two-stage hierarchical arrangement of the nucleus lead to an overall porosity of the nucleus consistent with observations. However, as flagged in the text, it is noted that this does not exclude alternative setups of the nucleus.

Derivation of Φ_{Max} using Eq. 2 in Methods : Eq. 2 in Methods can be used to derive Φ_{Max}, when all other values are known. Supplementary Table 1 shows the parameter space feasible for the variables in Eq. 2 and the deviation of the resulting maximum compression Φ_{Max} from the RCP value. We can see that for cm- and mm-size pebbles, i.e. for $p_m \approx 10^{-2}$ Pa and for $p_m \approx 10^{-1}$ Pa, respectively, the maximum compression is always so close to the RCP case that we can argue $\Phi_{\mathrm{Max}} = \Phi_{\mathrm{RCP}}$, regardless of the exact choice of the parameters Φ_{Min}, Δ' and Φ_1. The choice of the parameters $\Delta' = 1.3 \pm 0.05$ and $\Phi_1 = 0 - 0.3$ is irrelevant for the output as formally is the initial volume filling factor $\Phi_{\mathrm{Min}} = 0.50 \pm 0.05$.

In the lower two lines of Supplementary Table 1, we show that for 100 µm-sized pebbles, i.e. for $p_m \approx$ 1 Pa, the maximum compression is $\Phi_{\mathrm{Max}} \approx 0.61 < \Phi_{\mathrm{RCP}}$ and that for even smaller pebbles, i.e. for $p_m \approx$ 3 Pa, the maximum compaction is so low that the volume scaling factor $\eta = \frac{\Phi_{\mathrm{RLP}}}{\delta\Phi} = 18$ gets unfeasibly high[48]. Thus, Eq. 2 delivers a meaningful solution only for macroscopic pebble sizes >~ 100 µm. This also excludes a non-hierarchical setup of the boulder consisting only of sub-µm-sized dust/ice particles without intermediate-

sized pebbles. Thus, Eq. 2 cannot be used to constrain the initial porosity of the boulder by measuring the energy loss (see Supplementary Table 1).

It should be emphasised that $\Phi_{Max} = \Phi_{RCP} = 0.64$ is only valid for quasi-monodisperse spherical pebbles for which $\Phi_{Min} = \Phi_{RLP} = 0.55$. Wider size frequency distributions of the pebbles and other pebbles sizes may change these values considerably. However, Yu and Zou[59] showed that the difference between the minimum and the maximum volume filling factor, $\Phi_{Max} - \Phi_{Min}$, is rather independent of Φ_{Min}. Thus, our estimate of the impact energy loss (Eq. 2 in the Main paper) can easily be adopted to all cases with different pebble properties.

p_m [Pa]	Φ_{Min}	Δ'	Φ_1	$\Phi_{RCP} - \Phi_{Max}$
10^{-2}	0.55	1.3	0.05	7.5E-7
10^{-2}	0.50	1.3	0.05	1.8E-7
10^{-2}	0.60	1.3	0.05	9.3E-6
10^{-2}	0.55	1.25	0.05	1.0E-7
10^{-2}	0.55	1.35	0.05	3.3E-6
10^{-2}	0.55	1.3	0	1.1E-6
10^{-2}	0.55	1.3	0.35	3.7E-8
10^{-1}	0.55	1.3	0.05	6.9E-4
1	0.55	1.3	0.05	0.032
3	0.55	1.3	0.05	0.060

Supplementary Table 1 : Parameter space and results of Eq. 2

F4. Our use of the word “Primitive” in the text

Weisman et al.[62] state the following in their paper on the Origin and evolution of cometary nuclei :

“ “Primitive” is a relative term and it is important to define what we mean by that. Precursor elements and molecules that were incorporated in comets were processed in the interstellar medium and before that in the cores of massive stars, possibly multiple times. Volatile ices are deposited onto interstellar grains where UV radiation and cosmic rays provide chemical evolution. Further processing occurs as the natal interstellar cloud collapses and material is brought together in denser and warmer environments. For the purposes of this paper we will define “primitive” as the chemical state of cometary materials as they began to agglomerate/accrete into macroscopic bodies. As the surfaces of these bodies are modified by the physical processes described below they lose their primitive nature, but the nucleus interior likely remains primitive. Given the earlier processes mentioned above, it would be wrong to ever refer to these bodies as “pristine” as some researchers mistakenly do.”

On the basis of the above, we have decided to refer to the ice initially exposed by Philae at touchdown to be Primitive in nature.

F5. References for the Supplementary Material

53. O'Rourke, L., et al., The search campaign to identify and image the Philae Lander on the surface of comet 67P/Churyumov-Gerasimenko, Acta Astronautica, 157, 199-214, 2019

54. Fornasier S., et al, The structure of the regolithn 67P/Churyumov-Gerasimenko from ROLIS descent imaging, Science, 349, 6247, 2015

55. Delsemme, A.H., and Miller, D.C., Physio-chemical phenomena in comets III, The continuum of comet Burnham, Planetary & Space Science, 19, 1229-1257, 1971

56. Heinisch, P., Analysis of the Magnetic Field Observations of the Comet Lander Philae, Cuvillier, in-print, ISBN 9783736960404, 2019

57. Arakawa, S., and Ohno, K., Thermal inertias of pebble-pile comet 67P/Churyumov-Gerasimenko, MNRAS, 497, 1166, 2020

58. Watson, P. K., Mizes, H., Castellanos, A., & Pérez, A., Powders & Grains 97, ed. R. Behringer & J. T. Jenkins (Rotterdam: A. A. Balkema), 109, 1997

59. Yu, A.B. and Zou, R.P., Prediction of the porosity of Particle Mixtures, Kona Powder and Particle Journal, 68-81, 1998

60. Yang C.-C., Johansen A., Carrera D., Concentrating small particles in protoplanetary disks through the streaming instability, A&A, 606, A80, 2017

61. Lorek, S., Lacerda, P., Blum, J., Local growth of dust- and ice-mixed aggregates as cometary building blocks in the solar nebula, A&A, 611, A18, 2018.

62. Weisman, P. et al, Origin and Evolution of Cometary Nuclei, Space Science Review, 216, 6, 2020

63. Mottola, S. et al, The structure of the regolith of 67P/Churyumov-Gerasimenko from ROLIS descent imaging, Science, 349, 6247, 2015

64. Capanna, C., Jorda, L., et al, Extreme 3D reconstruction of the final Rosetta/Philae Landing site, EGU General Assembly, Vol 18, EGU2016-4522, 2016

65. Vincent, J.B., shapeViewer, a Mapping Tool for the Morphological Analysis of Small Bodies and Mission Operations Planning, Lunar and Planetary Science Conference, No. 2083, id.1281, 2018

F6. Supplementary Figures

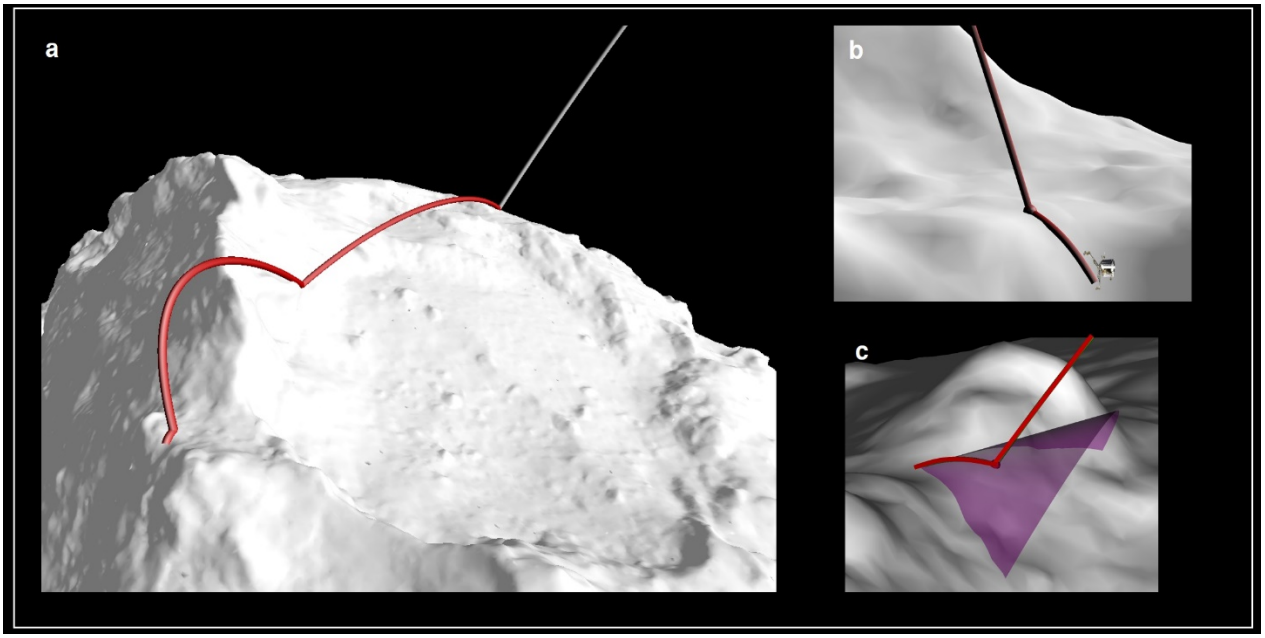

Supplementary Fig. 1: Trajectory overview. Image **a** shows the full trajectory from initial touchdown through to final touchdown. Image **b** is taken from the perspective of the final landing position of Philae looking back towards the TD2 position. Image **c** show the error cone.

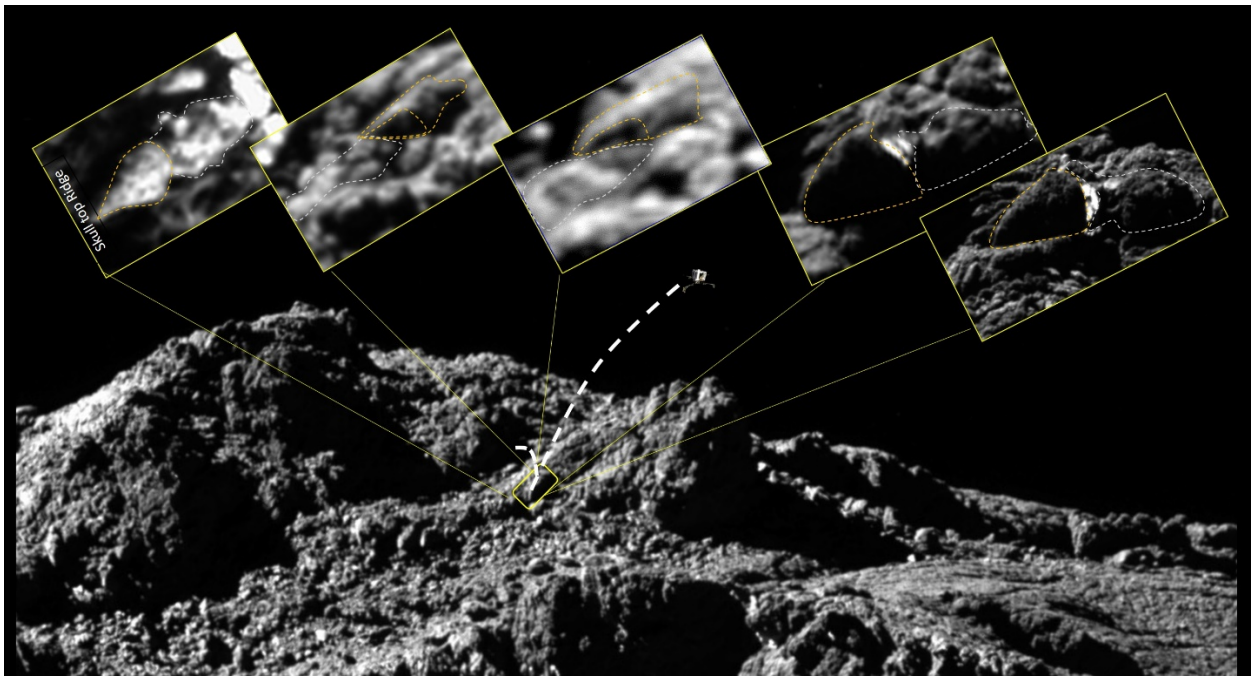

Supplementary Fig. 2 : Overlay of 5 different views of the Skull-top boulder region on top of a wide angle NAC image of the Abydos region. The connecting line meeting the central image represents the direction from where images were taken. Images displayed (L to R) 21st March 2016, 16th May 2016, 22nd October 2014 (Pre-landing), 6th August 2016 and 24th August 2016. Superimposed on the global image is the final Philae simulated trajectory including the last rebound to final landing location. The Skull-top hat boulder is in orange dash while the Skull face boulder is in light blue.

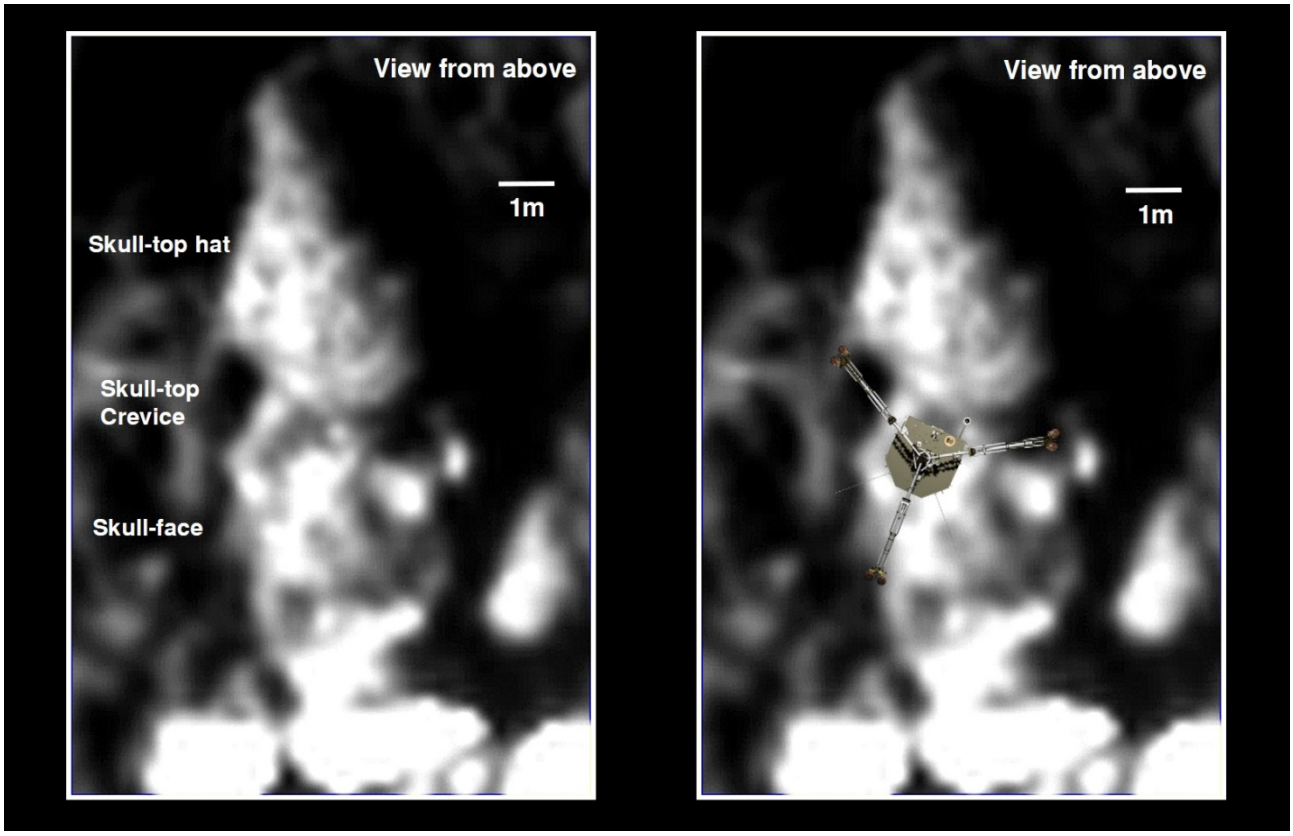

Supplementary Fig. 3: Skull-top boulders with Philae superimposed.

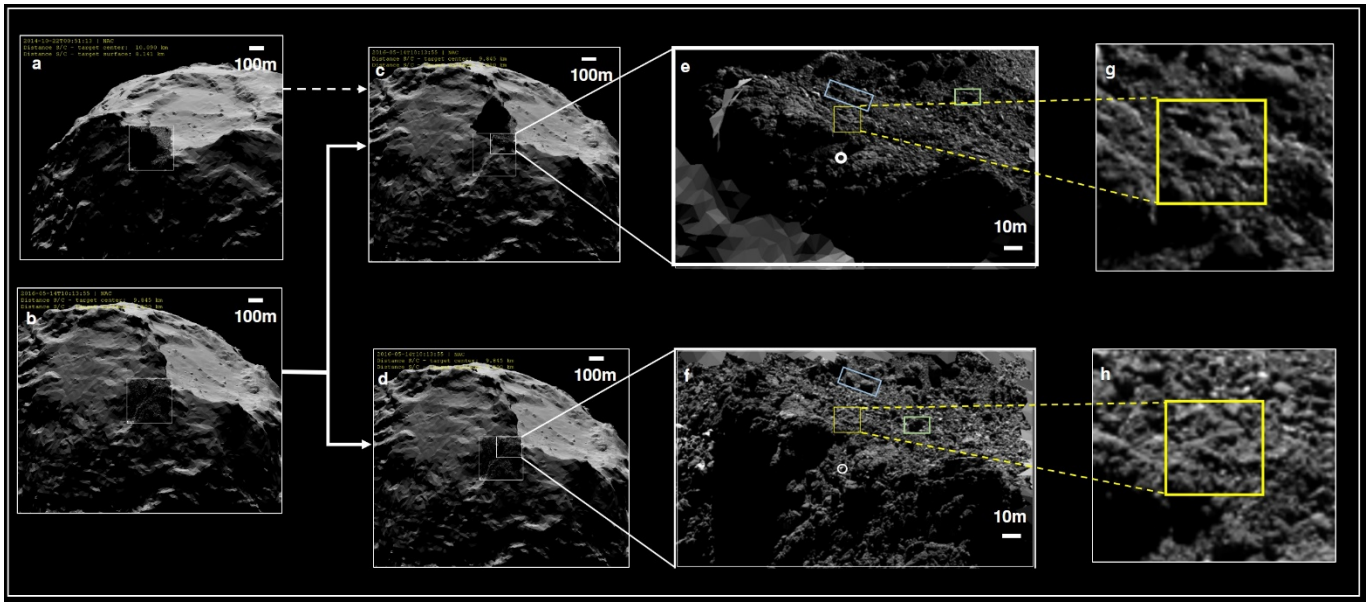

Supplementary Fig. 4: Pre & post-landing image comparison. **a** OSIRIS image of 22nd October 2014 (pre-landing) and **b+d** 14th May 2016 (post-landing) of Abydos region overlaid on 67P shape model. Image **c** 22nd October 2014 overlay viewed from the Rosetta geometry of 14th May 2016. Images **e** and **f** show zooms of Abydos with blue/green boxes highlighting boulder movement; white circle is Philae final location. Images **g and h** are zooms of skull-top ridge although image g is the shape model altered image of 22nd Oct 2014 to allow comparison with h. See Extended Data Fig. 1, Supplementary Fig.9 and Supplementary Video 1=.

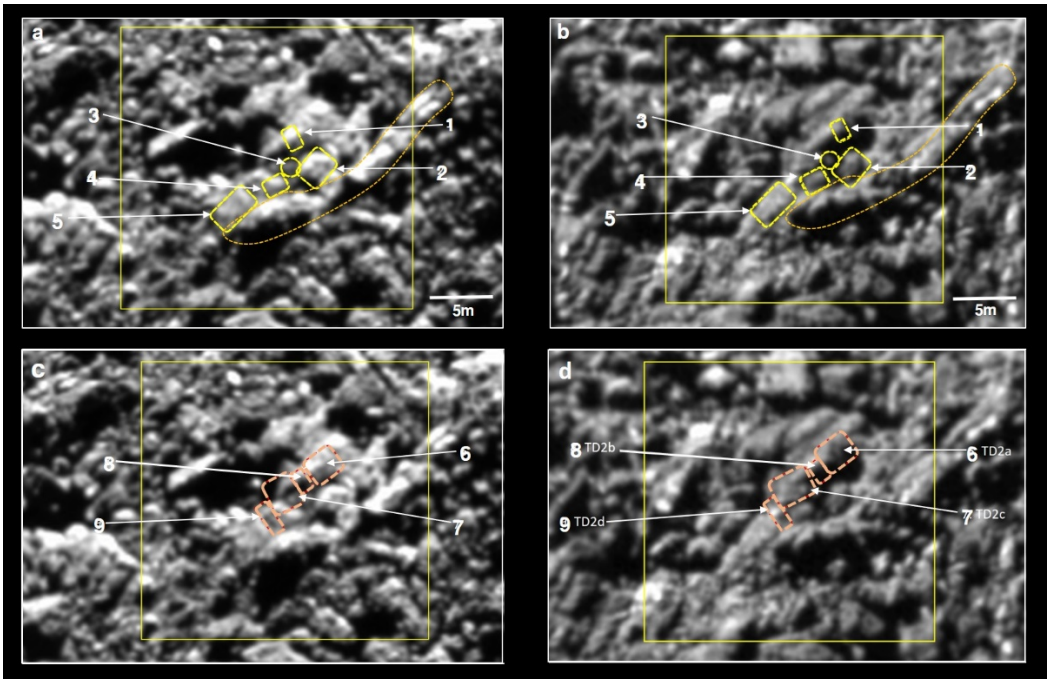

Supplementary Fig. 5: Analysis of pre & post-landing images. a & c : 22nd Oct 2014 **b & d** : 14th May 2016. Images **a** and **b** highlight five similarities (yellow dashes) between the images. Although viewing geometry & illumination differs, the same features are observed. Images **c** and **d** show differences (red dashes) between images. Points 6-9 in image **d** differ significantly with the same points in image **c** because they correspond to the 4 touchdown points (TD2a-2d). The boulders located above and to the left of the skull-top boulder region are located down in the Abydos valley. In image **a** and **c**, other skull-top ridge boulders are highlighted in dashed orange to further demonstrate consistency between the images.

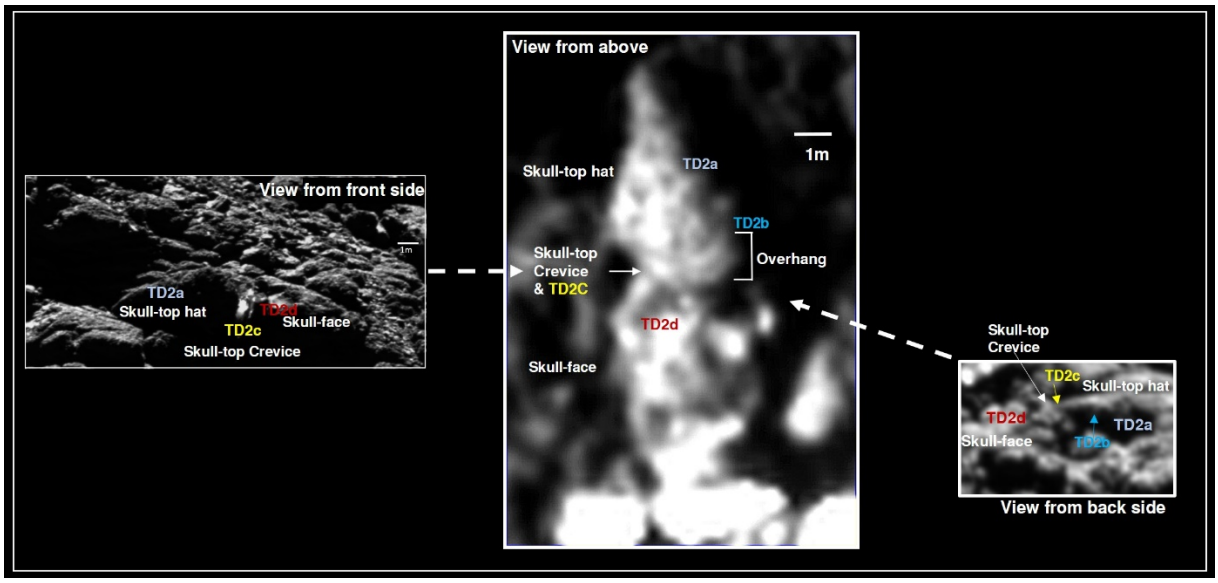

Supplementary Fig. 6: Skull-top boulders and the position of TD2a to TD2d Three different OSIRIS images (Left - 2nd September 2016, middle - 21st March 2016, right - 16th May 2016) provide views from the front side (left image), from above (middle image) and from the back side (right image) with touchdown points TDa to TD2d highlighted. Also the naming of the boulders are presented in each image. The dashed arrows show the viewing direction from which the left & right images were taken.

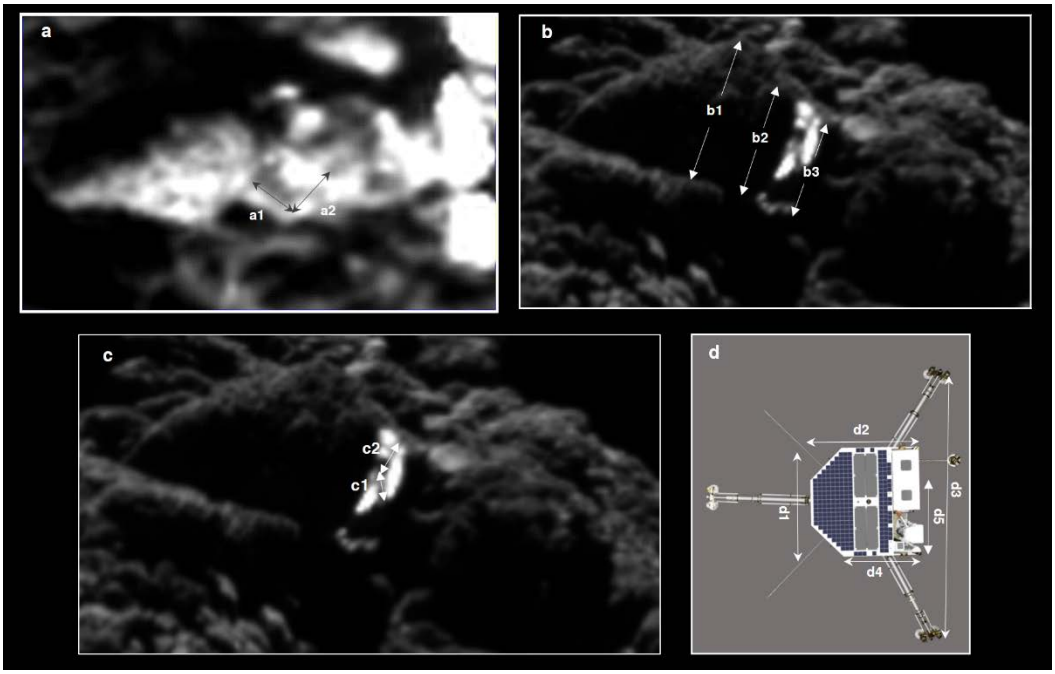

Supplementary Fig. 7: Comparison of cometary boulder measurements versus Philae dimensions in image d. a. OSIRIS image (21st March 2016 11:43 UT - resolution 0.195m/pixel). The edges of TD2d are measured by the dark arrows. Both a1 and a2 measure 0.915 ± 0.195m while the corresponding measurement in image d from Philae for each side is 0.85 m (d1 and d2). **b and c.** OSIRIS Image (24th August 2016 19:39 UT - resolution of 0.081m/pixel). The different heights are measured to be approximately, b1 = 3.80 ± 0.16m, b2 = 2.75 ± 0.16m and b3 = 2.07 ± 0.16m. For comparison in **d**. Philae has a distance between legs (d3) of 2.59m. Image **c** has length of the sides of the ice impression to be c1 = 0.60 ± 0.08m and c2 = 0.61 ± 0.08m approximately comparing c1 and c2 with Philae d4 & d5 equivalent side measurements = 0.60m.

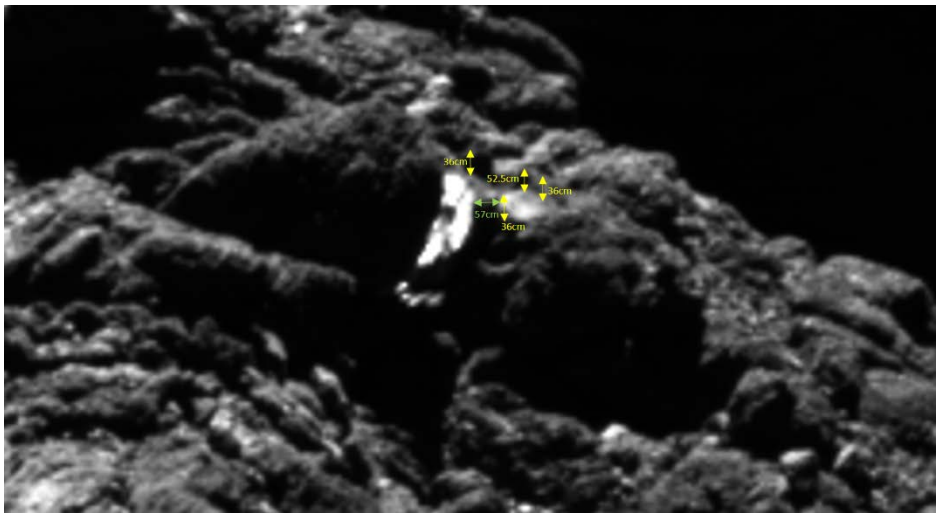

Supplementary Fig. 8: Sample of the dust heights around TD2d Dust heights as provided for the TD2d location with values varying from 0.36 to 0.53m (+/- 0.04m).